UNIVERSITÀ DEGLI STUDI DI MILANO

DEPARTMENT OF PHYSICS

PHD SCHOOL IN

PHYSICS, ASTROPHYSICS AND APPLIED PHYSICS

CYCLE XXXIII

CHARACTERIZATION OF NANOSTRUCTURED FILMS WITH NON-LINEAR ELECTRICAL PROPERTIES FOR THE FABRICATION OF NEUROMORPHIC DEVICES AND UNCONVENTIONAL DATA PROCESSING

Disciplinary Scientific Sector FIS/03

PhD Thesis of:

Matteo Mirigliano

Director of the School: Prof. Matteo Paris

Supervisor of the Thesis: Prof. Paolo Milani

A.Y. 2020-2021

Contents

1. Introduction

The continuously increasing demand for ubiquitous distributed complex computational performances can be hardly sustained by using digital computing hardware based on von Neumann architecture [1–3]. An approach aiming at the reproduction of the human brain architectural and dynamical properties has been proposed: the study of the mechanisms underlying data processing in the brain are source of inspiration to find novel hardware and software solutions to overcome the intrinsic limitation of the digital computer paradigm [4–8].

The expression "neuromorphic computing" is used to identify the search of data processing hardware and software schemes emulating those implemented by mammalian brains [5,9,10], with the ambitious objective to transfer biological neural information processing to artificial computing systems. To date, this approach is based on the use of artificial neural networks that reproduce the non-linear behaviour of brain neurons using hardware architecture developed for digital computer working as Turing machines. This is a contradiction since the human brain is not working as a Turing machine [4,11,12].

Very recently attention has been focused on the so-called unconventional computing approaches broadly consisting in the exploitation of the physical properties of matter to perform computation [4,5,13–16].

One of the possible architectures for non-conventional computing is based on assemblies of interconnected nanoscale electrical switching elements that exhibit synapse-like behaviour [11,17–19]. The elemental building blocks of these kinds of networks are nanoparticles showing non-linear electrical properties upon the application of a voltage. Before discussing unconventional computing based on nanostructured systems, I will briefly present the main features of digital computing and artificial intelligence.

1.1. Digital Computing

1.1.1. The Turing Machine

The most successful and versatile computing machine developed in the history of the humankind is the electronic digital computer [1,4,20]. The formalization of the theoretical foundations of the architecture of a digital computer started with Aristotle and received its final frame with the works of A. Turing and A. Church [20]. They proposed a theoretical model of computation based on an ideal machine, known as the **Turing Machine** (TM), that manipulates strings of characters, given a set of rules [20].

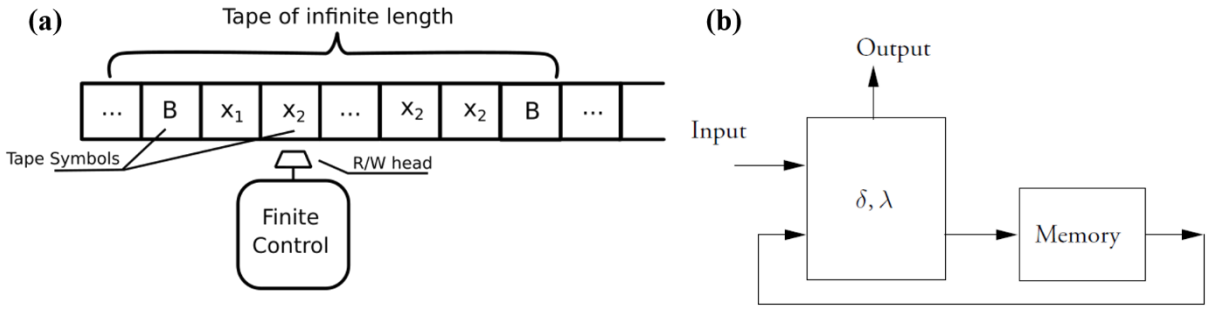

Figure 1-1 (a) Scheme of a Turing Machine. Symbols are stored on a tape with infinite length. The head (or control unit) writes and reads the symbols on the tape moving left and right. The process is handled by a precise set of instructions, that respond to the symbols on the tape. (b) Structure of a FSM composed by a logic unit and an external memory. FSM executes a series of steps taking its current state from a set Q and current external input from a set Σ of input letters and combines them in a logic circuit L. The logic unit produces a successor state in Q and an output letter. It can be viewed as having two parts, the next state function δ and the output function λ. δ computes the state of the machine at each processing step and stores it in memory. λ computes the output depending by the actual state and the input. The output is released to the external world. From [20].

A TM (Figure 1-1 (a)) consists of a tape with infinite length, divided in several unit cells and a head (or control unit) that can read or write symbols on each cell. At each implementation of an operation, the head receives an input from the tape and writes output on it. Each operation is implemented following the instructions corresponding to the symbols written on the tape. The tape and the head are modelled like Finite State Machines (FSMs). A FSM has a logic unit and an external memory (Figure 1-1 (b)): the memory unit stores the actual state of each component, and the input-output architecture exchange information among them to implement the writing/reading operations of the head on the tape.

The following set of rules formally defines a TM [20]:

1. a set of states
2. an alphabet of symbols
3. a blank symbol
4. input symbols
5. an initial state
6. a final state
7. a transition function

These rules define the modern concept of program that implement operations to perform a task. Starting from an input configuration $C(0)$ built from the alphabet, the transition function is repeatedly applied to obtain e sequence of configurations $C(1), \dots, C(n)$, until a halting criterion is reached. The alphabet in modern digital calculators is constituted by the binary digits $\{0,1\}$. Through two digits it

is possible to represent a general set of symbols, so a general working frame can be achieved. For each digit employed to represent a symbol, a bit of memory is occupied [20].

A TM can manipulate and transform sequences of character from the alphabet. The tape and the head have a memory unit to store the manipulated symbols. The apparatus of ordering and the rules that regulate the use of the alphabet to implement operations define a language [20]. A TM accepts only recursive languages, those for which a halting criterion exists for each input taken from the language; in this way TM performs transformations on a series of characters and implements symbolic computation [4]. Each task is serially executed: read/store on memory, set on a particular state, implement the read/write operation depending on the assumed state [1,20].

J. Von Neumann codified the architecture on which the modern digital computers are based (Figure 1-2) [1]: the central processing unit consists of a control unit that contains registers and counters, to drive the program execution, and an arithmetic unit that implements fundamental operations. An external memory stores data and instructions to be exchanged with the central processing unit. The input/output mechanisms enable the communication with external world.

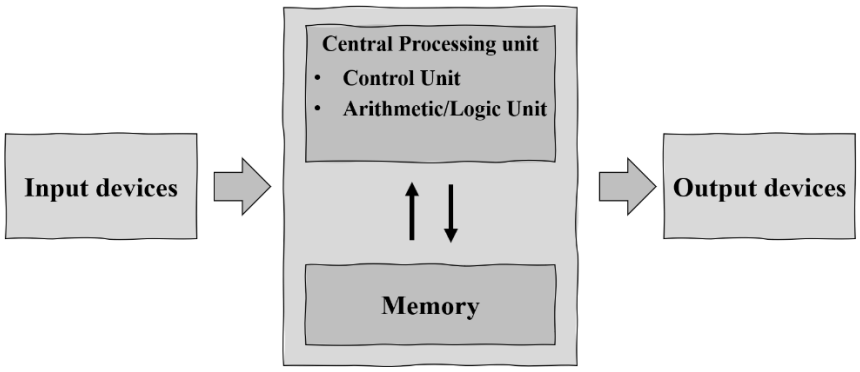

Figure 1-2 Scheme of the Von Neuman architecture. The Central Processing Unit contains the arithmetic one, that implements logic operations on bit data, and a Control Unit, a fast memory register that handle the arithmetic unit. The Memory is the unit where data are saved and exchanged with the Central processor. The input/output data stream is controlled though device that insert and extract data from the memory.

This kind of machine can solve all the tasks of a TM and can be reprogrammed to execute different programs. The hardware of digital computers is based on transistors.

1.1.2. The hardware

The hardware of a digital computer is based on logic circuits executing Boolean operations [21]. The inputs and the outputs of the circuits are 0 and 1 values usually associated to two well distinct voltage outputs. These signals are elaborated to map a set of inputs to a set of outputs. There

are various types of logic gates implementing different Boolean functions (AND, OR, NOT, etc.) [22]: Figure 1-3 shows an example of an AND and an OR gate obtained through two switches.

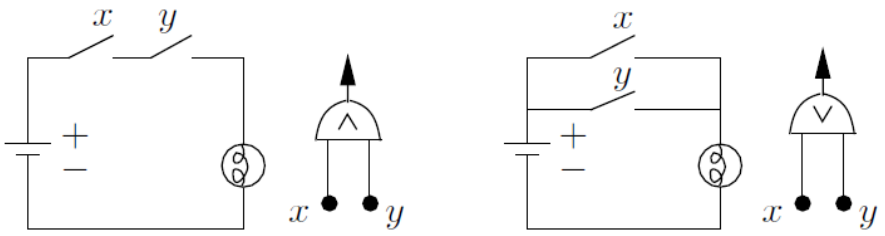

Figure 1-3 Implementation of logic gates through switches. The input logic values correspond to the switch state: 0 for open switch, 1 for closed switch. The output values correspond to the voltage output: high voltage for logic 1, low voltage (ground signal) for logic 0. Left: the AND gate implementation through two switches, with the related symbols. To implement the AND operation, logic output is 1 only when both inputs are 1, two series switches can be used. Right: the OR gate implementation through two switches. To implement the OR operation, logic value is 0 only when both inputs are 0, two switches in parallel configuration can be used. From [20]**.**

The building block of modern digital computers is the Field Effect Transistor (FET) acting as a switch with two conducting and non-conducting states. The Metal Oxide Semiconductor (MOS) is the most widespread technology employed to fabricate the FET [22]; the MOS structure consists of a thin silicon oxide layer grown on doped silicon substrate. Two electrodes, the drain and the source, are connected to two highly doped regions, between the source and the drain a channel, the depletion region, is placed.

The fabrication and integration of MOS-FETs is based on the Complementary MOS (C-MOS) technology [22,23]. This consists in the use of a symmetric pairs of p-type and n-type MOS-FET for the implementation of logic gates and digital circuits. The fabrication process is based on the masking of the silicon substrate and the doping process in sequential steps to obtain the desired configuration of MOS transistors on the same substrate. C-MOS technology boosted the integration capability of logic circuits, improved the speed and the computation power of digital computers [23]. In Figure 1-4 the trend for the last decades of the device dimensions and number of transistors per chip are shown.

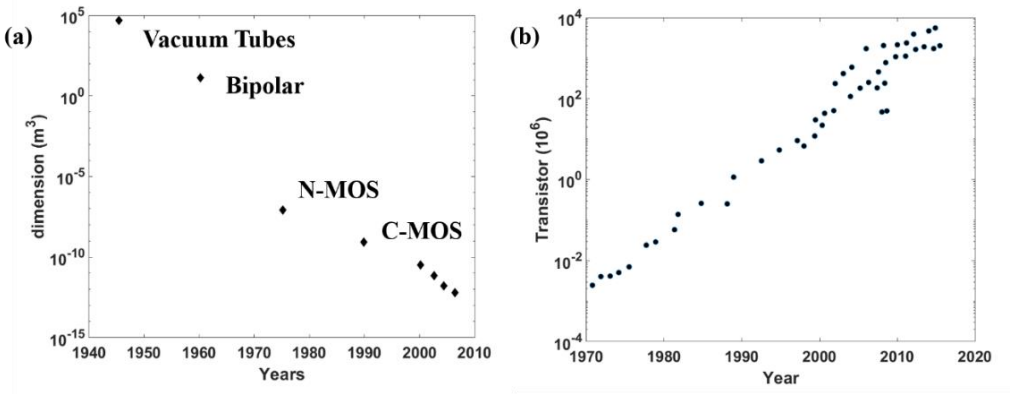

Figure 1-4 (a) Scaling of size over the years for the transistor; y-axis in logarithmic scale. Figure adapted from [23] **(b) Number of transistors for the Intel processor over the year; y-axis in logarithmic scale. Adapted from** [24]**.**

Although the miniaturization of MOS directly scaled up the performances of digital computers, some limitations are intrinsic to this technology. On one hand, the miniaturization process is limited by the appearance of quantum effects that prevent the correct device operations [25]; on the other hand, the high surface density of transistors per unit surface area rises the problem of energy dissipation [9]. In addition, the Von-Neumann architecture has an intrinsic limit due to the physical separation of the memory and computation units [1,11,16,26].

The advent of the internet of things and of autonomous driving demands for continuously increasing computational performances, whereas the performances of digital computers have reached a limit imposed by the dimension of the hardware [9,27–30]. Significant performance improvements of computational systems based on von Neumann architecture, in terms of data handling and processing, are hardly sustainable at extreme miniaturization due to the required energy dissipation capabilities [9,16,28,30].

An approach aiming at the reproduction of the human brain architectural and dynamical properties has been proposed to overcome these limitations [2,5,27,28,31–33]. The study of the mechanisms underlying data processing in the brain are a source of inspiration to find novel hardware and software solutions to overcome the intrinsic limitation of the digital computer paradigm [7,8,11]. The development and widespread exploitation of a “neuromorphic technology” is the very ambitious target [4,5,7,8,30,34,35].

1.2. Artificial Intelligence

1.2.1. Biological neural network

The neuron is the fundamental building block of the nervous system [36]: it consists of a lipidic central body (the soma) with a high number of dendritic terminations, the synapses, and the axon, an extension of the soma that extend for several time its diameter (Figure 1-5).

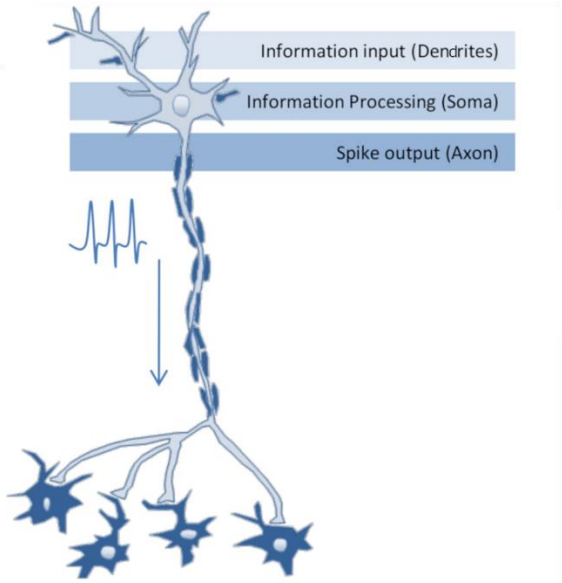

Figure 1-5 The structure of a neuron. The soma is the cell body, where action potentials are integrated over time and can be generated. The body is ramified into the dendrites, the terminations that drive the arriving signals to the body. The axon is the transmitting part: the generated potential travels along it to reach other cells. Adapted from [33]**.**

The axon also terminates in dendritic synapses; one neuron can be connected to 10^4 other ones through the synaptic dendrites [32,36]. In the extracellular media outside the soma there is a distribution of positive charge excess, while in the inner an excess of negative charges; the lipid membrane of the soma acts like a barrier for the diffusion of the charges. The voltage difference across the membrane caused by the excess of charges is defined as the membrane potential [36,37]: when the charge balance of the neuron at rest is perturbed, it emits an electrical signal called action potential [36]. The typical amplitude of the signal is about 100 mV and the temporal width 0.1-1 ms, the action potential is emitted when the membrane potential reaches a certain threshold. The neuron firing is followed by a refractory period, after the action potential is emitted, the neuron ability to generate a second action potential is suppressed.

The emitted signals travel along the axon and can be transmitted to other neurons through the synapses [7,32,36]. Considering a couple of neurons, the pre- and post-synaptic one, the incoming

signal can trigger the emission of other action potentials on the post-synaptic neuron. The transmission is regulated by the strength of the synaptic links among different neurons. Synaptic plasticity is the mechanism considered to underlie the learning and memory functions of the brain [36].

The concept of synaptic plasticity has been heavily influenced by the Hebb's postulate [38] stating that the connection strength between neurons is modified based on neural activities in pre-synaptic and post-synaptic cells. The mechanism that control the potentiation (increasing of synaptic conductance) and depotentiation (decreasing of synaptic conductance) is called Spiking Time Dependent Plasticity [36,39]. The potentiation occurs if the pre-synaptic neuron repeatedly fires preceding the post-synaptic neuron. Vice-versa, when the post-synaptic neuron precedes the pre-synaptic one in the action potential emission, depotentiation occur. A smaller time window among pre and post synaptic spikes translates in a stronger potentiation/depotentiation. These processes are at the base of learning behaviour and associative memory [36].

To further understand how the brain processes information, the activity of several connected neurons should be considered. A single neuron has not a high computation capability: when several neurons are connected, perception and learning naturally emerge [36,40]. The mammalian brain is characterized by a high number of neurons, about 10^{11}, and an extremely high number of synapses, about 10^{15}. The synaptic plasticity of connected neuron regulates the overall activity of the network [36].

Neuron networks produce bursts of spikes separated by period of reduced activity [37,40,41]; the individual neuron integrates the signals arriving form the other ones and redistributes electrical stimuli to the network. Spatial and temporal distributions of spikes described by power laws has been observed in the measured activity of neuronal culture [42] independent from the temporal scale of the observations [42,43]. This kind of activity is observed in extremely different complex physical systems: nuclear reactions [44], granular media [45], earthquakes [46], and it is typical of systems composed by a huge number of units that can integrate and redistribute back the energy to the system itself [47,48]. The scale invariance and the power law description of the measured observables are typical of dynamical systems organized into a critical state (Self-Organized Criticality, SOC). Another hint of SOC in dynamical media is the 1/f noise observed in measured electrical signal of neuronal network [42,49], also if the relation with correlated behaviour is still debated [49]. Hypothesis related to the organization into a SOC state for neuronal network, were considered to explain complex information transmission, stable network activity, optimization and training processes [42,43,50].

The brain capacity of integrating information derives from the cooperation of different areas of cortical neuronal networks [51,52]. Many theories of whole-brain function rely on the fact that cooperation and effective communication between spatially separate neural regions is crucial for the execution of effective behaviour [53]. This is at the base of the appearance of complex behaviour, like languages and coordination [36,52].

1.2.2. Is the Turing Machine Neuromorphic?

The theoretical solidity of the Turing Machine paradigm and its success in providing the basis of an unprecedented technological and anthropological revolution that the humankind is facing from the last fifty years, somehow distracted from a careful consideration of the similitudes and differences between the TM and the mammalian brain modus operandi and cogitandi [1,4,12,54]. Actually the question about the capability of "thinking" of a machine was raised in 1950 by A. Turing [12,55]. He highlighted some differences among a computing machine and the human faculties: 1) human brain can make "mistakes", while a machine gives always the "correct" answer if correctly programmed; 2) it is difficult to forecast the human behavior, while machines are essentially predictable. Although Turing avoided to define the term 'thinking', his paper shaded a new light on his computation model showing that some elements necessary to simulate the human behaviour were missing. Turing proposed the introduction of a random element in a machine to better simulate the human behaviour [12,54].

The role of randomness in the complex functioning of human brain has been somehow overshadowed in the development of "neuromorphic" computing: attention has been mainly concentrated on the serial/parallel character and on different architectures that implement memory and computation ability for digital computers and neural systems [4].

A further very important aspect is that a TM can only implement tasks for which an algorithm with a halting condition and no state of indecision exists [4,20]. The task for which these conditions are not respected is the classification one. Categorizing require abstract abilities and autonomous decision [56]. The limitations of the TM approach appear when this class of machines is programmed to implement operations like pattern recognition, data mining [9] and applications requiring autonomous decisions [56]. The question about the ability of "taking decisions" in programmed machines requires new solutions about the design of hardware and software of an artificial intelligence [5,57,58].

1.2.3. Hardware for artificial intelligence

Artificial neural networks (ANNs) have been proposed and developed to perform tasks such as pattern recognition with high efficiency in terms of performances at a low energetic cost through the mimicking of brain general features [59]. ANNs make it possible to automate tasks that are complex to be programmed with digital computers and represent a useful engineering tool for a variety of technical applications, such as pattern recognition and function approximation.

The simplest artificial neural network is the perceptron [60]: a single node designed specifically to implement a logic operation [61], it is based on the McCulloch-Pitts non-linear neuron model [62] and it is the simplest device that can be used for classification of patterns [63]. It basically consists of a single neuron with adjustable synaptic weights and bias and it can classify linearly separable functions, as shown in Figure 1-6 [61].

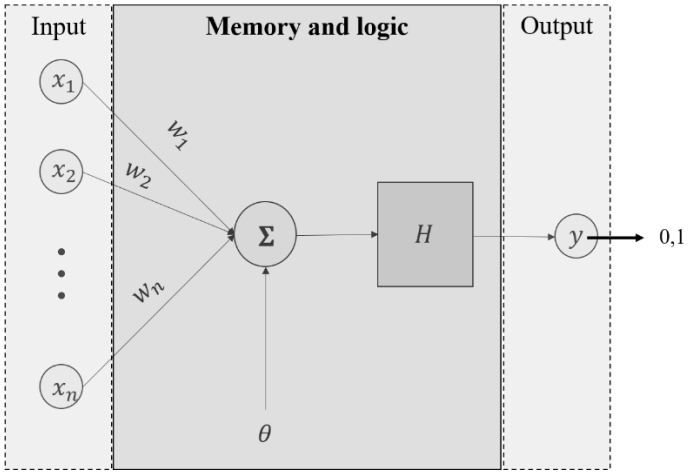

Figure 1-6 The receptron architecture. The inputs $x_1, \dots, x_n$ are connected to the central unit through weighted links. The central unit performs the weighted sum of the inputs and adds a constant bias θ. The result undergoes a thresholding process to obtain 0 or 1 as output. The weights and the summing unit represent both memory and logic operation.

Formally, the output *y* of the perceptron is given by:

$$y = H(\sum_i w_i x_i + \theta)$$

where H is the activation function [59], that gives as result 1 if the argument is higher than a certain threshold, 0 otherwise and θ an external constant bias [59]; the perceptron output can be either '0' or '1'. This allows to implement a function that associates the input to one output: the weighted sum of the inputs is computed, and the two output values are discriminated through a thresholding process. The network can be trained, adjusting the weights to match the correct input-output combination.

The perceptron is a linear classifier [61,64]: a set of inputs are linearly combined and classified into two classes, 0 and 1. However, compared with a Turing Machine, it has a lower computational power since it can compute only linearly separable function [61].

Several perceptrons can be connected to obtain an artificial neural network (ANN) [59]. There are two fundamental class of neural networks: feedforward, where the connections between the neurons do not form a cycle [59], and recurrent neural network, where the connections can present feedbacks [65,66]. The first class is most widely used to implement classification [67], autonomous learning [68] and predictive data analysis [69]. The architecture of a feedforward network (Figure 1-7) consists of multi perceptron layers, where the first unit layer is directly connected to inputs and some intermediate layers (hidden units) are connected in series [68].

One or more units in the last layer play the role of network outputs [68]. The multiple layer structure allow to reach a high level of abstraction, transforming the output of one layer into a higher abstract representation for the next one [67,68]. This method is known as deep learning [68]: as it results, complex function can be learned by the multi-layer network, as demonstrated for a general feedforward structure [70,71].

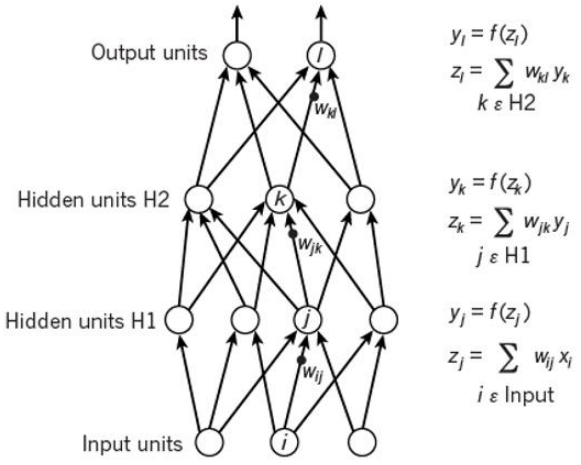

Figure 1-7 Feedforward multilayer neural network, the first layer directly connected to the inputs units, two hidden layers, H1 and H2, and one output layer with two units. On the left, the equation used to compute the forward output in the network with two hidden layers. At each layer, the total input z to each unit is computed as the weighted sum of the outputs of the units in the layer below. The non-linear function *f(.)* is than applied to compute the output of the unit. The operation is repeated for each unit at each layer, until the output unit layer are computed. Adapted from [].

In ANN, learning consists in adjusting the unit weights to approximate the inputs with the desired output [59]. The process can be carried out in the supervised or unsupervised manner [59]: in the first case, some teaching data, the batch sample, are given to the network in form of input-target

couples, the target being the desired output response that should be given when the associated inputs is matched [59]. The second one, consists in memorizing only one set of data, that will be recalled in future, when similar featured inputs are given to the network [59].

The most common machine learning method is the supervised one [68]. During the training, an input in form of a bit array, for example the pixel values of an image, are given and the network produces an output as a form of vector score, one for each input. The aim is to assign the highest score to the inputs that matches some category. The difference between the target and the output is computed, and each weight of the machine is changed to minimize the error [59,68,72]. A widely used approach is the gradient descent [72], consisting in computing the outputs and the errors for a batch of examples, the average gradient of the output evaluating for each units in the networks by what amount the error would increase or decrease if the weight were increased by a tiny amount [72]. The weights are then adjusted in the opposite direction of the gradient. The gradient for each weight variation is computed following the backpropagation procedure [72]; the computation is carried out for each layer by working backwards from the gradient with respect to the output of that layer.

In order to achieve a high abstraction ability and to approximate well a high number of functions, the ANN must have a high number of units and layers. This directly affect the learning process since the adjusting weights for each input is time consuming. In addition, the perceptron networks are implemented on digital computers where the von Neumann bottleneck limits the attainable performances. The technological goal is thus the fabrication of an hardware coherent with the neural networks architecture.

1.2.4. Hardware implementation of artificial neural network

Since the appearance of the first artificial neural networks hardware, the availability of a component with a nonlinear behaviour mimicking that of the synapse was a major technological issue. In neuromorphic applications, the signal must be elaborated in real time as well as the output [6,30].

The strategy to build CMOS-based neuromorphic device consists in designing circuits that simulate the behaviour of the basic biological counterparts, synapses and neurons, and then integrating them into more complex devices [30]. This is possible thanks to the Very Large-Scale Integration reached by the CMOS technology. This is achieved through very expensive solutions or imposing the operation of the MOS transistor in the sub-threshold regime [30]. In the last case, the main conduction mechanism is diffusion, similar to that of neurons allowing to reproduce a dynamic behaviour similar to the neuronal spiking activity, however in this regime noise can strongly influence the performances [30].

An interesting alternative to the CMOS is represented by the memristor [73–75]. The memristor is the fourth fundamental electronic component together with resistor, inductor and capacitor. It was theoretically predicted by L. Chua [73] in 1971 and experimentally demonstrated in 2008 [76]. It can be employed to implement a reversible switching between two resistive states, with no need of voltage or current control, nor of an external power supply. Thanks to this feature it is considered an efficient element to implement the synaptic conductance changes [33,77].

The usual scheme of a memristor is a thin insulator or semiconductor film between two metallic electrodes: the application of an external electric field causes the migration of some charge carriers, like ions, into the thin film, building bridges between the electrodes. The formation of the conductive paths, as shown in Figure 1-8, known as *electroforming step* [77], results in the switching to a different resistance level.

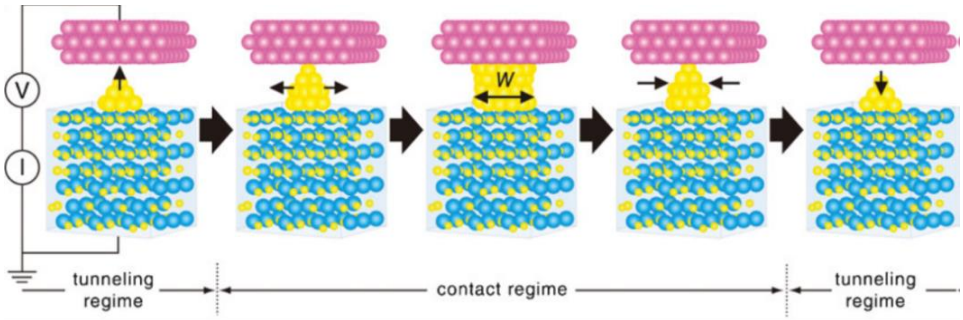

Figure 1-8 Operating model for the metal bridge formation in Ag_2S atomic switch. The top layer represents Pt electrode, the voltage signal is applied between the electrode and the Ag_2S switch. The bridge is formed under negative bias and destructed under a positive bias, through the migration of Ag atoms after a redox process. In the first step, the metal protrusion is still partial, and the system is in high resistance state. Under the application of the negative voltage, the metallic bridge is formed, and the cross-section increases the are with the conductivity. When the bridge reaches a cross-section diameter W, the system is in the low resistance state. The bridge can be destructed inverting the polarity of the applied voltage. From [78].

The reached state is maintained until a voltage or a current higher than a certain threshold is applied to destroy the conductive bridges. Analogue systems are percolating films of metallic nanoparticles embedded in a dielectric matrix [19,79], and free filament memristive crossbar arrays [80].

Memristors are employed to fabricate artificial neural network based on the perceptron model [63] and Hebbian learning systems [81]. A good scalability and integration with standard electronic systems is achieved. However, the scheme is relied on a learning procedure, related to a weighting process, that is energetically onerous and computationally rigid [2]. This is at the origin of some drawbacks: performances are sensitive to device imperfections arising in the fabrication process and due to the extreme reached integration [2,82]. To overcome these difficulties solutions were proposed [2,82], like the use of an external software to monitor the device performances during the learning

phase. This scheme is one of the main issues of the artificial neural networks and more generally of neuromorphic devices based on supervised learning.

1.3. Beyond Artificial Intelligence: Unconventional Computing Models

1.3.1. Background

Recently a new class of data processing systems based on the exploitation of the physical properties of a material to perform calculations has been proposed [5,13,16,83,84]. This approach has been placed under the umbrella of a wide variety of models called unconventional computing [5].

Conventional computing is not always the most efficient way to process information [4,13,16]: devices that respond to rigid instruction requisites for programming systems, are intrinsically physically inefficient since they are designed to be forced into high potential barrier to follow precisely prescribed computing processes [13]. Freeing the computing architecture from abstract predictable models opens the research to a wide range of material that can be utilized as computational substrates [4,13]. On one hand, this allows to exploit the physics of the materials that naturally lead to an efficient process that minimize the free energy of the system [83]. On the other hand, the fine control of the material structure is not necessary, avoiding high-cost fabrication methods and difficult integration processes.

One concept that well captures the advantages of this approach, is the in-memory computing [16,28,85]. It refers to the ability of perform computation and store data in the same physical unit [28]. This presents the clear advantage to remove the latency and the energy burdens caused by the information exchange between separated memory and logic units. The physical processes linked to the evolution of some physical parameter, like current in electrical circuit, or conductance in conductive materials, allows to implement the elaboration of data inputs in the same place where this is stored.

The key concepts that should lead to the development of computing materials are the self-assembly and self-organization of elemental interacting components [4,13,83]. The material should spontaneously show the organization into the desired architecture and emerging physical properties that show dynamical evolution into critical states [16,43,83]. The concept of critical state consists in high sensitivity to small external perturbations that generate avalanches of events in some physical observable of the system [47]. The main features of this class of systems, that are related to the concept of Self-Organized-Criticality (SOC), are scale-free phenomena and long-range spatial correlation [47].

Similar scale-free properties appear in percolating systems [86]. Percolation is the phenomenon related to appearing of at least one fully connected path in a complex network of linked units, at a critical fraction of the number of units themselves [86]. Percolation theory gives powerful instrument to study and control the growth of systems composed by a high number of components with a complex organization [86,87].

Several models were proposed in the past to avoid the problems related to a rigid and inefficient request of high predictability [88–91]. For the sake of comparison, some theoretical model related to the field of artificial neural network are briefly reported below.

Boltzmann machines consist of a neural network where the output of each neuron is stochastically activated with a certain probability [92]. The model was studied to evaluate how noise, that is a natural source of stochasticity, can be exploited as a resource in the computation process [89]. It was experimental tested that the appearance of random transition in memristive element can empower the learning ability of a spiking neural network [93], however, this approach suffers from an onerous learning process [59,82].

Reservoir Computing (RC) is a computational framework to elaborate time varying input signals [65,94,95]. It encompasses several machines, like the echo state network [65] and the liquid machine [94]. RC exploits the non-linearities and high output variability of a recurrent neural network (the reservoir) to map an input into a readout layer [65,95]. The reservoir maps the input in high dimensional space, so that the readout can work on a signal with a higher number of parameters with the original one, increasing the computational power, the readout being a feedforward neural network [65,95]. RC gained much attention in the last years and was applied in different fields like robot control and speech recognition [5]. Several systems were implemented exploiting non-linear optical systems [96], FPGA [97] and memristors [98].

The main drawbacks are related to the development of a reservoir system that satisfy all the theoretical constraints (separation property, independence by the input story, non-linearity [65,88,95]) these features are hard to be implemented on the same physical substrate. In addition, the pre-processing data to fit the reservoir interface mode often adds a constraint to the computation process [98].

1.3.2. Nanomaterials and their emergent physical properties

The design of devices for nonconventional computation may demand the development of materials with physical properties that hardly fit the requirements of miniaturization, integration, scalability typical of the microelectronic industry on which digital computers are based [23,57].

Systems based on the autonomous evolution of some parameters linked to a physical substrate, such as carbon nanotube/polymer mixture [99] or FPGA systems [100], to perform computational tasks is the 'evolution-in-materio' [15,99]. A genetic algorithm is developed and software-implemented to evaluate the evolution of the physical substrate under the application of external stimuli. The computer based evolutionary algorithm is used to optimise and autonomously adjust the electrical control signal configurations to induce the desired properties to the physical substrate [15,100]. The response of the material to the external inputs can be employed to fulfil computational tasks [99].

Although this approach can achieve some reliable results for programmable hardware [15,100], forcing the physical substrate to follow a precise evolution results in processes with very low efficiency, or even some limitations of the substrate can emerge [84]. The principle underlying the training process is not different form the usual approach employed for classical computing systems, the complexity of the process is assigned to an external software [15,84,101].

A new approach in developing systems that show high amount of information process capability, scalability and efficiency, consists in the use of hardware obtained by the assembling on nano-objects [17,34,102–105]. The term nano-objects refers to artificially synthetized structures with different chemical composition and geometrical configurations, that are confined to the nanoscale at least in one dimension. A material fabricated assembling building blocks of nanometric dimension have different physical properties with respect the bulk counterpart [106–110]. The main advantage of this approach is represented by the self-assembling process of the constituents and by the exploitation of emergent behaviour in response to external inputs [11,18,111]. This is made possible by the complex physical interactions among the elemental building block and their collective response when a physical perturbation is applied to the system.

The physical properties of this class of systems appear from the confinement of the materials and their constituents at the nanoscale [112,113]. Nanoparticles, structures formed by few atoms, from molecules to clusters [112], have properties intrinsically different both from the atom and the bulk like materials [112,113]. Their physical properties arise from size and quantum effects [113]. Due to the presence of a high number of surface atoms, with a fewer number of neighbours with respect to the bulk one, makes the thermodynamic limit no longer valid for particle of nanometric sizes [113]. Hence, assembling a high number of nanoparticles, the organization into a critical state is the natural route followed by the system [18,114].

In the last years, systems obtained by the assembling of structure confined at the nanoscale at least in one dimension, like nanowire networks [34,104,115], atomic-switch networks [19,78,102,111] and cluster-assembled materials [103,109,110,116], gained a high interest from the

researcher community in the neuromorphic applications. These systems show stable activity in response to a wide range of input currents, and high resilience to high dissipated power [103,104,109,111]. They usually show dynamical evolution as response to external inputs electrical signals, measured by the resistance change over time, organizing the interaction among the constituents to dissipate a low amount of power [8,104,109]. Voltage dependent switching dynamics share similar features with the synaptic processes and temporal correlations suggested a Self-Organized-Criticality behaviour [18,114].

Material	**Single component**	**Switching mechanism**	**Emerging properties**	**Literature**
Atomic-switch network/ Nanowire network	coated silver nanowire	diffusion of metal cations and reduction/oxidation processes	Spatially distributed memory and recurrent dynamics, Winner-Takes-All	[17,18,78,102]
Cluster-assembled films (percolation threshold)	Sn nanoparticle	Electromigration	Self-Organized-Criticality, synaptic like resistive switching	[103,114,117]
Carbon nanotube mixture, linked gold nanoparticles	Carbon nanotube, gold nanoparticle	Non-linear conduction properties introduced by an insulating phase in a conductive medium	Training through 'Evolution in Materio'	[15,99,118]

Table 1: materials studied to develop neuromorphic devices; in the table the composition, the switching mechanism and the properties of interest for technological application are listed. Main references are shown in the last column.

A case of particular interest is represented by systems characterized by a large number of metallic nanojunctions, show the appearance of non-ohmic behaviour under the current flowing [119,120]. High energy densities and non-linear electron conduction mechanisms trigger phenomena out of equilibrium with atomic rearrangement [119]. The collective behaviour of the synthesized materials shows emergent non-linear electrical conduction properties, multiple resistance states and conductance evolution under the application of an external field that resembles that of synaptic activity [78,102,103,109].

These properties emerge from a recurrent structure at the nanoscale, that strongly influence the electrical transport properties [8,17,109]. All the mentioned systems present the advantage to be self-assembled, with a simplicity of design without losing of the complex interconnections formed among the building elements [11,17]. Although the systems present interesting perspectives for processing information applications [18,114], like reservoir computing [102,103], practical demonstration of a device is still missing.

In this thesis, the use of cluster-assembled metallic films as a neuromorphic material application and a method to exploit their non-linear electron transport properties is presented. Recently it was demonstrated that nanostructured Au films fabricated by bare gold nanoparticles produced in the gas phase and deposited by supersonic cluster beam deposition can be reversibly switched between low and high conductance values [105,109,110,116]. They present a threshold voltage for the appearance of the switching activity, recurrently and discrete explored resistance states dependent from the structural features of the cluster-assembled film (average thickness, resistance value reached on the percolation curve) [109,121].

In data processing with artificial systems, nonlinear projection into a high-dimensional feature space can make data linearly separable, simplifying the classification of complex features. Such nonlinear projections are computationally expensive in digital computers. A promising approach is to exploit cluster-assembled films to perform this nonlinear projection intrinsically, because of their high computational density, inherent parallelism and energy efficiency.

The possibility of fabricating a device, called “receptron”, made of a generic pattern of electrodes interconnected by cluster-assembled Au film with a thickness above the electrical percolation threshold is here proposed and discussed.

1.4. Thesis Outline

This thesis work is focused on the fabrication and characterization of cluster-assembled nanostructured gold films showing a non-ohmic electrical behaviour and complex and reproducible resistive switching. My work was directed to demonstrate that the electric conduction properties of Au cluster-assembled films are deeply affected by their nanocrystalline complex structure characterized by both very high density of grain boundaries and crystalline orientation mismatch. The obtained experimental results showed that the flow of electric current gives rise to inter-cluster and intra-cluster rearrangements. The non-linear electric behaviour of cluster-assembled gold films is remarkably stable and reproducible allowing the facile training of the devices on precise resistive states.

Having acquired a detailed knowledge on the physical properties of cluster-assembled gold films, my goal was to show the possibility of fabricating a device based on cluster-assembled Au film able to perform classification tasks exploiting the emergent complexity of the system. In particular the efforts have been directed to the fabrication of a device that can receive complex inputs and generate a complete set of Boolean functions of n variables.

In **Chapter 2**, cluster-assembled materials are briefly presented, highlighting the structural and conduction properties. In **Chapter 3**, the fabrication technique and the experimental methods used in this work are presented. **Chapter 4** presents the results obtained about cluster-assembled gold film from the characterization of structural and electrical conduction properties. The emerging resistive switching behaviour and the temporal correlation in measured resistance data series are discussed.

In **Chapter 5**, the electrical behaviour of a cluster-assembled film subject to signals applied to separated regions is reported. The emerging spatial correlation among the conductive properties of different regions are discussed. In **Chapter 6**, a device based on a cluster-assembled gold film, capable of processing and classification of input electrical signals, is described and the experimental tested performances reported. In **Chapter 7** the conclusions emerging from this work are discussed.

2. Cluster-Assembled Metallic Films

2.1. Fabrication of Cluster-Assembled Metallic Films

The fabrication of cluster-assembled films relies on nanoscale building blocks that maintain, at least partially, their original structural and functional properties once assembled on a substrate [122,123]. Since I will consider systems composed by metallic clusters or nanoparticles with no protective shells, I will concentrate only on physical fabrication methods based on gas-phase technologies.

In gas phase synthesis, nanoparticles are made by "building" them from individual atoms or molecules up to the desired size: cluster embryos are formed either by physical means such as condensation of a supersaturated vapor or by chemical reaction of gaseous precursors [122,124]: Figure 2-1 shows schematically of the nanoparticle growth process.

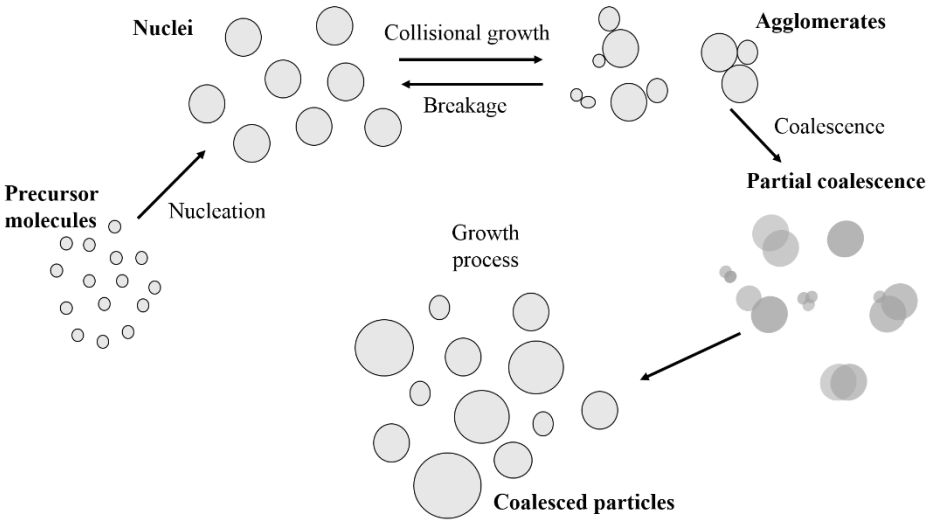

Figure 2-1 Scheme of nanoparticle growth process in gas phase. The precursor from which the growth starts are the atoms or molecule disperse in an inert gas. Nucleation processes form the first agglomerates. Collisional phenomena tend to increase the size or to break the preformed agglomerates. Coalescence in agglomerates takes place and particle size increases.

Depending on the embryo concentration, system temperature and pressure, clusters continue to grow to larger entities by coagulation and coalescence and/or surface growth, finally forming a suspension of particles in a gas (aerosol) [124,125]. The starting material can be vaporized from a hot source into a low-density inert gas employing Joule heating, laser ablation, arc discharge or sputtering [122,124,126].

Different cluster production techniques are more or less suitable for scale-up, while maintaining a tight size distribution and/or chemical composition: aerosol sources can produce nanoparticles in

bulk quantities, but they have the drawback of a limited control of particle size distribution and on particle manipulation in the gas phase resulting, in a poor control of lateral resolution of the deposited particles [124]. High lateral resolution can be obtained by cluster beam deposition based on supersonic gas expansion techniques [127], Figure 2-2 is a schematic representation of a typical cluster-beam deposition (CBD) process.

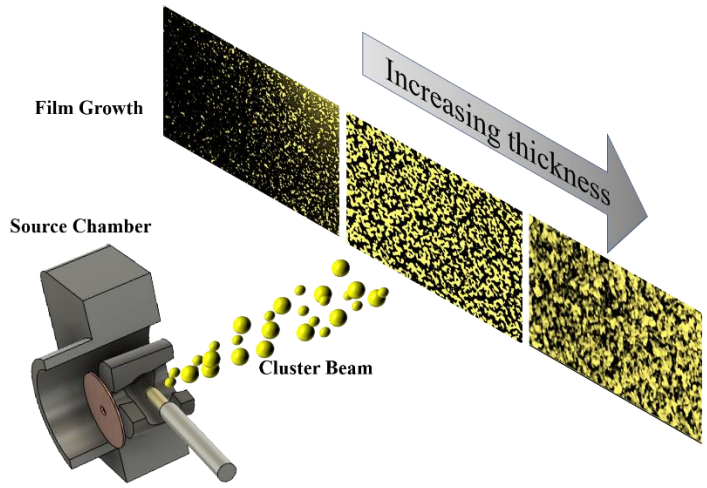

Figure 2-2 Schematic view of the deposition process of clusters on a surface from the gas phase. Clusters are produced by a suitable source chamber and subsequently deposited on a substrate.

Sputtering of a target in the presence of an inert gas is one of the most popular and widely used methods to produce metal cluster beams [128]. The coupling of a magnetron plasma source to a gas-aggregation cell for CBD has been proposed by H. Haberland and co-workers [129]: in the original design, the magnetron discharge is operated at a pressure of about 1 Torr to favor aggregation of the sputtered species; clusters are carried away from the formation region by the gas stream. Sputtering sources produce a large amount of ionized clusters that can be accelerated in a second chamber towards a biased substrate. By varying the distance between the magnetron unit and the orifice, the cluster residence time and hence the mass distribution can be controlled [130].

This approach has been developed and refined along the last couple of decades to achieve a very good control on structure and stoichiometry of the produced clusters; considerable efforts have been also directed toward an increase of production rate and cluster manipulation after the extraction for the source [124]. Deposition rates depend on the different sputtering source designs and the growing parameters used such as geometry of the vacuum chambers, carrier gas pressure, the ionization degree of the nanoparticles, etc. [131]. Despite significant progress, magnetron sputtering remains a technique limited by a rather low cluster deposition rate [128], basically due to the difficulty

of efficiently extracting the nanoparticles from the condensation region of the source [130]. The continuous working regime, typical of this class of sources, severely limits the use of supersonic expansions as a tool for cluster manipulation in flight and focusing [122,130].

2.2. Growth of Nanostructured Films

The presence and the evolution of defects in metallic thin films, depending on their thickness and growth conditions, have important consequences on the electrical conduction properties, in particular with a significant increase of resistivity values compared to the corresponding bulk materials [132–136]. Electric transport in polycrystalline thin films characterized by a high number of defects and grain boundaries has been extensively explored due to the need of extremely high integration of devices and hence the reduction of the dimensions of interconnects [137–139].

Here I consider the growth mechanisms of cluster-assembled films with particular focus on the differences from the growth of atom-assembled metallic films and on the factors that can influence and determine their morphological properties at the nanoscale.

2.2.1. Background: atom-assembled metallic films

Polycrystalline thin films grown by atom assembling exhibit a wide variety of microstructures characterized in terms of grain size and crystallographic orientation, lattice defects, phase composition, and surface morphology [140–142]. The Volmer-Weber model describes the initial growth stages characterized by the formation on the substrate of isolated islands with sizes and shapes strongly dependent by surface and bulk diffusion [143]. The grains formed on the substrate in the first stages increase their lateral size with the thickness: the film microstructure typically evolves in a competitive fashion and the kinetic limitations typical of growth conditions far from thermodynamical equilibrium cause the formation of metastable phases and defects on the micro- and nanoscale [140].

Systematic characterization of the correlation between film structure and deposition parameters, during the past seven decades, have led to the development of the so-called structure zone models (SZMs) which systematically categorize self-organized structural evolution during physical vapor deposition as a function of film growth parameters [144,145].

The growth processes controlling microstructural evolution include nucleation, island growth, coalescence of islands, formation of polycrystalline domains, development and growth of a continuous structure. When surface diffusion rates are significant, film thickening proceeds through local epitaxy on individual grains. Grain coarsening, i.e., recrystallization through grain boundary can occur both during and after island coalescence [140,146].

The nucleation barrier is generally expected to be small, leading to randomly oriented islands, for low-temperature deposition on amorphous substrates [147]. During island coalescence, there is a strong driving force for coarsening through surface atom diffusion and grain boundary motion. The island with lower energy per atom consumes the others, resulting in a new single-crystal island as the system attempts to minimize the overall surface and interface energy. Coarsening during coalescence is the first and most active phenomenon leading to selection of preferred orientation [140,146].

With continuing deposition, the islands grow until they come into contact forming a metallic network which then "in-fills" to form a continuous film of thickness $t_{Continous}$. The dimension of the grains in such a type of metallic film usually increases with the average thickness in a wide range of thickness values (from few to hundreds of nanometers) [141,148]. As I will discuss in the following, this is a major difference with respect to a cluster-assembled film where the number of defects and grain boundaries does not depend on the film thickness.

2.2.2. Cluster-assembled film growth

Although one can expect that the use of clusters as building blocks causes substantial differences in the morphology, structure and functional properties of metallic thin films, compared to the atomic deposition [149], only very recently these aspects have been explicitly highlighted [109,110].

The growth of cluster-assembled metallic films has been studied mainly in the sub-monolayer regime with particular focus on transition metal clusters [150,151], noble metals [110,152–155], bismuth [156–158], tin [159] and antimony [160,161]. Nucleation and growth process of Bi and Sb thin films grown by atomic and cluster deposition has been characterized by Transmission Electron Microscope (TEM) [149,156] showing the high sensitivity of the film structure to the size of incident clusters. The increase of the size of incident clusters induces a decrease of the mean diameter of the supported aggregates. When the size of free low-energy clusters increases, their surface diffusion becomes low enough to neglect the growth of supported particles [149].

The growth by CBD of antimony films has been modelled as the filling of a random network in the percolation model. This allows quantitative predictions of the electrical conduction threshold (as we will discuss in the next paragraph), coverage rate at the threshold, fractal dimension of the percolating path and multifractal properties of the cluster-assembled films [149].

Transition metal nanostructured films grown by SCBD have been characterized by AFM [150]. The observed morphology is characterized by nanoscale porosity, poorly connected and non-compact structures with lower density respect to bulk and a surface roughness increasing with film thickness.

The growth processes of cluster assembled gold films have also been studied starting from the sub-monolayer regime. The deposition of size-selected gold clusters produced by a laser vaporization source on HOPG has been reported [155]. The evolution of the cluster density can be described by a ballistic deposition model [162], cluster coalescence or re-arrangement is not observed demonstrating that the crystalline structure of the preformed clusters is conserved upon deposition and that no evolution of grain boundaries is present [154,155,163].

2.3. Electrical conduction properties

2.3.1. Percolation theory

Percolation theory describes the electrical conduction in systems composed by small conductive units mutually connected [87,164], correlating the morphological and the conductive properties of a thin metallic film. The notion of percolation is related to the study of paths formed by the elements composing the system: one can consider a lattice where a particle is represented by an occupied site (Figure 2-3). The percolation threshold is reached when at least one continuous path of contiguous occupied sites is formed.

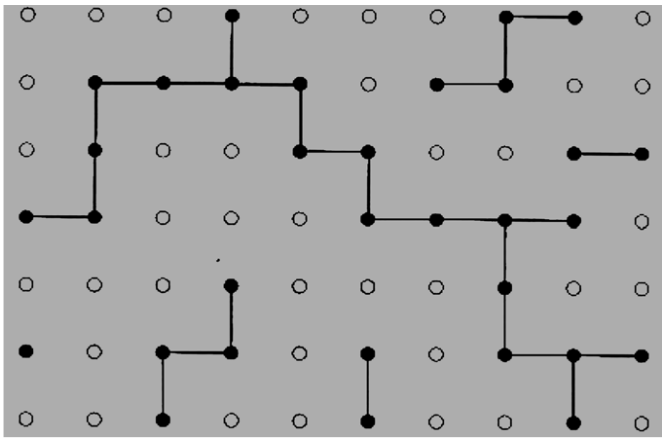

Figure 2-3 example of percolation on a lattice. The sites of the lattice can be unoccupied (white) or occupied (black). One percolation path is formed along the occupied ones. Figure from [165]**.**

Percolation phenomena are present in different systems, such as porous media, spread of diseases and fires, gelation and glass transitions [164]. In particular the percolation formalism has been used to describe the thin film growth process from discontinuous to continuous states [151,166,167], the metal/insulator transition in nanocomposites [168] and the divergence of electrical conductivity and dielectric constant in sintered composites consisting of micrometres-sized powders [169].

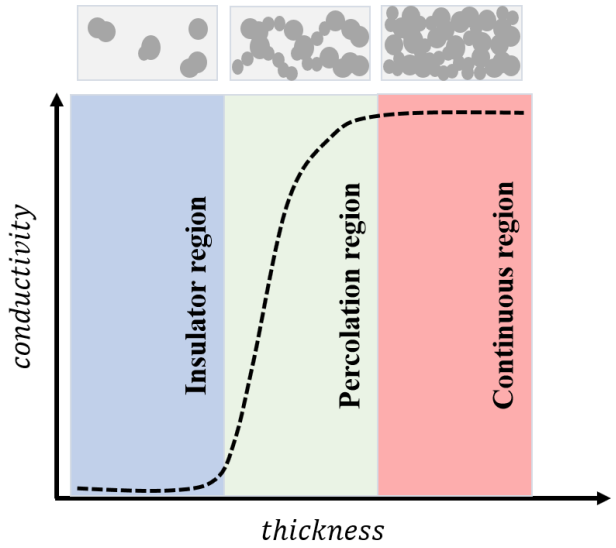

Figure 2-4 Example of percolation curve: conductivity vs. thickness. Top: the three principal growth stages are shown with a schematic view of the particle arrangement on the surface.

Percolation theory can describe a system of interconnected metallic nanoparticles (Figure 2-4): the evolution of electrical conductivity of thin metallic films as a function of their thickness follows the variation of the connectivity the particles on the substrate [151,164,166]. Thin films undergo, during the growth process, three fundamental electrical conduction stages: an insulating one, where only isolated aggregates are present on the substrate; the percolation stage, where the film is still discontinuous but the islands begin to join, forming conductive paths; the continuous stage, where a continuous layer is formed. Near the percolation threshold the electrical conductance G obeys a power law,

$$G \propto (p - p_c)^q \tag{3.1}$$

where p is the fraction coverage and p_c is the critical faction, two quantities strictly related to the thickness [151,170]; the exponent q has a universal value and it depends only on the dimensionality of the system. Several experiments demonstrated that the conduction properties of thin films are related to the percolation one and that the metal insulator transition can belong to the same universality class of the percolation problem [110,151,157,166].

When granular systems formed by metal nanoparticles are considered, some care must be taken with the concept of geometrical contact. In particular, standard percolation theory considers the conducting particles as either electrically connected, with some finite inter-particle conductance, or disconnected [87,164].

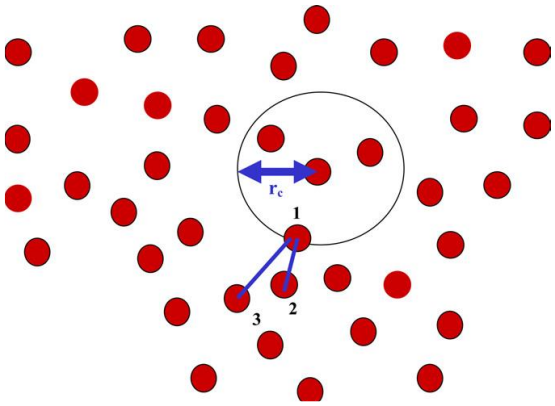

Figure 2-5 A random ensemble of spheres (red circles) of a small radius b with a uniform concentration of *N* spheres (indicated in the figure in the circular region) per unit volume (area). The topological requirement for a spanning percolation cluster is an average of *B*c bonds per site. This means that the local connectivity criterion is determined by the 'excluded' volume. Three neighbouring spheres and typical near neighbour distances are indicated in the figure. From [165]**.**

Below the percolation threshold p_c the resistivity is infinite because there is no spanning cluster network of connected particles. This notion of a sharp cut-off applies well only to composites made of large conducting particles (in the micrometric scale), for which two particles can be considered electrically connected only if they essentially touch each other. However, when the nanostructured system is formed by elements and structures having sizes limited to a few nanometres, the presence of this sharp cut-off is less clear. As often it happens in such cases, even if the particles do not physically touch each other, like shown in Figure 2-5 electrons can still flow from one particle to the other if their separation is low enough that tunnelling processes can occur [165,168]. In particular, below the critical transition point p_c the tunnelling process is the main mechanism that contributes to the conductivity of the system [165,168].

In the insulator-conductor transition region, metal particles begin to touch each other, leading to the formation of conductive paths. In this regime, nanogranular systems exhibit a feature common to most random insulator-conductor mixtures, once a critical volume fraction of the conductive phase is reached, a sharp increase of the conductivity is observed (Figure 2-4). The electrical conduction is due to both percolation along the forming metallic network and electron tunnelling between isolated particles. By further increasing the volume fraction of the metal fillers, tunnelling effects become less and less relative than the contribution of percolation [150,158].

Once a continuous layer is formed, an ohmic type conduction should be reached, however, the presence of an extremely high number of defects and grain boundaries typical of cluster-assembled films regardless the thickness may have a profound influence of the conduction regime [134,136,171]. The role of defects on electrical conduction of polycrystalline thin film has been extensively studied, much less is known about cluster-assembled nanostructured film. As we will see,

an extrapolation of the polycrystalline film behaviour to the nanogranular case is not justified by recent experimental results [110].

2.3.2. Electrical conduction in thin metallic films

Percolation theory gives a broad description about the connection between the morphological and the electrical conduction properties. It does not give an insight into the mechanisms that determine the electron conduction into a medium. Along the three fundamental growth stages of thin metallic films different phenomena can be involved into the electron flowing under an external field.

The insulating stage is characterized by the lack of conduction under the application of an external voltage bias since isolated aggregates are present on the substrate. Only under certain conditions, high particle density and low interspacing distance, conduction can take place. In this case, the mechanisms are related to the presence of a barrier among the islands [172]. The principal phenomena that determine the conduction are thermal emission, Schottky field emission and tunneling [142].

Percolating regime is hard to be described invoking a single conduction mechanism [142]. The structure at the nanoscale is characterized by interconnects, bridges and gaps among metallic islands and the resistivity shows a strongly non-linear behaviour as function of the thickness. S. Brown and co-workers demonstrated the electrical switching behaviour and quantized conductance at room temperature in percolating films of nanoparticles [157,158]. They showed that percolating systems of randomly deposited nanoparticles exhibit room temperature quantized conductance and switching, both during, and in response to, applied voltages. They attributed this behaviour to the formation of atomic-scale wires within the gaps in the film of particles [103,157]. The characteristics of this percolating-tunneling systems are similar to those of memristors [173] and may be exploited for the fabrication of neuromorphic devices [103,114].

In the past, greater efforts were addressed to describe the electronic conduction in continuous metallic films. In this stage, deviation from a pure bulk conduction are observed since the low thickness of the films that introduce some constraints in the electron conduction, and a morphology that deviate from a crystalline one [134,136,174]. Several models were developed to integrate in the semi-classical theories of Sommerfeld for the metallic conduction, the dimensionality effects due to the presence of the surface and the grain boundaries [134,171].

In polycrystalline metallic films, the conduction is dominated by the three principal scattering sources: 1) the scattering inside the single grain region (the volume or background scattering), 2) the scattering at the grain boundaries and 3) the scattering near the surfaces [136]. The first attempt to build a model that describes the conduction of continuous metallic films is due to Fuchs and

Sondheimer [132,133]. The proposed model considers the scattering near surfaces for film whose thickness is comparable to the mean free path. A formula for the film conductivity σ as function of the thickness t was derived by Fuchs in 1938 solving the Boltzmann transport equation [132], modelling the surface scattering as especial boundary conditions for the electron velocity [132,133]:

$$\frac{\sigma_0}{\sigma} = 1 - \frac{3}{2}(1-p)\frac{l_\infty}{t}\int_1^\infty (k^{-3} - k^{-5})\frac{1 - e^{-\frac{tk}{l_\infty}}}{1 - pe^{-\frac{tk}{l_\infty}}}dk \qquad (3.2)$$

where p is the fraction of electrons elastically reflected at the surfaces, against the fraction 1-p that is diffusively scattered, and l_∞ the mean free path of the of an infinite thick film and σ_0 the bulk conductivity. Two simplified expressions were given by Sondheimer [133] in the limit of thick film ($t > l_\infty$)

$$\frac{\sigma_0}{\sigma} = 1 - \frac{3}{8}(1-p)\frac{l_\infty}{t} \qquad (3.3)$$

and in the limit of thin film ($t < l_\infty$)

$$\frac{\sigma_0}{\sigma} = \frac{4}{3} - \frac{1-p}{1+p}\frac{l_\infty}{t\ log(t/l_\infty)} \qquad (3.4)$$

In the case of continuous film, the formula 3.3 is that practically employed for calculations. In this model the surfaces of the thin films are considered planar and the scattering process independent by the angle of incident, this last hypothesis was discussed by several authors [175]. Instead, the role of surface roughness was considered into other models like those reported in [175,176]; note that the Namba model gave interesting results compared to experimental data [136]. In all the listed models the scattering processes that regulate the electron conduction are that related to volume and surface scattering.

Mayadas and Shatzkes proposed the first model where the three types of electron scattering are simultaneously considered [134]. The grain boundaries are modelled like parallel and equally spaced planes, perpendicular to the electric field responsible for the electron motion. In the proximity of each plane, a short-range and smooth potential acts to disturb the electron motion, so that only specular reflection is produced. Following the method previously described, the Boltzmann transport equation is solved for this problem [134,177] to find the expression for the conductivity σ_g due to grain boundary (the other scattering sources contributions, except for the surface one, are included like a relaxation time contribution [134]). The obtained formula:

$$\frac{\sigma_g}{\sigma_0} = 3\left[\frac{1}{3} - \frac{1}{2}\alpha + \alpha^2 - \alpha^3 \ln\left(1 + \frac{1}{\alpha}\right)\right] \qquad (3.5)$$

where $\alpha = \frac{l_\infty}{t}\frac{R}{1-R}$ (R is the reflection coefficient at the grain boundaries, it determines the fraction of electron secularly reflected). The total resistivity is recovered, solving the Boltzmann equation under the Fuchs boundaries conditions, now considering σ_g as the intrinsic conductivity [134]. Note two important aspects of the last model: 1) in the expression for the total conductivity, a general parameter for the mean free path cannot be defined. This is since polycrystalline films do not respect the Matthiessen's rule and the resistivity ρ_g cannot be expressed as the sum of the resistivity due solely to grain boundaries and to background resistivity [134,177]. The authors define an 'effective mean free path' $l_g = \frac{\rho_g}{\rho_0}\, l_\infty$ (we will discuss this point later in the text). 2) Both Fuchs-Sondheimer and Mayadas-Shatzkes have the same trend and well describe experimental data only for thickness well beyond the continuous threshold [136].

Hofmann and co-workers proposed an alternative calculation of the conductivity of thin metallic films including the contribution of grain boundaries scattering [171]: this consist in a quantum mechanical computation based on the matrix-transfer approach. The grain boundary potential is introduced in the Schrodinger equation in the form of a series of potential barrier that electron goes through along its mean free path. In this picture, the fraction of electron that are reflected with a reversal momentum causes a lowering of the current density. Only a fraction of the total conduction electrons density contributes to the current flowing. The model brings to a modified Drude formula [171,178]:

$$\sigma_\infty = \frac{e^2 n_b T^{*\frac{l_\infty}{D}} l_\infty}{m v_F} \tag{3.6}$$

where, T^* is the transmission coefficient, v_F is the Fermi velocity, m ois the mass of the electron, D is the grain size and n_b the electron density of a bulk material without grain boundaries. The formula can be interpreted considering that only a fraction $n_c = n_b T^{*\frac{l_\infty}{D}}$ of the bulk electron density gives a contribution to the conductivity (3.6). This model gives a new insight on the contribution of grain boundaries on the electron conduction, as different ratio between grain size and mean free path length can have different consequences (like a negative temperature coefficient of the resistance, see [171,179] for a detailed discussion).

Although the described models were often employed in the past to interpret experimental results [136,148,180], they present several limitations. The weak point is the difficulty of defining the mean free path in films with a high concentration of grain boundaries. In addition, none of the presented models consider the role of the disorder [177,181]. In fact, the grains have not the same dimensions and are not equally spaced, but they are modelled like a periodic potential [177] and only

a posteriori mean grain size is taken to predict the experimental data [171]. It is well known (see the works of Anderson [182,183] and Thouless [184]) that a disordered potential can cause localized states and the transport could not take place. This is the principal inconsistency of the Mayadas and Shatzkes model. The effect of disorder become particularly evident in very thin films [185–187].

For disorder it is intended a wide distribution in island size, interspace distance between grain and tortuous structure. In Figure 2-6 (a)-(d) the effect of different degrees of disorder and coalescence on the electron transport is shown. As a result, non-ohmic mechanisms together with a high degree of disorder can explain the non-metallic behaviour in nanostructures [186,187]. Figure 2-6 (e) shows the trend of the resistance as function if the inverse of the temperature for metallic films of different thickness [186,187]. In the shown graph, a trend typical for non-metallic systems, appears for the lower thickness values.

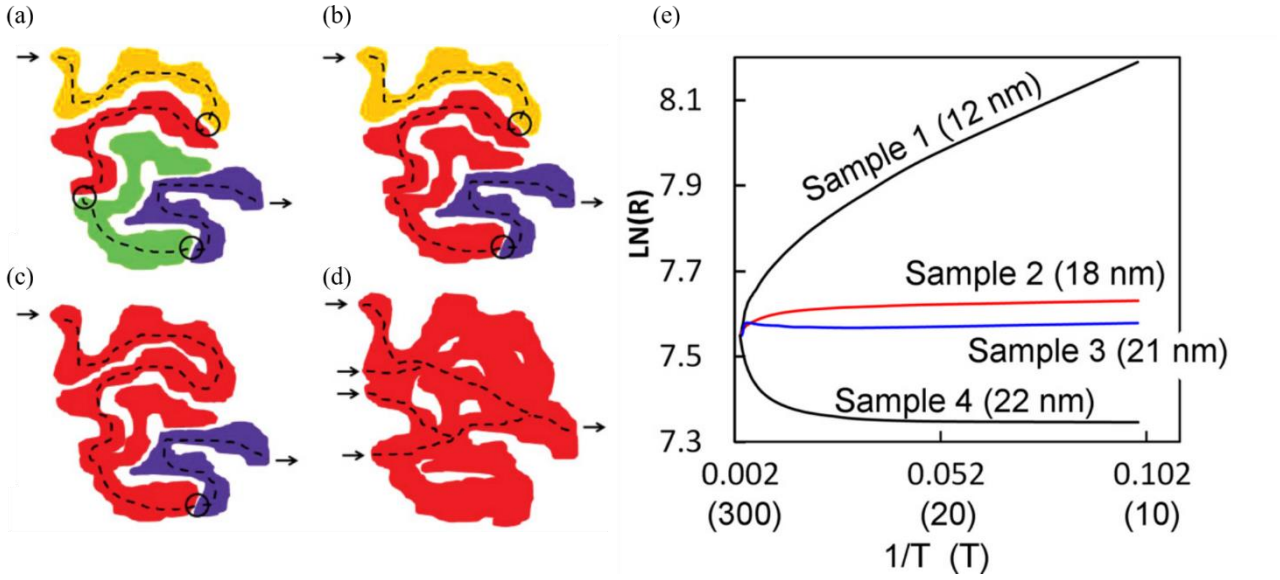

Figure 2-6 (a)-(d) Schematic electron transport paths (dashed line) in metallic nano-islands at different aggregation stages. From (a) to (d), coalescence at increasing thickness value is shown. With increasing thickness, the islands coalesce, and parallel electron paths appear. Taken form [187] **(e) The resistance vs the inverse of temperature is shown for metallic gold films at different thickness. The trend of the curves reflects the different involved mechanism in the electron transport at the nanoscale for different degree of coalesced islands and disorder. The thicker sample (sample 4) shows a metallic behavior, with the electrical resistance decreasing as function of the inverse temperature. The thinner sample (sample 1) shows a completely different behavior, similar to that expect for a semiconductor** [187]**.**

The strong influence exerted by a granular nanostructure on the electrical conduction properties of thin metallic films was studied in the past [188], however, a complete knowledge of the matter is still missing and there is not a global solution to the problem [181].

The presented results show two principal facts: 1) morphology and structure of the thin film at the nanoscale play an important role in regulating the global electron conduction; 2) Cluster-assembled film can present peculiar conduction properties due to their morphological properties.

3. Experimental methods

3.1. Supersonic Cluster Beam Deposition

An interesting evolution of CBD for the fabrication of cluster-assembled films is represented by Supersonic Cluster Beam Deposition (SCBD) that has been demonstrated as a scalable fabrication tool up to industrial processes currently in use [126,189]. SCBD is characterized by a high deposition rate, high lateral resolution (compatible with planar microfabrication technologies) and neutral particle mass selection process by exploiting aerodynamic focusing effects [124]. SCBD is currently an enabling tool for the large-scale integration of nanoparticles and nanostructured films on microfabricated platforms and smart nanocomposites [190]. A typical SCBD apparatus is schematically shown in Figure 3-1.

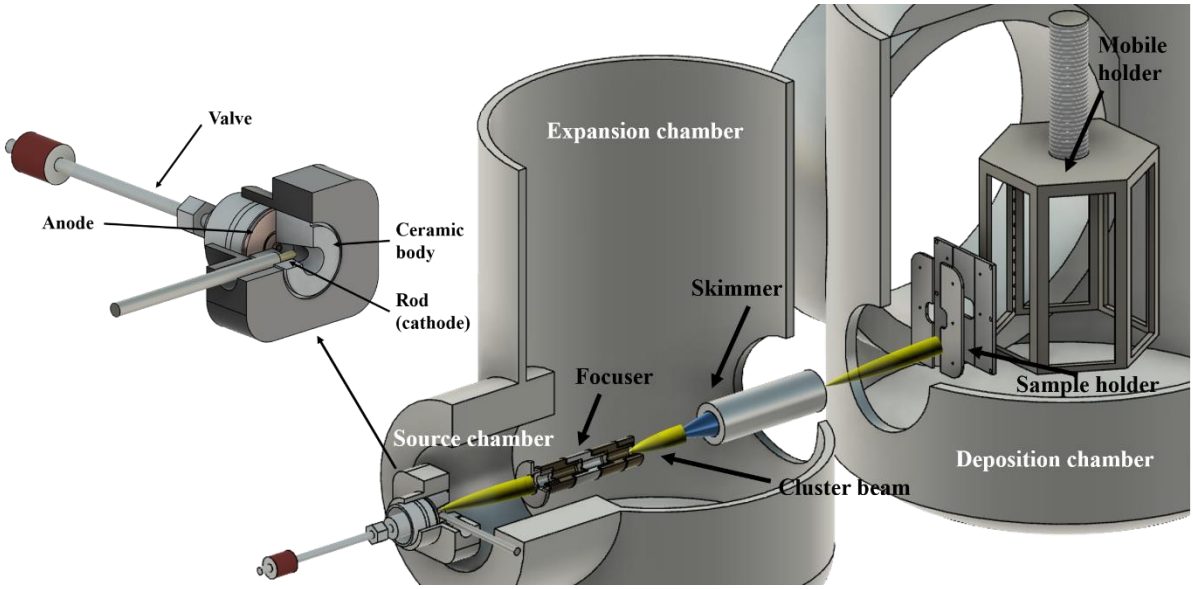

Figure 3-1 Scheme of the SCBD experimental apparatus. Clusters are produced in the source chamber and then extracted into the expansion chamber where they undergo a process of aerodynamical focusing. The focused beam arrives to the deposition chamber, passing through a skimmer. The cluster are deposited on the substrate mounted on the mobile holder. On the top left, an insight of the PMCS. The ceramic body consists in a cylindrical cavity where the gas injection is controlled by a pulsed valve. Between the ceramic body and the valve, a metallic disk, the anode is placed. The cathode, a gold rod, is inserted into the cavity through one lateral hole.

A source particularly suited to obtain intense and stable neutral supersonic cluster beams is the Pulsed Microplasma Cluster Source (PMCS), as described in detail in [191,192].

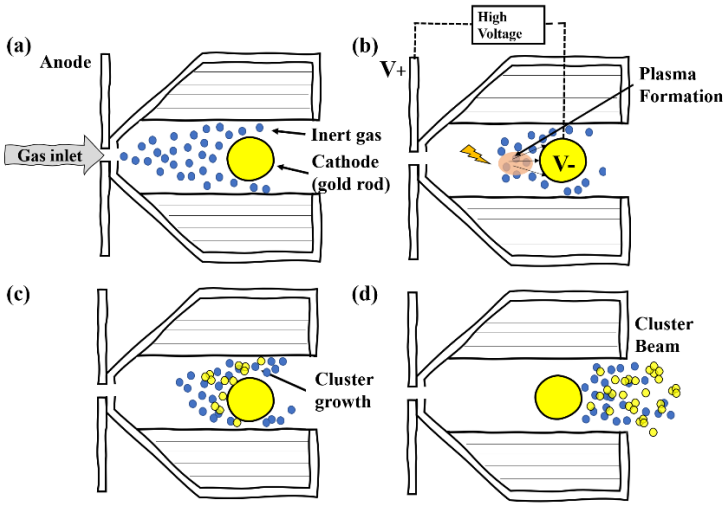

Figure 3-2 The working stages of the PMCS. (a) The injection of an inert gas into the conic chamber. (b) A high voltage is applied between the anode and the cathode (the rod). An electrical discharge ionized a small gas volume. (c) Atoms are extracted from the rod surface through the sputtering process and the cluster growth starts. (d) The seeded beam is extracted from the source chamber through the different pressure with the adjacent one.

Briefly, the PMCS principle of operation consists of the ablation of a metal target rod by a plasma ignited during the injection of a high-pressure pulse of an inert gas (He or Ar) [191,192]. The species resulting from the target ablation condense through collision with the inert gas to form clusters, then the cluster-gas mixture is expanded through a nozzle generating a supersonic seeded beam [193]. The working scheme of the PMCS is shown in Figure 3-2.

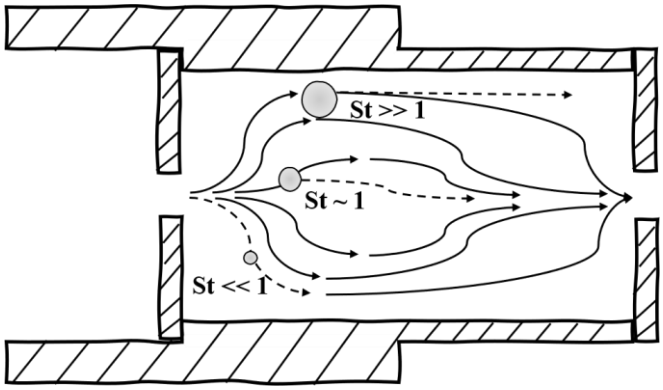

Figure 3-3 Schematic design of a focuser stage. The black arrows represent the streamlines of the gas flow that have different effects on particles with different inertial properties. Only particles with a Stokes number close to 1 slightly decouple from the streamlines and are concentrated along the focuser axis.

The cluster beam is focused by an aerodynamic lenses system [194] and directed on a substrate placed in a deposition chamber. The lenses force the gas flow lines to abruptly change when the gas passes through the orifice, obtaining a series of contractions and expansions during the passage

through the focuser stages. Each metallic particle follows the streamlines of the flow originated at the lens nozzle depending on its inertial properties. A scheme is shown in Figure 3-3.

A quartz microbalance periodically monitors the amount and the rate of deposited material and it allows to make an estimation of the nominal thickness of the films. High directionality, collimation and intensity of aerodynamically focused supersonic cluster beams, make them well suited for patterned deposition of nanostructured films through non-contact stencil masks or lift-off technologies [195,196].

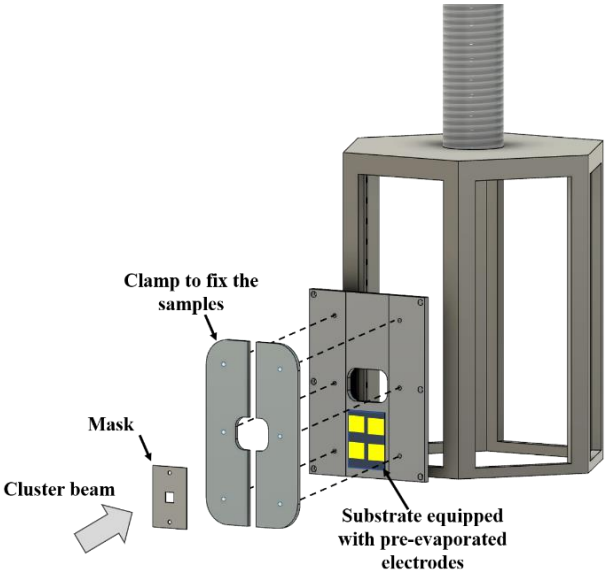

Figure 3-4 Scheme of the sample holder mounted on the manipulator during the deposition process. The sample is adjusted on the holder and fixed by two clamps. A mask is placed on the sample holder to intercept the cluster beam during the deposition and pattern the film on the substrate.

The evolution of the electrical properties of cluster-assembled films can be characterized in situ during the fabrication process: in Figure 3-4 I show schematically the configuration of the substrate holder for the in-situ electrical two-terminal device: the cluster assembled film is deposited by using a stencil mask [110]. The sample holder is equipped with electrical contacts for the in-situ characterization of the evolution of the electrical properties of the film during the deposition process.

3.2. Physical Vapor Deposition

Thin metallic films assembled by atoms were fabricated during my PhD work through the technique of Physical Vapor Deposition (PVD). The technique consists in bringing a material (gold) to a vapor phase and form a thin film through the sublimation of the evaporated atoms on the desired substrate.

In Figure 3-5 the scheme of the experimental apparatus is shown. A vacuum chamber is brought to high vacuum (10^{-4} mbar) through a diffusive pump after a pre-vacuum stage (5×10^{-2} mbar) reached by a rotary pump.

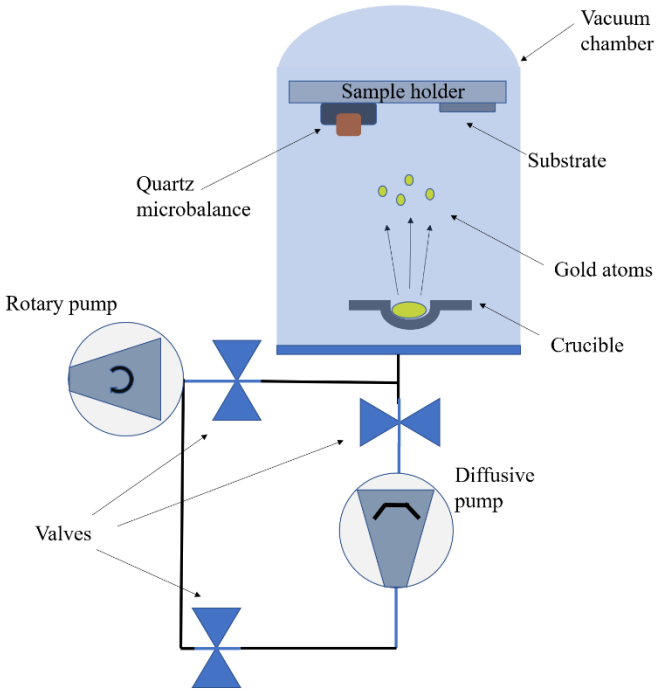

Figure 3-5 Experimental apparatus for the Physical Vapor Deposition. The crucible into the vacuum chamber is heated through an external controller and the gold is brought to its melting temperature. The atoms evaporated from the melted gold are deposited on a substrate. A quartz microbalance measures the nominal thickness of the fabricated film. A pumping system brings the chamber to high vacuum conditions.

The target material is placed in a crucible connected to a current generator and heated exploiting joule heating. The material is heated until it reaches the liquid phase in high vacuum condition. The atoms evaporated from the melted material can be deposited on the substrate laid down on the sample holder (Figure 3-5), monitoring the nominal thickness of the growing film through a pre-calibrate microbalance. The substrate, equipped with two pre-evaporated gold electrodes (not shown in figure) can be connected to a digital multimeter and measure the electrical resistance *in situ*, in order to obtain a percolation curve.

3.3. Characterization methods

3.3.1. Electrical characterization

The electrical resistance of cluster-assembled films was measured in the two-probe configuration [197], in Figure 3-6 a scheme of the experimental setup is shown. The sample is mounted on a holder

with two planar copper tapes to contact the electrodes, a voltage signal is applied and the current is measured through an Agilent E5280B, remotely controlled by a computer and the measurement is automatized through a Labview script. The resistance is computed as the ratio between the applied voltage and the measured current. The current measurements are carried out under continuous voltage and under pulses train.

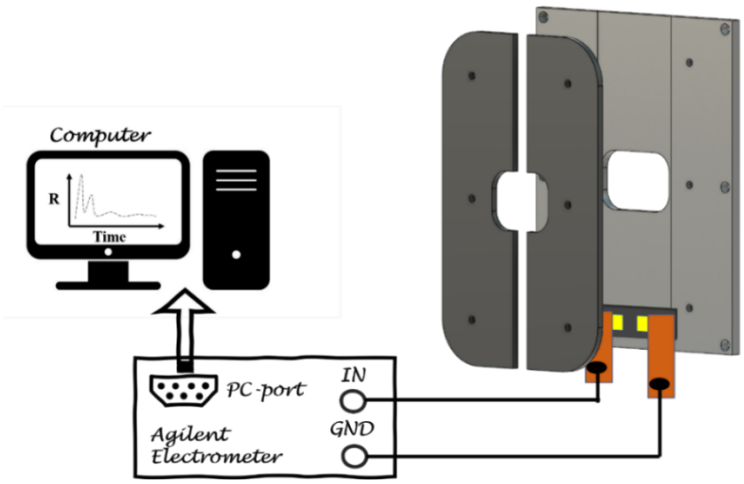

Figure 3-6 The setup scheme employed for the electrical characterization. The cluster assembled films are mounted on the holder where the two electrodes are connected to two copper contacts. The measurement is carried out in the two-probe configuration. The digital multimeter is remotely controlled by a computer.

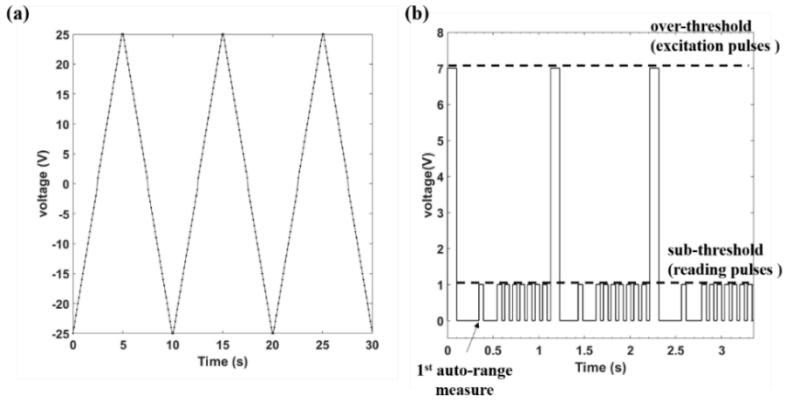

Figure 3-7 (a) Voltage ramp example where each ramp point is applied and the current is measured. The time interval between two consecutive points is 100 ms. (b) Pulse train example. The higher (excitatory) pulses are separated by small and briefer (reading) pulses. For each reading pulse the first one is employed to carry out an auto-range measurement to check the sample resistance value.

Continuous voltage is employed to evaluate the resistance evolution in time and to record the current-voltage curve. In Figure 3-7 (a) an example of voltage ramp is shown. The frequency of current measurement is 10 Hz (100 ms between two consecutive point ramps) and the maximum ramp

value is varied in the range 5 V to 40 V. Both positive and symmetric ramp (positive-negative voltage) are applied

An example of voltage pulses train is shown in Figure 3-7 (b). Between two high voltage pulse trains a 1 V pulse train of 0.07 s period, width 0.05 s is applied. The smaller pulses are considered the reading pulses, employed to measure the resistance and check the effect of the higher (excitation) ones. The height of the excitation pulses is varied in the range 5 V to 40 V, while the width between 0.1 s and 1 s.

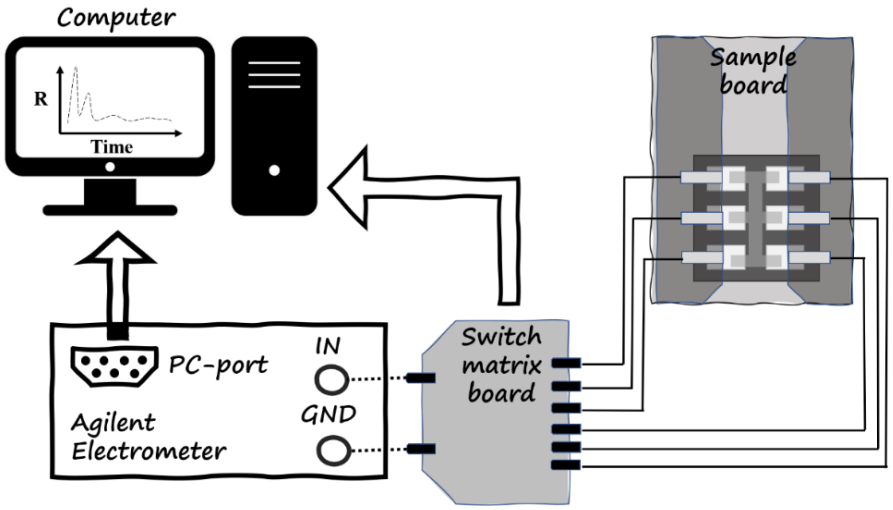

Figure 3-8 Scheme of the electronic setup for the measurement of multielectrode devices. The device is mounted on a board that connect each electrodes of the cluster-assembled film to a switch matrix board. The switches enable the selection of one electrode configuration. The measurement is carried out through an electrometer in the two-probe configuration. Both the switch board and the electrometer are remotely controlled by a computer.

A similar protocol is utilized to perform the resistance measurements for a multi-electrode device. In Figure 3-8 the setup is shown: each electrode is connected to a relay matrix that allows the selection of one couple of electrodes at the time, connecting one electrode at the voltage source and the other one to the ground. A pulse voltage train was applied to one couple of electrodes (values in the range -35 V to 35 V), followed by a train of small voltage pulses (1 V, period 0.07 s) to measure the resistance of all electrodes couples. This protocol allows to evaluate the effect of high voltage pulses that trigger the switching activity, through the measurements of the resistance under the small voltage pulses. In addition, applying the high voltage bias on one electrode couple, its effect on each other couple can be checked through the low voltage measurements.

3.3.2. Structural characterization

The surface morphology of nanostructured gold thin films was characterized in air using a Multimode Atomic Force Microscopy (AFM) equipped with a Nanoscope IV controller (BRUKER) [198]. The AFM was operated in Tapping Mode, using rigid silicon cantilevers mounting single crystal silicon tip with nominal radius 5–10 nm and resonance frequency in the range 250–350 kHz. Several 2 μm x 1 μm images were acquired on each sample with scan rate of 1 Hz and 2048x512 points. The images were flattened by line-by-line subtraction of first and second order polynomials in order to remove artifacts due to sample tilt and scanner bow.

Only globular objects from AFM images have been selected for the analysis of the cluster heights, by applying filtering selection criteria described in [199]. The height distribution of the objects identified is typically log-normal, as it is typical for systems resulting from aggregation processes [200], and they appear Gaussian in a semi-log scale [81]. The distributions have been normalized with respect to the total number of counted particles and the median value of each Gaussian is associated to the diameter (in z direction) of the gold clusters.

The electron microscopy was employed for the characterization of the samples with different thickness. The images were taken through Scanning Electron Microscopy (SEM) operating at 5 - 7 kV of accelerating voltage (SEM model Zeiss Supra 40), and through Transmission Electron Microscopy (TEM), even in High Resolution mode (HRTEM). The latter was performed by a ThermoFischer Titan Themis Z microscope operating at 300 kV of accelerating voltage, equipped with an ultra-bright Schottky (X-FEG) electron source, with a double spherical aberration corrector, and a 16MP CMOS Ceta camera. TEM/HRTEM imaging was performed on a thin film (average thickness 12 nm) deposited on an amorphous and thin (10 nm) substrate of silicon nitride.

4. Structural and Electrical Properties of Cluster-Assembled Gold Films

4.1. Structural properties

Morphological characterization was carried out for gold cluster-assembled films of different thicknesses. The percolation theory provides an adequate description of the evolution of the electrical resistance of thin metallic films as function of the thickness [87,169].

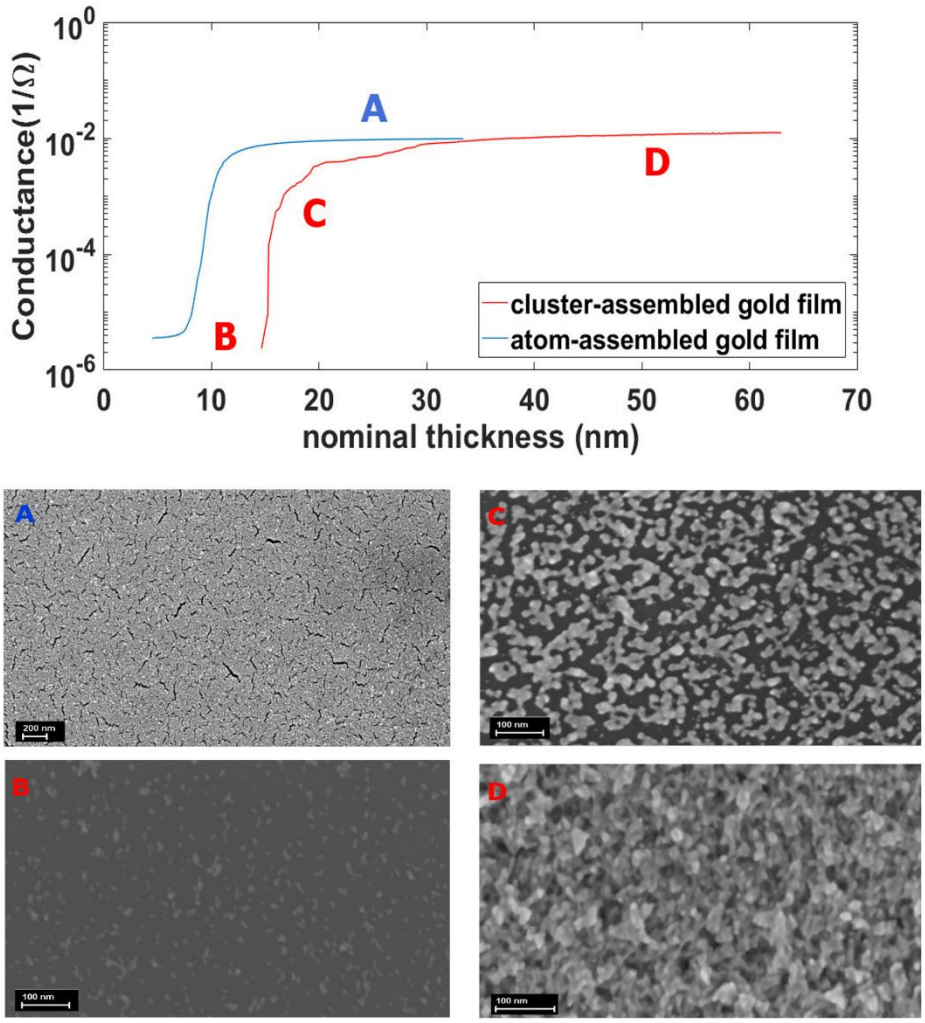

Figure 4-1 Top: percolation curves of an atomic-assembled gold film (blue) and of a cluster-assembled film (red), with the conductance (the inverse of the measured film resistance) on the y-axis in logarithmic scale and the film thickness on the x-axis; bottom: SEM images of the film morphology are associated to different film thicknesses and electrical behavior. A) continuous atom -assembled film (scale bar 200 nm). B-D: Images of the principal steps of growth of a cluster-assembled metallic films are reported counter-clockwise: B) insulating stage; C) close to percolation; D) conducting regime: a fully connected thick-film (scale bar 100 nm). From [109].

A quantitative analysis of the percolation curve, obtained fitting law (3.1) of atom assembled [167,180] and cluster assembled [151,160] metallic films can be found in literature. For cluster assembled metallic films fabricated through SCBD the scaling exponent is comprised in the range 0.41 to 0.78 [150] and it depends form the atomic specie and the growth conditions. Here I report a percolation curve obtained for cluster-assembled gold films (red curve in Figure 4-1). SEM images relative to the three fundamental regions are reported. In order to study how the growth and the resulting structural properties of cluster assembled films affect influence the evolution of the resistance, I fabricated an atom assembled gold film and measured a percolation curve (blue curve in Figure 4-1) to realize a comparison. The atom assembled gold film was fabricated through PVD on a substrate (Si with SiO_2 layer) of the same type of that used for cluster-assembled gold film, equipped with two pre-evaporated electrodes.

The three principal growth stages of a random assembling of nanoparticles are easily identified from the conductance-thickness curve. The conductivity of the cluster-assembled films (Figure 4-1, red curve) shows an insulating behaviour; by increasing the thickness, the first percolation paths are formed (geometrical percolation stage) and the conductivity abruptly increases, while the film is still in sub-monolayer regime. The critical thickness for the electrical percolation threshold, corresponding to the film morphology, can be determined by the occurrence of the maximum slope of the conductivity vs. thickness curve [201]. Beyond the percolation transition, the cluster-assembled film is fully connected, as shown in panel D, where a granular structure is still visible at this thickness value. In order to determine the thickness t_* at which the transition to a ohmic behaviour takes place, the minimum of the curve Rt^2 is searched, where R is the electrical resistance and t the thickness [170].

Although the percolation theory gives an adequate description of the evolution of the electrical properties of the cluster-assembled film, some care need be taken. For the sake of comparison, the evolution of the electrical properties of an atom-assembled film (blue curve) is also reported in Figure 4-1, showing the percolation threshold below 10 nm, instead, cluster-assembled films display higher threshold values, at thickness ~10-15 nm. The different surface mobilities of atoms and clusters are the origin of the different threshold thickness in the two systems [149]. For the atom-assembled films the transition to an ohmic behaviour occurs at a thickness around 12 nm, while the cluster-assembled film shows the same transition in a range between 18 nm and 25 nm. The morphology of an atom-assembled film is reported in the panel A, showing the typical structure expected for a film assembled by atoms [202], with evident differences with respect to the cluster film morphology in the continuous regime.

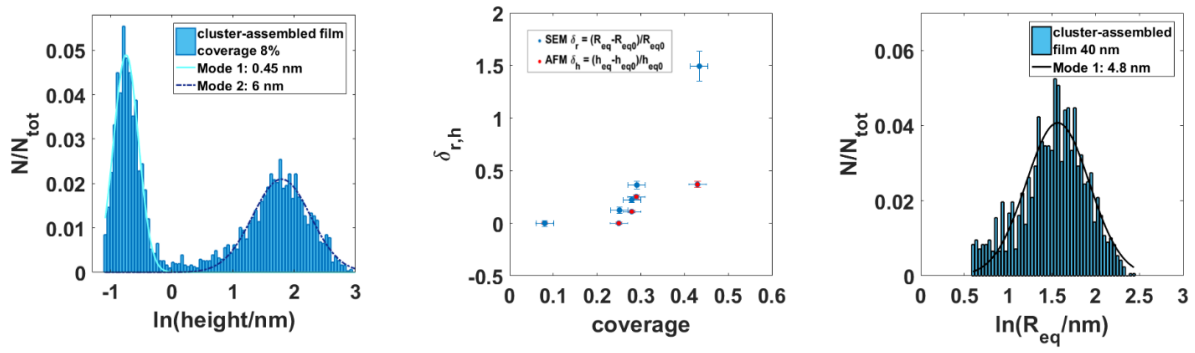

Figure 4-2 From left to right: (a) histogram in logarithmic scale of the height of the clusters measured by AFM on the smallest coverage sample. (b) relative island heights $\frac{h_{eq}-h_{eq0}}{h_{eq0}}$ (measured by AFM) and the relative radius $\frac{R_{eq}-R_{eq0}}{R_{eq0}}$ (measured from SEM micrographs) as a function of the coverage (the subscript '0' refer to the smallest coverage sample). (a) histogram of the equivalent radius of the grains obtained segmenting a SEM micrograph of the thick film.

Figure 4-2 shows the size distribution of the primeval clusters arriving on the substrate. In order to observe the grain size distribution and the growth dynamics characterizing their structure, a morphological analysis with atomic force microscopy (AFM) of the sub-monolayer cluster-assembled films has been performed. The results show a broad bimodal distribution of the particle heights: the smaller height peaked at 0.4 ± 0.1 nm, while the median value of the population of the largest clusters is around 6 ± 2.5 nm. The same analysis was carried out for the equivalent radius distribution, that is bimodal, with the main two peaks around 0.7 and 4.4 nm. Although the occurrence of aggregation processes on the substrate cannot be excluded, the distances form the observed islands prove that their coalescence is rare in this growth stage. This was also confirmed in previous results [203]: the distribution well reflects the real size of the deposited clusters. Since SEM images present more reliable evaluations in the lateral dimensions than the AFM (due to the tip-sample convolution [198]), I compared these results with the size distribution of the cluster sizes obtained from the SEM images of the same set of samples (details can be found in [203]). The results confirm that the size distribution of the primeval clusters is bimodal, and two class of particles are deposited: one formed by the smaller ones (< 1 nm) and the other one characterized by the bigger clusters (7 nm). This is due to the working regime of the PMCS: the two populations of nanoparticles result from different residence time of the sputtered gold atoms in the source chamber. The smaller one belongs to the cluster extracted from the chamber soon after the sputtering process took place, while the greater one derives from the clusters that reside for a longer interval time.

The native cluster sizes deposited on the surface strongly influence the film growth process. From the SEM images of cluster films with increasing thickness, interesting information can be gained. By increasing the surface coverage from 0.08 to 0.45 (Figure 4-1 panel c-d), the mean value

of the whole clusters heights increases of only 50%, on the other hand the equivalent radius increases of 160%. This suggests a preferential growth in x-y directions instead of z one in the first growth stages caused by the highest mobility of the small clusters [149].

The structure of the grains for very thin films (up to an average thickness 12 nm) has been observed through TEM microscopy in order to guarantee both the transmission of the incident electron beam and the observation of the first phenomena took place after the deposition. TEM observations shown in Figure 4-3, present a structure consisting of branched aggregates and also shows that such a structure is based on the hierarchical arrangements of small units in larger features up to a certain critical length-scale, determined by the time of the deposition process [109,199].

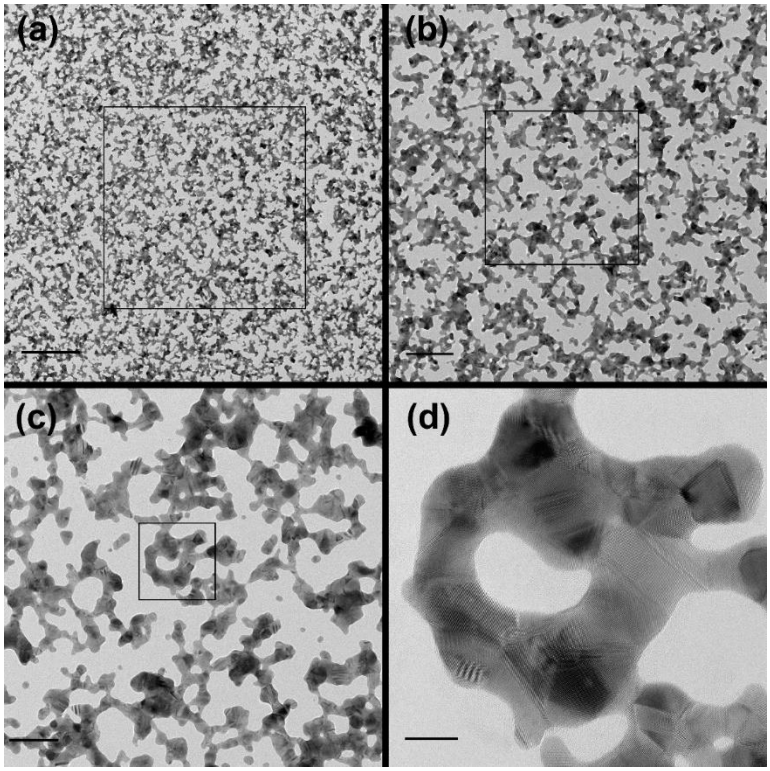

Figure 4-3 TEM/HRTEM images of the gold clusters. (a) Overall view of the percolating film, scale bar: 250 nm; (b) magnified view of the square reported in panel (a), scale bar: 100 nm; (c) magnified view of the square reported in panel (b), scale bar: 50 nm; (d) HRTEM image of the polycrystalline cluster surrounded by the square in panel (c), scale bar: 10 nm.

This can be explained by the primeval incident cluster size distribution: the surface diffusion on the silicon substrate and the nucleation for smaller clusters, initially result in a 2D growth, while larger clusters act as static nucleation sites where a 3D growth mode is promoted [199]. HRTEM characterization shows that the branched structures and larger aggregates are mainly constituted by several crystal domains grown without preferential direction, as expected for a deposition on an amorphous substrate. Figure 4-3 clearly displays two very important features typical of the deposited film:

1) its branched structure does not show any isolated cluster (see panels (a)-(c)), this meaning that the percolation threshold has been largely reached;

2) the HRTEM imaging (panel (d)) shows that the clusters constituting the thin film are in turn constituted by several crystal domains, with size (calculated as domain wall length) ranging between 5 and 10 nm.

Moreover, they are randomly grown and in different possible crystal relationships among them: some of them are twinned domains, while in other cases the domains are just separated by grain boundaries, often with frequent stacking faults, in order to minimize the surficial interface energy. Finally, in some cases a superposition of crystal domains is also observed, and that is easily identifiable by the presence of Moiré fringes. In general, what is indicated by the HRTEM imaging is that the occurrence of the above-mentioned different possible crystal domains configuration is very likely dictated by the local thickness: if it increases, the structure evolves from quasi 2D crystal domain to twinned ones, to further give rise superposition among them. In summary, the observed structures do not change their aspects varying the quantity of deposited materials, for thickness around 12 nm. This means that the particle aggregation during the first growth stages results always in a ramified and granular structure. In addition, the observation of different domain in films whose percolation threshold was reached and their dimensions, suggests that they are determined by the native cluster size deposited on the surface and survive increasing the quantity of deposited materials. To understand how this influences the conduction properties, cluster-assembled gold films with higher thickness were taken under study.

By continuing the deposition a fully connected film is produced (Figure 4-1 panel D, thickness 57 nm) and the growth is essentially ballistic beyond the continuous stage [199,204]. To extract a grain dimension in thicker films, a quantitative granulometric characterization of SEM images was carried out following the procedure in [199]. Briefly, the analysis aims to obtain the typical dimension of the grains deposited on the surface analysing the geometrical curvature of the grain regions in the SEM images. The surface is characterized by a grain distribution substantially similar to that of the sub-monolayer films (Figure 4-2 c).

I underline the fact that the grain distribution nearly perfectly overlaps with that of the sub-monolayer film, thus suggesting that no significant grain growth is present even for very high thickness and that the nanoscale building blocks retain their individuality [150,199,203]. This is at odds to what has been observed for the growth of gold films assembled by atoms: in this case the grain size increases linearly as films become thicker [146,205]. Figure 4-4 (a) shows the values of the mean grain size of three cluster assembled films with increasing size and these are compared with the theoretical grain size growth for atom assembled films found in literature [141,148].

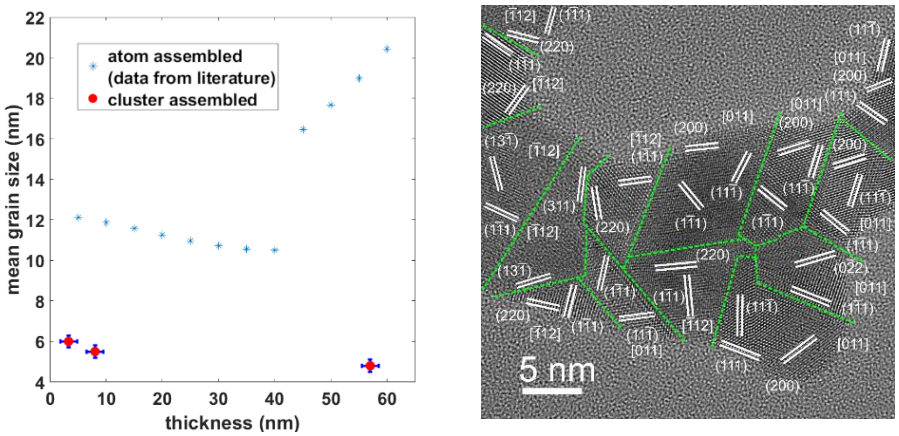

Figure 4-4 (a) Mean grain size as function of the thickness for a cluster-assembled and an atom assembled films (theoretical curve from [141]**). (b) HRTEM image of a typical region of a sub-monolayer cluster assembled film. Different crystal domain separated by grain boundaries are visible. For each single crystal domain, the corresponding zone axis [hkl] is displayed, after determination by local 2D-Fourier analysis of the relevant region of interest in the HRTEM image.**

The grain size of a cluster assembled film is constant for increasing thickness, on the contrary that of an atom-assembled film strongly increases for thickness greater than a certain threshold (about 40 nm). The atom assembled film morphology is characterized by islands that grow through nucleation or island coalescence, determining a lateral increasing of the grain size. On the other hand, the growth of the cluster assembled films is strongly influence by the native cluster crystal structure deposited on the surface. In Figure 4-4 (b) an HRTEM image of a sub-monolayer region of a cluster assembled film is reported. The aggregate is characterized by a crystal domain with size equal to the cluster one (compare with the highest peak of the cluster size distribution shown in Figure 4-2).

4.2. Electrical conduction properties

The morphological structure presented in the last paragraph causes interesting electrical conduction properties under the application of an external field. The behaviour of the continuous Au cluster-assembled film is non ohmic and characterized by the onset of switching activity with a series of discrete and reversible resistance variations [109]. Remarkably the I-V curve of the cluster-assembled film shows a non-linear behavior and the presence of hysteresis. The coexistence of reversible switching regimes characterized by very different resistance ranges has been reported in cluster-assembled gold films below the percolation threshold [116]. Quite unexpectedly a non-linear behavior is observed also for continuous gold nanostructured films. For the sake of comparison, an atom assembled metallic film was fabricated through PVD and tested on the a substarte of the same

type of those used or cluster-assembled film (Si with a SiO_2 layer). The design of electrode and relative dimensions are the same for the two classes of thin films (refer to inset in Figure 4-5).

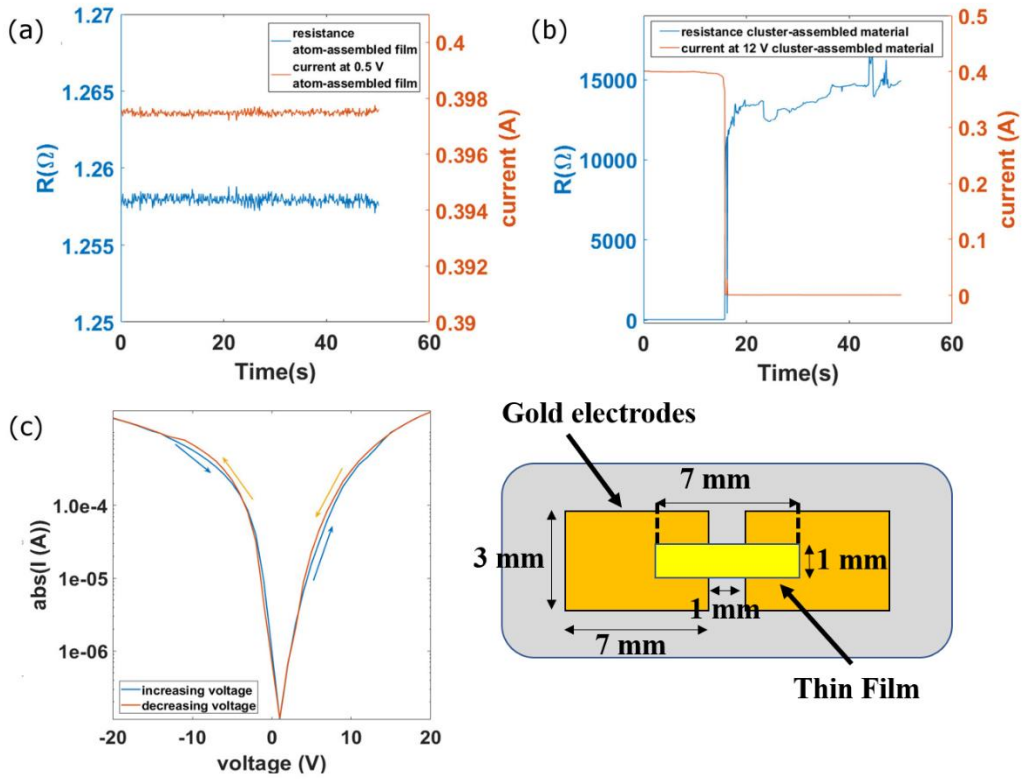

Figure 4-5 a) Measured electrical resistance and current of an atom-assembled Au film 100 nm thick as a function of time under the application of 0.5 V. b) electrical resistance and current of a cluster-assembled Au film 65 nm thick as a function of time under the application of 12 V in the proximity of the forming step; the current is approximately equal to that circulating in the atom-assembled film c) I-V curve of a cluster-assembled film 65 nm thick after the activation of the switching activity in semilog-y scale. Inset: the scheme of the device for the electrical measurements of both atom-assembled and cluster-assembled thin films.

In Figure 4-5 the graph of the measured electrical resistance under a constant voltage is reported both for an atom assembled (panel a) and a cluster assembled film (panel b) in the continuous regime. Cluster-assembled films are characterized by a higher initial resistance compared to the atom-assembled ones; for this reason, a larger voltage drop in the former is observed, for the same current circulating in both systems. As suggested by the semi-classical models of Sondheimer and Mayadas-Shatzkes [133,134], the difference in the resistivity values between atom-assembled and cluster-assembled films is explained by the presence of an extremely large number of defects and grain boundaries typical of the low-energy cluster beam deposition regime resulting in highly porous films [150,206].

The structural properties of cluster-assembled films have also other consequences on the electron transport properties. Gold cluster-assembled films present resistive switching activation under the

application of a voltage higher than a certain threshold. In Figure 4-5 (b) the switch activation is shown for a sample 65 nm thick under voltage bias of 12 V. The graph shows a jump in the measured resistance of two orders of magnitude. The resistance increase suggests that breakdown phenomena take place at the nanoscale under the application due to the dissipated power. The porous structure of the cluster-assembled film and the presence of necks and bridges at the nanoscale favor the occurrence of high-density current values that trigger local electromigration and joule heating phenomena [119,120,207].

After the activation, the films show a resistance switching behavior and non-linear IV curve. In Figure 4-5 (c) the trend of the current-voltage curve is shown with logarithmic scale on the y axis. The trend is non-linear, with a deep valley around 0 V due to the noise current measured when no voltage bias is applied, amplified by the log scale on the y-axis.

The resistance variations take place in a wide range of applied voltage bias 0.5 V up to 35 V with well-defined levels that are recurrently explored under the application of a constant voltage bias, and whose order of magnitude and occurrence depends on the applied voltage.

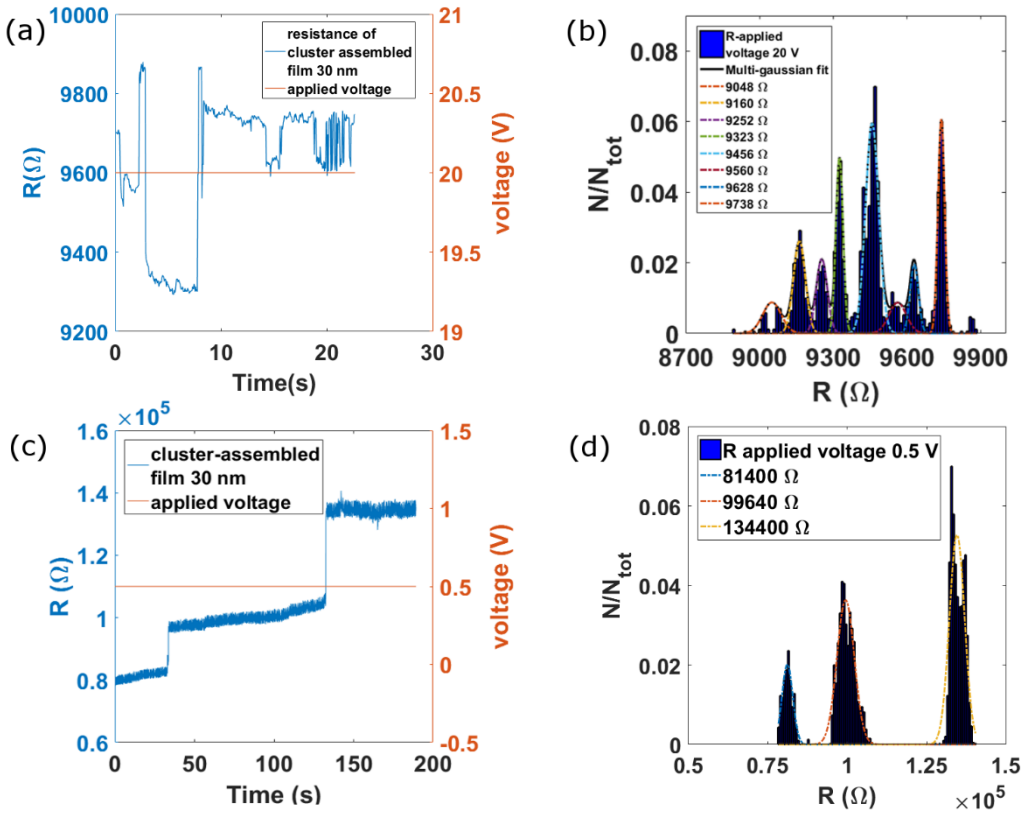

Figure 4-6 a) electrical resistance of a cluster-assembled film with thickness 30 nm under the bias of 20 V; several switch events in the interval time of 20 s are evident. b) histogram of the resistance values assumed by the sample under the application of 20 V in a time window of 200 s. c) electrical resistance of the same sample under the bias of 0.5 V. d) histogram of the resistance values assumed by the sample under the application of 0.5 V in a time window of 200 s.

Figure 4-6 reports two resistance patterns measured under the application of two different voltage biases. The histograms of the explored resistance levels are reported for each pattern. The current-voltage characteristic becomes non-linear after the switching activation, as shown in Figure 4-5 (c).

The main features of the resistive switching activity are shown in Figure 4-6. Graph (a) reports the evolution of the resistance for a cluster-assembled film with a thickness of 30 nm under the application of 20 V bias after the activation: typical switching features are present, consisting in reversible switches in different resistance ranges. This is quantitatively represented in the histogram of the resistance values under a bias of 20 V in a time window of 200 s. The histogram shows different gaussian type peaks around each resistance values reached after the switch events occur. The panels (c) and (d) report the results obtained under the application of 0.5 V. We will discuss later the influence of the applied voltage on the switching behavior.

In cluster-assembled gold films the granular structure at different length scales largely determines the non-ohmic electrical properties of the system. Although the elemental building blocks can be considered metallic, their assembly does not result in an overall ohmic conductor. The use of "good metal" building blocks to fabricate "bad metal" systems has been reported in the case of Ag films, assembled with traditional methods, where structural disorder at the mesoscale influenced in a substantial way the electronic properties of the system [208,209].

Electronic carrier conduction in porous systems can be considered to be based of space charge limited conduction mechanisms and coulomb blockade with very strong geometrical constraints [121,187]. The presence of an extremely high density of grain boundaries and crystalline orientation mismatch deeply affects the electrical conduction representing a barrier for the electric charge flow and resulting in a distribution of different "resistances" over the cluster-assembled film. The grain boundaries distribution can dynamically change under the current flow because of the formation of local "hot spots" that induce atomic rearrangement, and formation/destruction of contact depending on the power dissipated locally. For a deeper discussion see Appendix A and ref. [121].

These elements can explain the non-linear behavior and the presence of switching activity observed in continuous Au cluster-assembled films. Their structure and the presence of a granular structure also in the continuous morphology regime, introduce non-linear conduction mechanisms. This determines the global non ohmic behavior observed during the application of low voltages. The main phenomena that take place are Joule heating and electromigration phenomena [104,119,120,207,210]. Since they verified in a structure confined at the nanoscale the observed results can emerge. In a nanoscale junction, where the contact surface between grains is smaller than the mean free path of electron, small voltage drops (about 100 mV) can induce high temperature (up to thousands K) [120] causing the re-arrangement of the junction through defect displacement, atom migration and re-

crystallization [211]. In a cluster-assembled film, characterized by a granular structure, the momentum exchange between the mobile electrons and the atoms can cause the breaking/formation or purely rearrangement of nanojunctions and locally change the resistance. As result, the current flowing and the energy dissipation can give rise to rearrangement phenomena at the grain boundaries. The process is schematically shown in Figure 4-7.

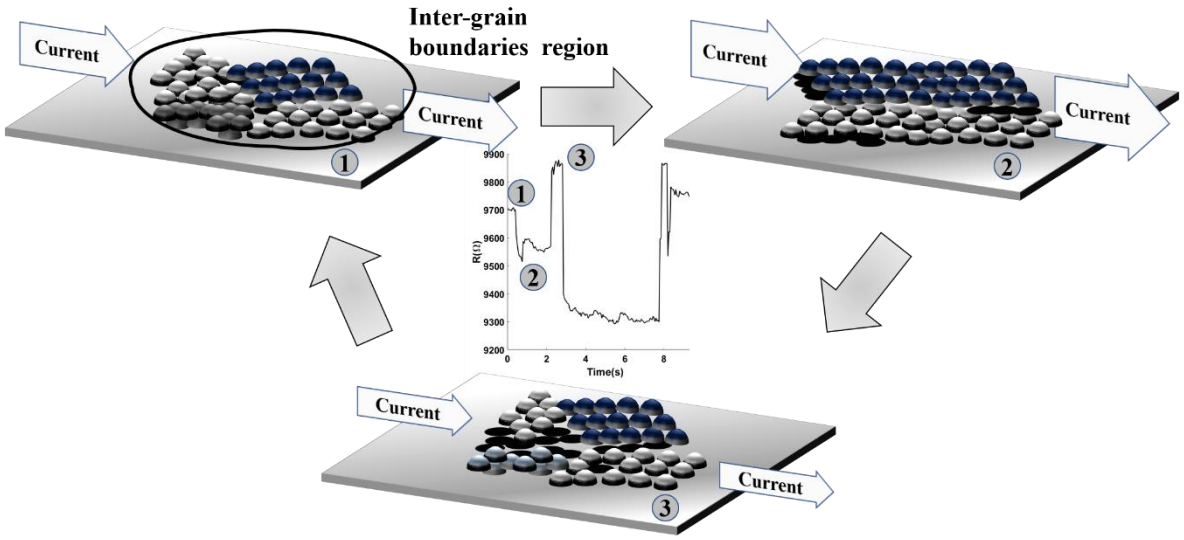

Figure 4-7 Schematic representation of the atomic rearrangements at a single grain boundary, due to current flow, giving origin to switch events. Different colors identify regions with different crystalline orientations. The starting configuration (1) represents the initial grain boundary atomic arrangement. During current flow through the boundary joule heating causes locally a temperature increase that favors crystalline plane rearrangement and defect elimination thus decreasing the local resistance (2). The higher current density causes further heating and breakdown of the electrical connection (3) resulting in a sudden increase of resistance. The current flow redistribution among adjacent regions causes further atom migration and reconstruction of the electrical connectivity between the grains (back to 1). This dynamical rearrangement is at the origin of the spiking behavior reported in the central panel.

The dissipated power can determine a local ordering of grains, with increasing the amount of current (passage from sketch 1 to sketch 2) [137,211,212]. On the other end, a critical current density can trigger the disruption of nanoscale contact (passage from sketch 2 to sketch 3). The observed behavior suggests that controlling the amount of delivered power, hence the applied voltage and flowing current, the switching activity can be influenced.

Cluster-assembled films with different thickness and in a different position on the percolation curve have been characterized, under the application of pulse train with controlled height and width (the measurement protocol is that outlined in chapter 3). By measuring the resistance with a low voltage pulse train, it is possible to probe the effect of the higher applied voltage. The fabricated samples are divided into two classes: those near the percolation threshold with High Initial Resistance (HIR) $10^4<R< 10^5$ Ω (thickness 10-15 nm, in the non-linear region of percolation curve, where a large resistance decreasing corresponds to a narrow thickness variation, see Figure 4-1, red curve), and

those in the continuous region with Low Initial Resistance (LIR) in the range 50<R<200 Ω (thickness 20-40 nm). The scheme of the device is the same for the two classes (refer to inset in Figure 4-5). For sake of comparison the SEM images of tow samples belonging to the two classes are reported in Figure 4-8 (a) and (b). In panel c the cross section of a LIR sample is shown.

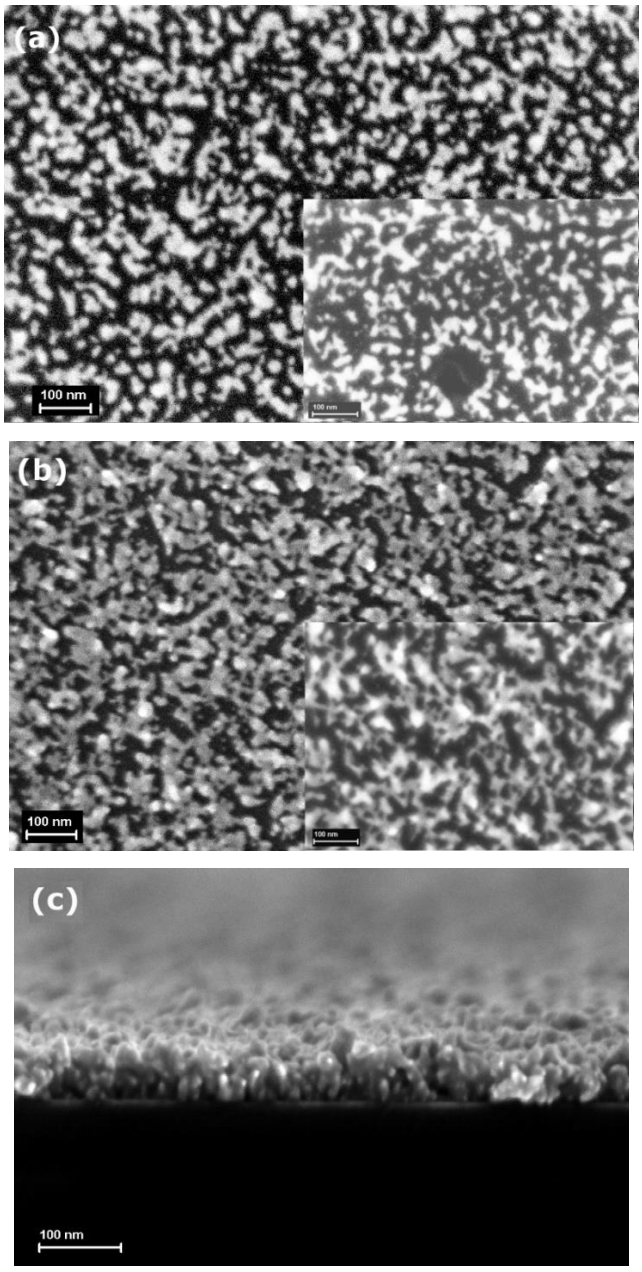

Figure 4-8 (a) Top-view SEM micrograph showing the surface morphology of a HIR cluster-assembled Au film (EHT 5.00 kV). The thickness of the film is 14 nm. The inset shows an enlargement where a poor connected film characterized by the presence of several isolated structures is visible. (b) Top-view SEM micrograph showing the surface morphology of a LIR cluster-assembled Au film (EHT 5.00 kV). The thickness of the film is 25 nm. The inset shows an enlargement where a fully connected network of cluster is clearly visible. (c) Cross section of a cluster-assembled films 57 nm thick (EHT 7.00 kV). The observed morphology is characterized by nanoscale porosity, poorly connected and non-compact structures with lower density with respect to bulk and increasing surface roughness with film thickness.

All the samples show the resistive switching activity although some differences appear: 1) the HIR samples do not need a switching activation, they show the pattern shown in Figure 4-9 since the application of voltage greater or equal to 5 V contrary to the samples beyond the percolation threshold; 2) the samples belonging to this class appear with a high degree of randomness (in Figure 4-9 it is possible to see the missing switching for some reading pulses).

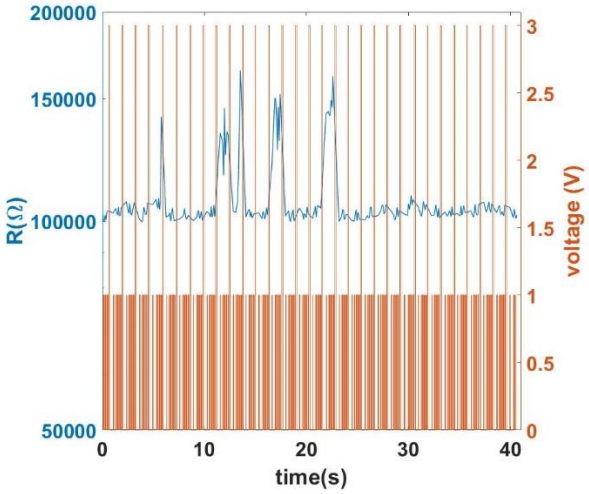

Figure 4-9: Switching activity of a HIR cluster-assembled film under the application of voltage pulses (3 V) (y axis in log scale). Reversible and consecutive events are observed due to the application of low amplitude voltage pulses.

LIR devices need a threshold voltage (whose value depends on the initial sample resistance) to activate the switching behaviour also under the application of a periodic voltage. At voltage pulses lower than the threshold value, the device shows an ohmic behaviour; approaching the threshold values the resistance undergoes an increasing trend as shown in Figure 4-10 (a). After the application of each excitation pulse, the resistance increases in time like an integration process in time. In addition, during the measurements through the sense pulses, it shows a sort of relaxation: a similar feature is observed in neural networks and it is described by the leaky integrate-and-fire neuron [213]. This type of behaviour is more clearly visible with 1 s width pulses. In Figure 4-10 the activation of switching activity takes place after the application of voltage pulses for a time window of about 100 s. The number of pulses needed to reach the activation step depends by the voltage level, the pulse width and the number of pulses. The activation voltage lies in the range 25 V up to 35 V and the process of activation is the same for all the LIR samples as shown in Figure 4-10.

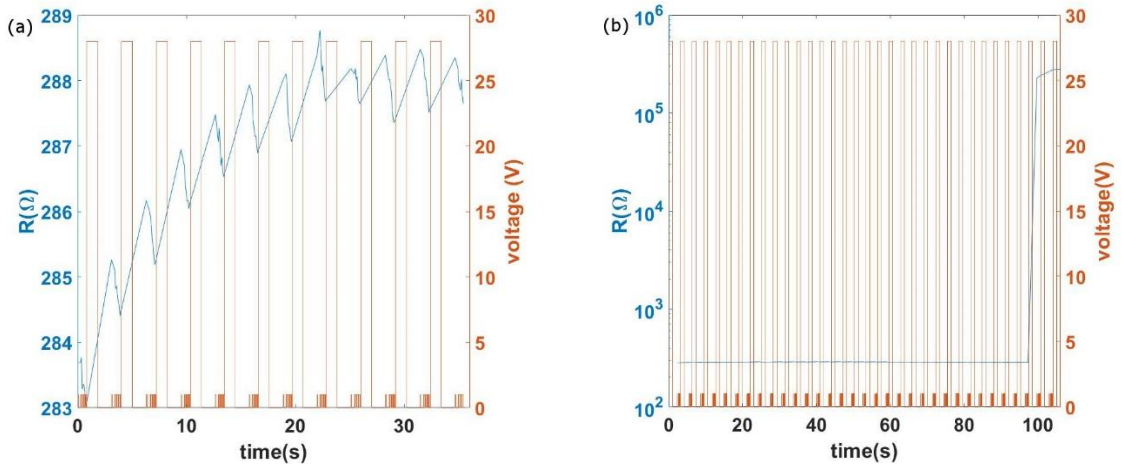

Figure 4-10. (a) Potentiation behavior of LIR samples under the application of a train of pulses near the voltage threshold (27 V in this case, width 1 s). (b) Switching activation of the LIR film (y axis in log-scale). After the potentiation trend shown in (a), the resistance abruptly increases. Note that the resistance scale does not allow to recognize the potentiation progression that appears as a straight line.

In Figure 4-11 the behaviour of the LIR device under the application of voltage pulses after the activation is shown: with 5 V pulses the device changes the resistance from the high to a lower level for almost one order of magnitude (Figure 4-11 a), while a transition to a higher resistance state under the application of 20 V pulses is observed (Figure 4-11 b).

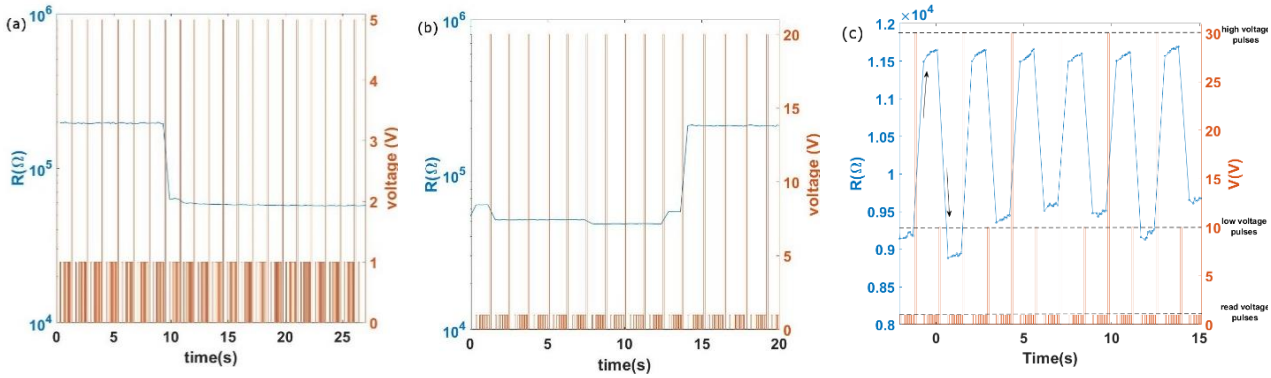

Figure 4-11. (a) Transition to a low resistance level under the application of low voltage pulses (5 V) for LIR sample (initial resistance 200 ohm). (b) transition to a higher resistance level under the application of high pulses (20 V) for the same sample as in (a). Y axis in log-scale for both graphs. (c) An example of consecutive transition from the higher resistance level to the lower one and vice-versa for a second LIR sample (initial resistance 120 ohm) observed under the application of consecutive low (10 V) and high (30 V) voltage pulses.

The switching from high resistance to low resistance levels is reproducible and stable over tenth of applied pulse train. The devices were tested several times at distance of hours with no significant differences in the switching activity. We observed that the reversible switching behaviour can be controlled tuning the pulse width and the height. For higher voltage pulses (beyond the activation level for LIR samples) 100 ms pulses are employed. In Figure 4-11 (c) consecutive and

reversible switches between higher and lower resistance state are shown with the applied pulses. The resistance level explored under the application of the pulses is random, the frequency of switch occurrence and their amplitude can be driven by the applied voltage pulses.

As pointed out previously, the observed switching behaviour in nanostructured Au films beyond the percolation threshold is quite unexpected. The morphological characterization reveals a deviation from the crystal structure and a grain size that does not evolve during the film growth. This is at the base of the observed electrical behaviour. Essentially, the presence of grain boundaries and defects makes the processes of rearrangement at the interfaces energetically favoured with respect other phenomena, like recrystallization. In addition, the granular and disordered structure can trigger different phenomena at the nanoscale, under the flowing of an electron current. Starting from this picture one can understand the differences among HIR and LIR samples as arising from the different degree and number of nano- and mesoscale junctions formed during the cluster deposition process. HIR samples are fabricated stopping the deposition close to the percolation thickness where the number of interconnection and junctions is relatively low. The structure is characterized by gaps acting as an effective barrier for the electron flow, thus involving non-ohmic conduction mechanism [142] and bridges, where current can reach high density levels inducing breaking/formation events. This determines the global non ohmic behaviour observed since the application of low voltages. On the other hand, LIR samples are characterized by a larger number of interconnections between grains with a higher volume density; as a consequence, the dissipated energy for volume unit and current density assume different values compared to those of HIR samples for the same applied voltage. The possibility to observe reversible switches controlled by the voltage pulse amplitude is due to the balance between connections formation and breaking taking place at the nanoscale for the different applied voltage values [114]. Higher voltages cause a higher flowing current inducing several and consecutive breaking phenomena between grains.

4.3. Temporal correlations of resistive switching activity

To gain a deeper knowledge about the switching activity and to understand the occurrence of the observed phenomena in time, we analysed the data to obtain the temporal correlations [18,46,114]. A thresholding process was applied to recognize the switching events and the distribution of the time intervals among switches was studied to reveal their degree of correlation.

Several inhomogeneous temporal phenomena, like occurrence of earthquakes and the neuron spiking activity are characterized by bursting period of high activity interspersed by periods of inactivity [46]. This reflects in a power-law distribution of the inter-event time distribution and scale free properties [46]. This kind of activity was recently recognized as a fundamental working state of

a biological neural network [42,48]. In particular, this behaviour results from the dynamic reorganization of the interconnected neurons in the network and enhances the learning performances [43,50].

This property is typically observed in systems that show emergent complexity [42,46,48] and the ability to organize into a critical state. The Self-Organized Criticality (SOC) is a general property observed in many contexts (earthquake, piling of granular media ecc…). The features of SOC are correlated temporal processes [47,48], with no characteristic scale for event size (scale-free property) and described by power law [46]. Here, the temporal correlations in the switching activity of cluster-assembled films are investigated.

4.3.1. Analysis Method

We performed a threshold analysis in order to distinguish switching events from random noise. This was obtained by computing the relative difference of consecutive resistance values in the temporal resistance series and setting a threshold to discriminate from noise. Figure 4-12 shows a pattern of the resistance evolution of a typical cluster-assembled film over the time under a voltage application of 15 V.

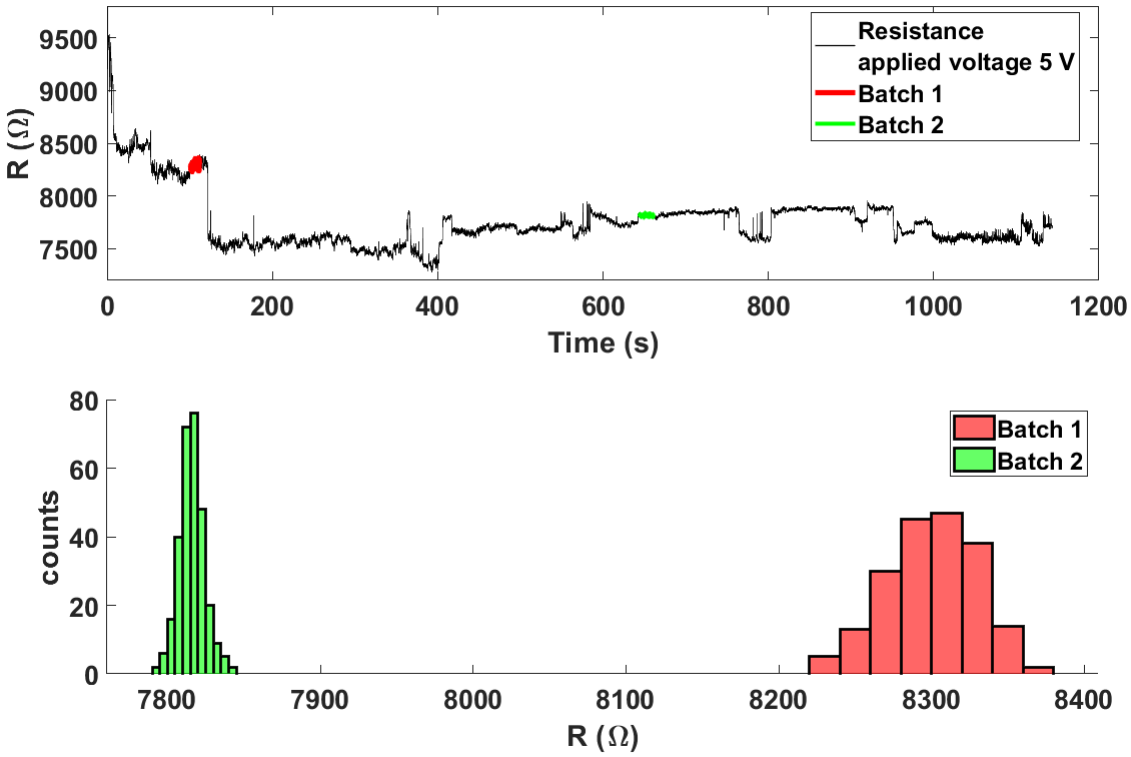

Figure 4-12 top panel reports the spontaneous activity for the electrical resistance as function of time for a cluster-assembled film under the application 5 V bias. The two selected intervals for the σ computation are shown highlighted in red and green. Bottom panel reports the distribution of the resistance values for the two

selected intervals shown with the same color code. The first interval has a distribution of the resistance values peaked around 7820 Ω, while the second one, more broadened, around 8300 Ω.

The threshold value was chosen calculating the standard deviation of an interval without switching events (the blue and red intervals in Figure 4-12, with the respective distribution on the bottom) normalized by the average of the selected values. In this way a switching event is defined as two consecutive resistance values that differ by a number greater than the computed standard deviation:

$$\frac{R_{i+1} - R_i}{R_i} > n * \sigma_{normalized} \tag{4.1}$$

with n = 4 to obtain a robust thresholding process and to avoid the recognition of spurious events. In the case of random noise, the resistance values should be normally distributed, when the difference between two values is greater than four times the standard deviation, then there is a high probability that a switch occurs.

Data analysis is performed through a software developed in MATLAB environment, which implements the method to recognize the switches, and computes the quantity of interest in (4.1) for the whole data series. To compute $\sigma_{normalized}$, it is possible to select several intervals where no presence of switches appears, like shown in Figure 4-12, and to observe the resistance value distribution for each interval.

The normalized standard deviation of the data is computed for each selected data interval and stored in memory. The intervals are selected in order to be representative of each explored resistance level, selecting different portions of data resistance values (Figure 4-12). The standard deviation in (4.1) is chosen evaluating the explored resistance levels during the thresholding process. In this way, the different amplitude of the random noise, for different resistance levels, is taken account, particularly when the switch amplitude is of different orders of magnitude. This allows to analyse large amounts of data and provide an objective method for the switch events identification preventing the presence of artefacts. After the recognition step, the series of switch events is obtained, and it can be treated like a point process in time, a collection of point related to the presence or the absence of the events.

The analysis is carried out for each resistance series measured at different voltage values (5 V, 15 V, 25 V). We evaluated the Inter-Switch-Interval (ISI) distribution by computing the temporal distance $t_{ie} = t_{i+1} - t_i$ (the inter-event time) of consecutive switches for the whole interval.

To further confirm the presence of correlations in sequences of discrete switching events, analysis such as the one proposed by Karsai et al. in [46] was performed. We counted the number of consecutive switches that falls into a bursty period if $t_{ie} < \Delta t$, where Δt is a fixed time interval,

greater than the inverse of the sampling frequency. We plotted the distribution of the number of events that belong to the same burst period both for the original and for shuffled data, that should show a non-correlated behaviour. The distributions for the two cases are compared to evaluate the differences among them in order to identify the degree of randomness in the switch occurrences. Usually an exponential decay in the distribution data tail is expected for independent and uncorrelated events; on the converse, a heavy tail (a deviation from this exponential behaviour) should indicate the presence of temporal correlations in the data [46].

4.3.2. Temporal Correlations Results

In Figure 4-13 the resistance data under the application of a constant voltage are shown both for samples near and beyond the percolation threshold.

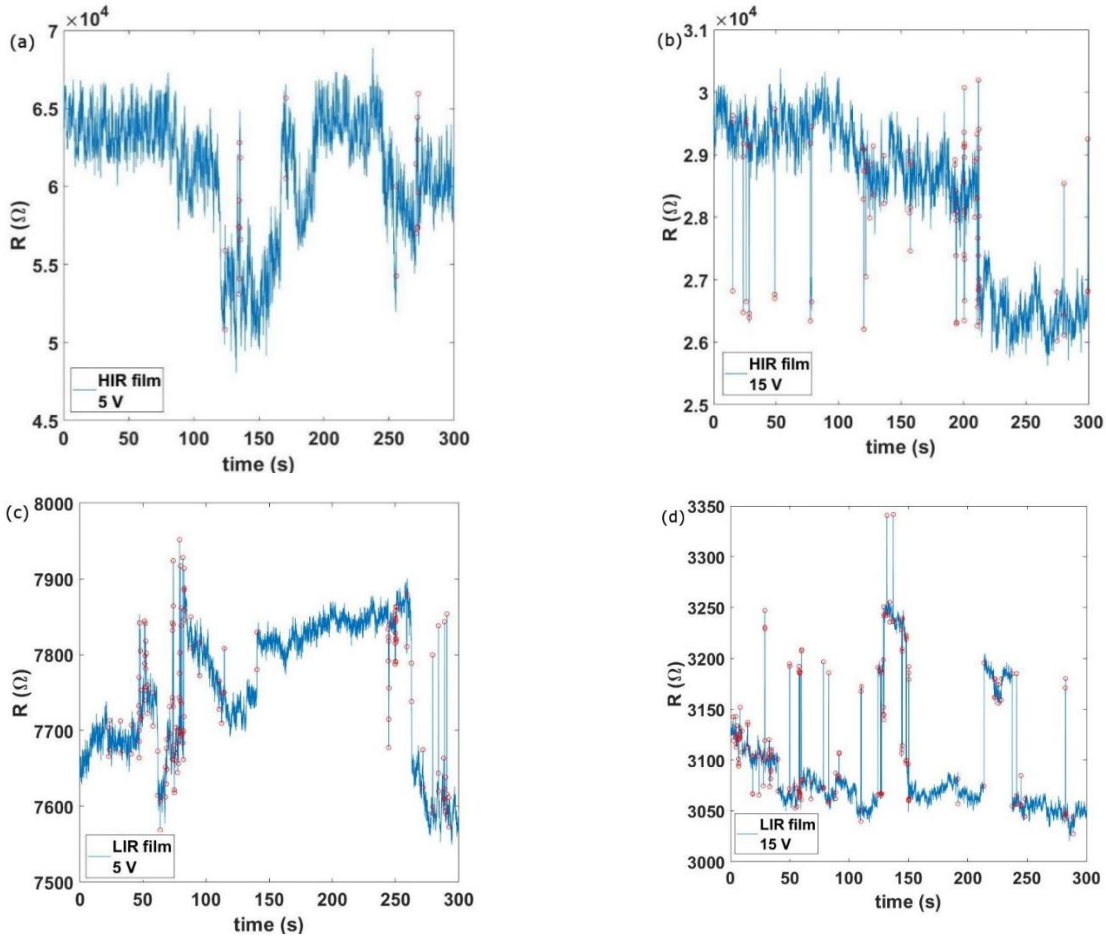

Figure 4-13 Switch activity patterns (in red the events identified as switches) for two different samples under different voltage values in a time window of 300 s. a) The switching activity for a HIR film under low applied voltage (5V) characterized by few and uniformly distributed events. b) Switching activity for the same sample under the application of higher voltage (15 V); the increasing of switching activity is clearly visible. c) Switching activity for a LIR sample under 5 V and d) under 15 V. In both cases an intense activity with burst events is visible. From [109]**.**

The samples belonging to the second class explore more stable and defined resistance levels; once a resistance level is reached, the sample continues to show the same resistance in time until a second switching event occurs. On the other hand, the samples near the percolation threshold show more frequent switching events and continuous evolution of the resistance, like the examples in Figure 4-13-a and c. The graphs become more similar under the application of higher voltages: the switching rate increases and the explored resistance states become more stable in both cases (Figure 4-13 b and d).

In order to verify the existence of a degree of correlation among the electrical spikes observed in the cluster-assembled films, the Inter-Switch-Interval (ISI) distribution was analysed. Figure 4-14 shows the ISI distributions for both LIR and HIR devices polarized at 5V. X-axis reports the ISI portioned into bin and on y-axis the normalized counts on the total number of measured ISIs. The distributions are characterized by a high number of consecutive switches with a small interval time between each other, giving rise to the higher peak in the graphs. The longer time intervals are determined by period of silence, i.e., where no switches are present; they contribute to the tail at higher time interval in the ISI distribution. The fitting procedure on the xx graph was carried out through the maximum-likelihood method [214] and comparing the confidence bounds [see *mle* function MATLAB documantion] of the estimated parameters for both.

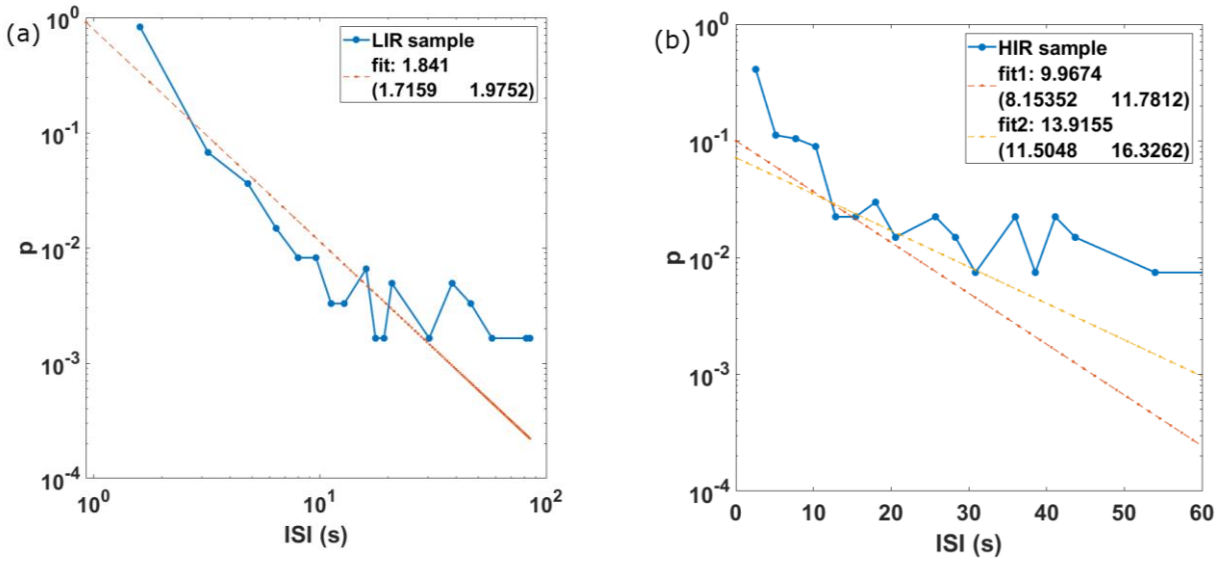

Figure 4-14 ISI distribution for measurements at 5 V. (a) Results for a LIR sample: the power law obtained by the maximum likelihood method is shown in the log-log scale graph (the estimated parameter with the confidence bounds at 95% certainty level is shown in the legend) (b) Results for a HIR sample: the bi-exponential trend that better fit the data are shown in the graph in semi-log scale (the estimated parameter for each exponential branch with the confidence bounds at 95% certainty level is shown in the legend). From [109]**.**

The maximum reached interval value can be different for each class of samples. It is usually higher for LIR samples (like the case in Figure 4-14 a), these results arise from a pattern with bunches of events (bursts) separated by longer interval of times (see Figure 4-13 c-d). For HIR samples shorter intervals are observed as shown in Figure 4-14 b, resulting from a pattern of switches more uniformly distributed than the first one (like that shown on Figure 4-13 a-b). In both cases the distribution trend was investigated fitting exponential and power laws. In the majority of the cases, we verified a power law trend (Figure 4-14 a) and sometimes (for HIR samples at low applied voltage) a bi-exponential trend better fit the data (we report an example in Figure 4-14 b). These differences arise from the different morphologic properties and the value of the delivered power. I highlight that points with 0 value on y-axis are not visible in the log-scale graph, they are the main source of error observed among the fitted and the experimental curve. As discussed previously, local configurations of interconnected grains can undergo different phenomena for different degree of connections and density of junctions; this determines temporal distribution of switching events. The presence of longer silence period for the LIR (Figure 4-13 c-d) and at higher voltages imprints a heavier tail to the ISI distribution.

This wide range of explored intervals can originate from the variety of structural defects and the consequent energy and time scale involved in their evolution. As an example, consider the vacancy diffusion mechanism that could be responsible for the resistance fluctuation, being capable to cover a wide range of relaxation-time interval, from $10^{-11}s$ to $10^{7}s$.

To confirm this behavior, the ISI distribution obtained in different conditions were compared and the results shown in Figure 4-15 (a), that shows the ISI distribution and the fit results for two set of data obtained with two different thresholds (n=4 and n=6 in equation 4.1).

The results clearly show that there is not a strong influence on the choice of the threshold in the explored range. The ISI distribution for different samples (both LIR and HIR ones) in Figure 4-15 (b) and under different applied voltage (Figure 4-15 c) confirmed the previous observations: LIR samples present a higher number of events at higher ISI (see the tail in Figure 4-15 b), while higher voltages can trigger an higher number of bursted events, increasing the burst activity in both classes of samples (compare the trend of the curves in Figure 4-15c). In LIR devices longer ISI were observed, as shown in Figure 4-14 (a), because of the presence of a larger number of junctions and connections that require a higher amount of flowing current to activate bursts of switches. This makes the events more grouped, with a lower probability (longer intervals between events) but with a high number of events after the activation (avalanche process), indicating a correlation between the switching events, as further suggested by the pronounced tail of the ISI graph in log scale.

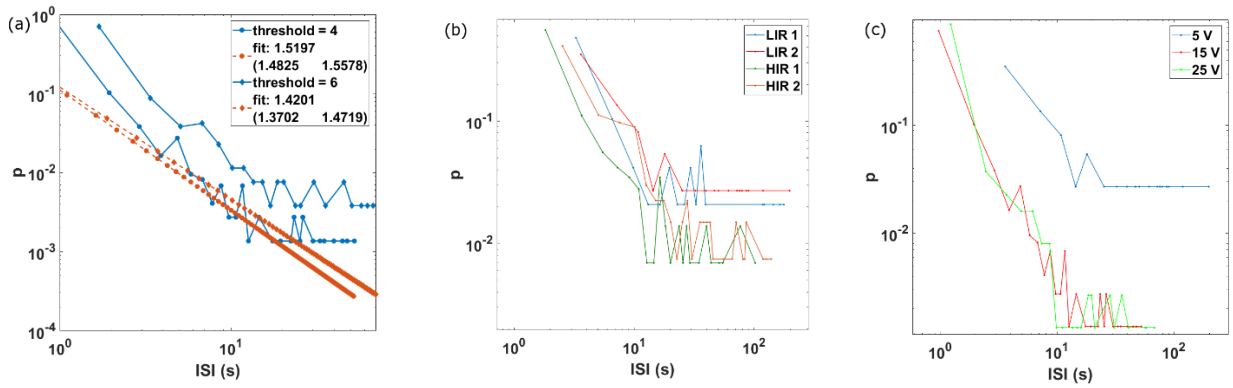

Figure 4-15 (a) ISI distribution for the same sample under the same applied voltage at different thresholds. The distribution and the resulting fit are not substantially affected by the chosen threshold. (b) ISI distribution for different samples (LIR samples blue and red curves, HIR samples green and yellow curve) obtained under the same applied voltage (5 V). (c) Typical ISI distributions for one sample obtained under different applied voltage (5 V, 15 V, 25 V). This shows as the applied voltage can determine the inter-switch interval distribution. From [109]**.**

In order to corroborate this observation, the burst analysis was performed comparing shuffled and original data (as described in detail in [46]). The distribution of the number of events that belong to the same burst period (selected choosing one interval time cut-off) both for the original and for shuffled data, that should show a non-correlated behaviour, was investigated.

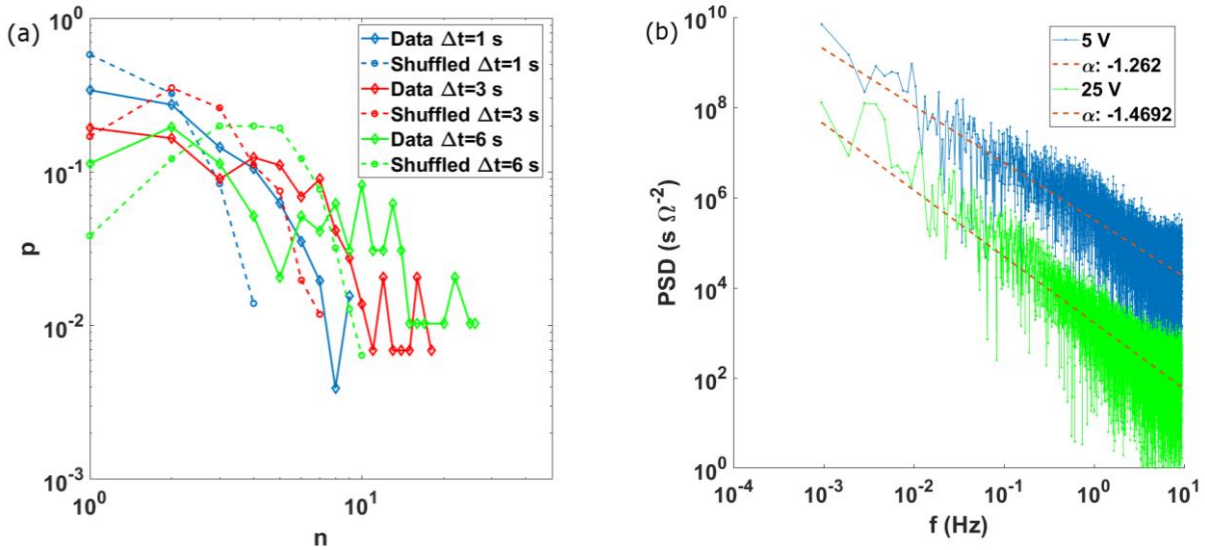

Figure 4-16 (a) The number of consecutive event distribution for different time windows *Δ*t (1 s, 3s and 6s) in log scale. Each curve of the number of consecutive events distribution (continuous line) is compared with the distribution obtained after the shuffling process (dotted line) (b) The power spectral density of the resistance data series of a cluster-assembled film in log scale for the same sample under two different applied voltage (5 V and 25 V). From [109]**.**

The results are shown in Figure 4-16, where the distribution of the bursty period (defined as the sequence of the number *n* of events where each one follows the other in a time window Δt) is plotted for different Δt values.

The dotted curves (shuffled data) decrease faster than the continuous ones (original data). This is due to the presence of longer ISI in the data that are washed away after the shuffling process. In samples with a more uniform switching pattern (like in HIR samples at low applied voltage) the two curves are more similar (data not shown). A pure exponential behavior (that should be an hint of independent and random events [46]) has never been observed for the original data; the graphs show no exponential trend for the data and the curve shows an heavy tail unlike the shuffled data one. A similar trend is encountered studying the electrical activity of neurons [42,46,49]. To exclude the influence of the selected time window to perform the analysis, we compared different curves in the same graph (Figure 4-16): they all show the same trend; the slight difference in the green curve can arise from the higher time window so that uncorrelated periods are merged together.

The trend of the power spectral density (PSD) of the overall data noise, was also reported in Figure 4-16 (b). The fluctuations in measured electrical quantities can give important information about the phenomena involved in the flowing of charges and their interaction with the particles that compose the studied system [142]; the PSD can give a deeper insight into their time correlation [17,215,216]. The measured resistance of cluster-assembled films shows a $1/f^{\alpha}$ scaling behavior in the range of analyzed frequencies (Figure 4-16), with $1 < \alpha < 1.5$. No significant differences were observed among LIR and HIR devices. We observed a dependence of the exponent α from the applied voltage, resulting in lower absolute value at lower voltage in most of the cases, as shown in Figure 4-16 b.

A similar network activity dynamics is described by the Self-Organized Criticality model [47,48]. SOC models display long-range correlations and very different systems such as *in vitro* neuronal cultures [48], acute cortical rat slices [42], and granular systems [45]. The SOC paradigm is then an interesting descriptive model for spontaneous bursts but does not offer insights into their biological origin and their functional role.

In this chapter, the results about the conduction electrical properties of cluster-assembled gold films were presented. Attention was devoted to study and discuss the activity of resistive switching resulting under the application of an external voltage bias. In particular, the effect of voltage pulses was taken into consideration, showing the possibility to exert a certain control on the random occurrence of switching events. In addition, the emerging activity form samples with different initial resistance was explored, showing different statistical properties in the resistance time series. Result suggests the appearance of a correlated behavior in the overall electrical activity stimulated by the

application of voltage bias. The features presented by cluster-assembled gold films demonstrate great importance for technological application. The switching activity and its dependence form both the external stimuli and the fabrication process provide the possibility of considering this class of device as source of a computation medium that merge a certain degree of stochasticity with a metastable response to an external electrical stimulus [3,4,16].

5. Non-local Spatial Correlation

Cluster-assembled gold films have a granular structure, rich of defects, grain boundaries and dislocations [121]. This is at the base of the deviation form Ohm's law and of the non-linear electronic conduction described in the previous chapters. Since the resistive switching activity originates from non-local phenomena and it is intrinsically linked to the structural properties at the nanoscale, this can vary on different zones of the film. The aim of this chapter is to gain a deeper insight into the non-local correlations of conduction properties of cluster-assembled films and how this influences the overall behaviour. To address this aspect, devices equipped with several electrodes are fabricated, to characterize of the electrical resistance of different regions of the film (Figure 5-1) and the spatial correlations.

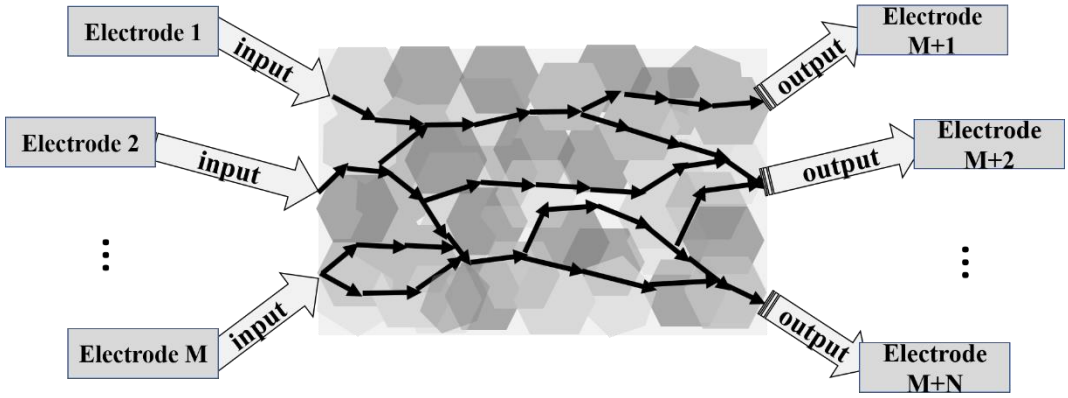

Figure 5-1 Schematic representation of a multi-electrode device. The area of deposition, shown in the middle of the figure, is connected to several electrodes. On the left, the electrodes used as inputs are shown. On the right, the electrodes used as outputs, collect the flowing current. The black arrows show the current paths of minimum resistance. Selecting one couple of electrodes, it is possible to select the current paths related to different region of the cluster-assembled film.

Using different configurations of input-output electrodes, it is possible to evaluate:

- The electrical properties of different zones of the same film
- How different zones influences each other under the application of an external bias (non-locality).
- How macroscopic geometrical factors of the fabricated samples influence the local and the overall switching behaviour.

Samples with different geometries were fabricated: in Figure 5-2 two different electrode configurations are shown.

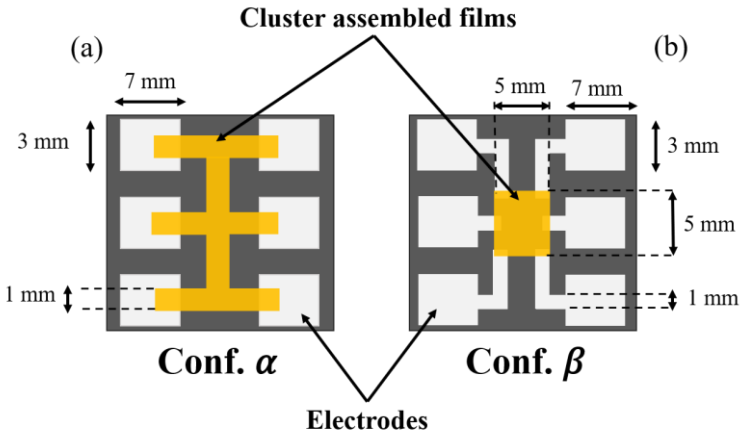

Figure 5-2 Scheme of two different device configurations, Conf. α consisting of one vertical cluster-assembled film stripe connected to 6 electrodes through three horizontal cluster-assembled film stripes and Conf. β consisting of a uniform square shape cluster-assembled film connected to six electrodes. a) Dimensions of Conf. α device (cluster -assembled film represented by the colored regions). b) Dimensions of Conf. β device (cluster-assembled film represented by the colored region).

Configuration α (Conf. α) consists of six electrodes connected by a cluster-assembled film shaped as one vertical stripe and three horizontal one as shown in Figure 5-2 (a). Configuration β (Conf. β) consist of a square cluster-assembled film (5 mm x 5 mm) connected by 6 electrodes (Figure 5-2 (b)). Conf. α and Conf. β devices are used to study how the electrode spacing connected to the cluster-assembled films and their configurations influence the resistive switching activity of the film and the correlations among the regions connected to different electrode couples. The samples under examination have a thickness of about 20 nm and belong to HIR class. I highlight that, since the cluster-assembled films deposited to fabricate multi-electrode devices have a larger surface with respect to two-terminal devices, samples with greater thickness values were not taken under consideration to avoid too low initial resistance values.

5.1. Resistive switching activity in multi-electrode cluster films

To evaluate non-local conduction properties of regions of cluster-assembled films, current-voltage characteristics are measured for different electrode couples. The curves are measured applying a voltage ramp in the range 1 V-20 V and measuring the current flowing between the selected electrodes at each ramp point. The voltage difference between two consecutive ramp points is 1 V and each point is applied for 100 ms. The voltage is ramped up and decreased, repeating the process 10 times.

The current-voltage curve obtained for 3 different electrode couples of a device with Conf. α are reported in Figure 5-3.

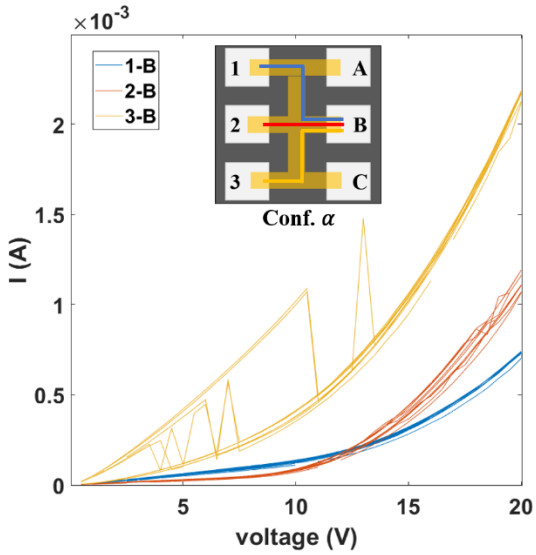

Figure 5-3 The current voltage curves of a multi-electrode device on different electrode couples in the range 1 to 20 V obtained applying voltage ramp with an increasing branch and a decreasing one. The inset shows the Conf. α device and the electrode configurations related to the measured I-V curves. The curves are non-linear and switching events are present, giving place to the hysteretic trend particularly evident in the yellow curve.

The main features reported in the previous chapter are present also for multi-electrodes devices. The I-V curves reported in Figure 5-3 in the range 1 to 20 V are non-linear and the slope strongly increases for voltage greater than 10 V. For each electrode couple different curves are reported, obtained applying different voltage ramps. The resistance can undergo discrete and reversible jumps that translates into a hysteretic behaviour, particularly evident in the yellow curve reported in Figure 5-3. The different slopes of the curve shown in Figure 5-3 are due to the different average resistance values assumed by the three different paths followed by the current for the three couples of electrodes. These results are valid also for conf. β devices.

Since these results shows the presence of resistive switching triggered by the repeated application of external voltage bias, to evaluate non-localities in electrical activity of each film region and how this is influenced by the application of an external electrical stimuli, an over-threshold signal is employed to trigger the switching activity. The threshold is selected by measuring the resistance of the film for each electrode couple in the two-probe configuration and increasing the voltage until the switching activity appears. It is usually larger than 5 V for the multi-electrode devices. A subthreshold signal, 1 V pulse train, is employed to check the resistance evolution. The sub-threshold train is composed by 25 pulses with width 50 ms. The scheme of the measurement protocol is shown in Figure 5-4.

The protocol employed for the film characterization, for each measurement step, consists of: the application of the over-threshold voltage on one set of electrodes and the subsequent application the

under-threshold voltage on all the electrode couples consisting in one left electrode (identified by a number in Figure 5-4) and one right electrode (identified by a capital letter in Figure 5-4), for example 1-A, 1-B…, to obtain the resistance values and evaluate their evolution. The possibility of choosing different electrode couples enables to check the correlation among the switching activity of different zones (Figure 5-4).

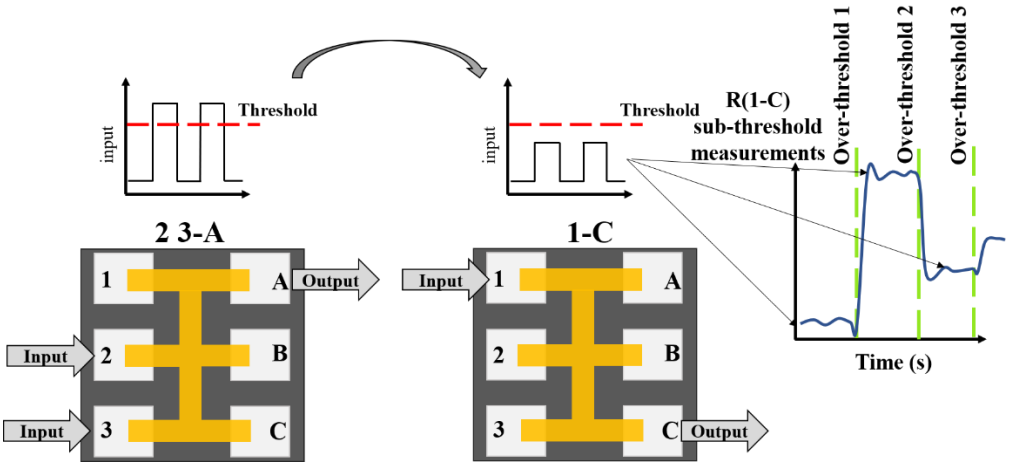

Figure 5-4: Schematic representation of the measurement protocol on multi-electrode devices. On the left, the electrodes 2,3 used as inputs and the electrode A employed as outputs, are selected for the application of an over-threshold signal. On the right, one example of sub-threshold measurement on the electrode 1 and C, whose aim is to check the effect of the application of the over-threshold signal. The inset shows a schematic graph of repeated measurement performed on one electrode couple (1-C) to check the resistance evolution after different over-threefold signals application.

Each over-threshold pulse lays in the voltage range (-15 V 35 V). Different electrode couple configurations are selected, and the resistance levels explored by each electrode couple are measured through sub-threshold voltages to check the non-localities arisen in the electrical switching activity triggered by over-threshold signal and the correlations between different regions.

The resistances of four different electrode couples, measured after each application of the over-threshold signal to one input electrode configuration (1-C), are shown in Figure 5-5. Green dashed line points out the over-threshold voltage application, and the resistance measured between the electrodes is shown before and after the application.

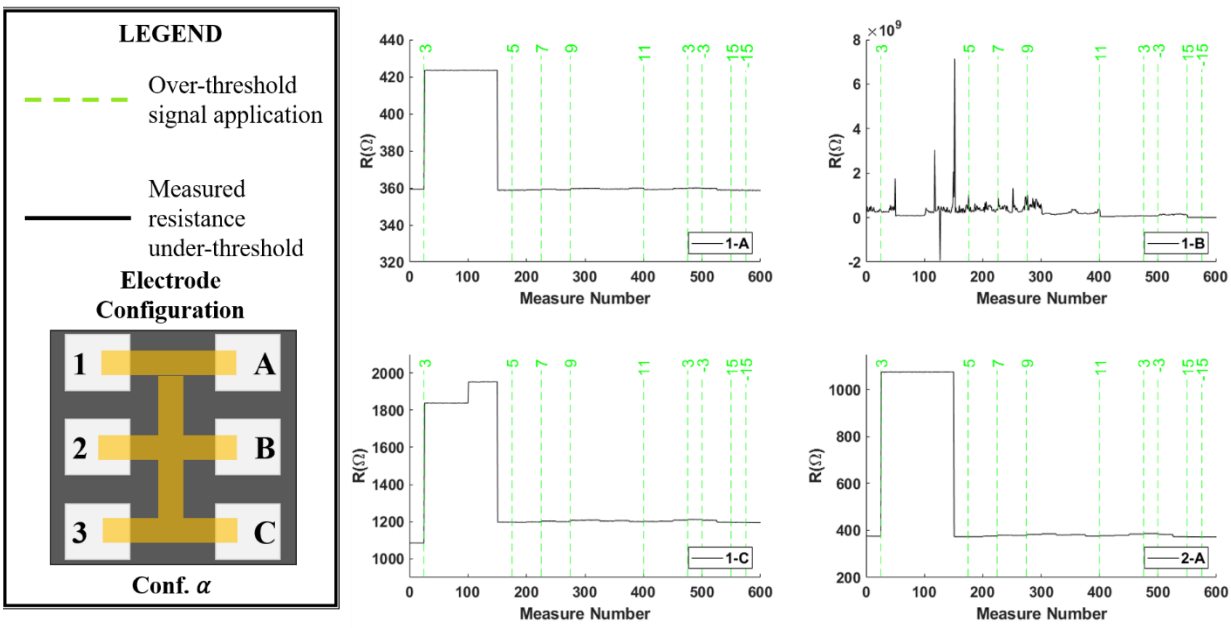

Figure 5-5: Electrical resistance evolution for a Conf. α device, for four different electrode couples after the application of several over-threshold signals to the electrode 1-C. The dashed green lines indicate for the over-threshold voltage application, to the electrodes 1-C, whose value is indicated at the top of each line. Green lines aim to aid the comparing the resistance levels explored before and after each voltage application on one electrode couple.

In Figure 5-5, the main aspects of the electrical activity of Conf. α are present. The application of over-threshold signal can determine a correlated resistive switching behaviour, evident in the resistance pattern measured at different electrode couples 1-A, 1-C, 2-A. Note that the electrode configurations having in common at least one electrode with the couple under which the over-threshold signal is applied, strongly react and switching events can be activated (see electrode couples 1-A and 1-C in Figure 5-5). On the other hand, also non-localities in the resistive switching activity triggered by the application of the over-threshold signal can occur, as shown for example by the electrode couple 2-A in Figure 5-6: in this case the resistance shows the occurrence of resistive switching even if the region of the cluster assembled film is not directly connected to the electrode couple to which the over-threshold signal is applied. This is due to resistive switching events that can occur in different points of the region of the cluster-assembled film interested by the passage of current during the over-threshold signal application, determining non-local effects.

Noteworthy, the resistances referred to electrode B have a higher value than the other ones. The origin is ascribed to the occurrence of breakdown phenomena near the electrode B, after the application of over-threshold signals, that affect the current flowing through that electrode. This means that the current flowing toward electrode B experience the highest resistance paths.

Some of the over-threshold signal can result also in the absence of switching activity for the electrical activity of the electrode couples shown in Figure 5-5. However, this is due only to the

history of the over-threshold signal applied to one electrode couple. The resistive switching activity can be triggered again changing input electrode configuration.

As a result, the control of the resistance switching activity by the application of over-threshold signals at different electrode configurations determines non-local electrical activity of the film where different regions can react differently to the application of the same signal on the same electrodes. This is reflected by the presence of correlations in the resistance pattern measured at each electrode couple and the occurring of non-local resistive switching event after the application of over threshold signals.

In order to gain a deeper view into the resistive switching activity of a multi-electrode cluster assembled film, the histogram of the explored resistance levels measured at two electrode couples of a Conf. α are reported in Figure 5-6.

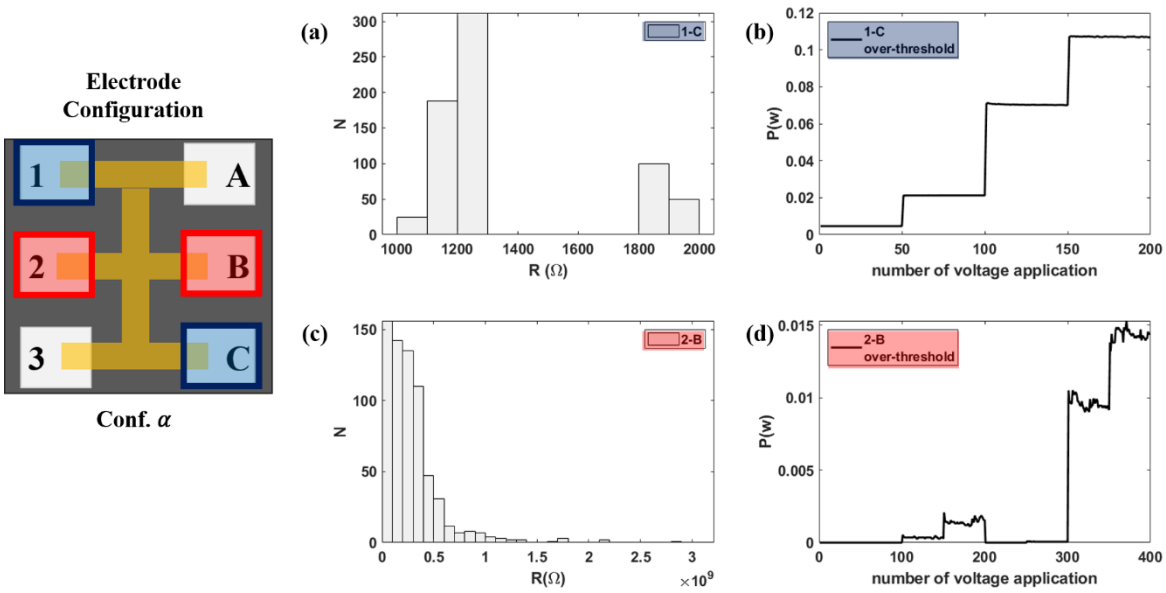

Figure 5-6 On the left, the Conf. α device scheme showing the electrode configuration for the measurement. On the right, the histogram for the resistance values and the dissipated power over time for two electrode couple. (a) Histogram of explored resistance values on the electrodes 1-C for a whole set of measure under sub-threshold voltage. (b) Dissipated power computed as the product between voltage and current on the same electrodes for the over-threshold voltage application. (c) Histogram of explored resistance values on the electrodes 2-B for a whole set of measure under sub-threshold voltage. (d) Dissipated power computed as the product between voltage and current on the same electrodes for the over-threshold voltage application.

The histograms shown in panel a and c report the number of explored levels of two different electrode couples measured after several over-threshold signal applications (more than 20 different over-threshold processes applied to different electrode configurations). The different peaks in the histograms referred to different resistance states recurrently explored by one single electrode-couple.

In addition, different trend for the two histograms is due to the different effects on each film regions of the over-threshold signal application.

For the sake of completeness, the dissipated power by the over-threshold signal is reported in panels (b) and (d) of Figure 5-6. This gives a useful information in term of power needed to trigger the resistive switching activity in multi-electrode device. The difference between values of dissipated power at different electrode couples is clearly visible. Note that a maximum of 100 mW is dissipated for the electrode 1-C, to a minimum of few μW for the electrode 1-B This is a consequence of the different resistances characterizing different cluster-assembled film regions. Note that the presence of well different resistance values for different electrode couples, and hence of dissipated power by a flowing current, open to possibilities of choosing the electrode configuration that is more power efficient to control the resistance switching activity of the device.

These results suggest that the electrical activity observed for different electrode couples arise from atomic reorganization that takes place at the nanoscale after the application of an over-threshold signal [121]. The current flowing under the application an over-threshold voltage bias dissipates a critical amount of energy triggering the occurrence electromigration and atomic rearrangement phenomena [110]. These processes are favoured by the presence of defects, dislocation and high density of grain boundaries that characterize the structural properties of cluster-assembled film at the nanoscale [109,121,150]. In Figure 5-7 a schematic representation of the effect of an over-threshold voltage is shown.

The local alteration of the structure at the nanoscale determines a change of the conduction properties in different regions with a consequent reorganization of the currents flowing in the film through the paths of minimum resistance. This explains the different electrical activities observed for different electrode couples: the sub-threshold measurements performed on electrodes collecting currents flowing though unaltered paths are not characterized by resistive switching activity. On the contrary, electrode couples collecting the current flowing through regions affected by the over-threshold voltage bias result in resistive switching phenomena (see Figure 5-7).

The effects of different electrode configurations used for the application of over-threshold signal can be explained considering the organization of the current paths at the nanoscale. The current flowing through different electrode couples, flow though different regions of the film. This in turn causes the occurrence of rearrangement effect in different zones (see blue and read shaded region in Figure 5-7).

The result of this complex behaviour, the organization of the paths of minimum resistance at the nanoscale after the application of the over-threshold signal, can affect the conduction properties of

several couples od electrodes. This gives rise to the non-local effects and the correlations observed in the measured resistance values for different electrode couples.

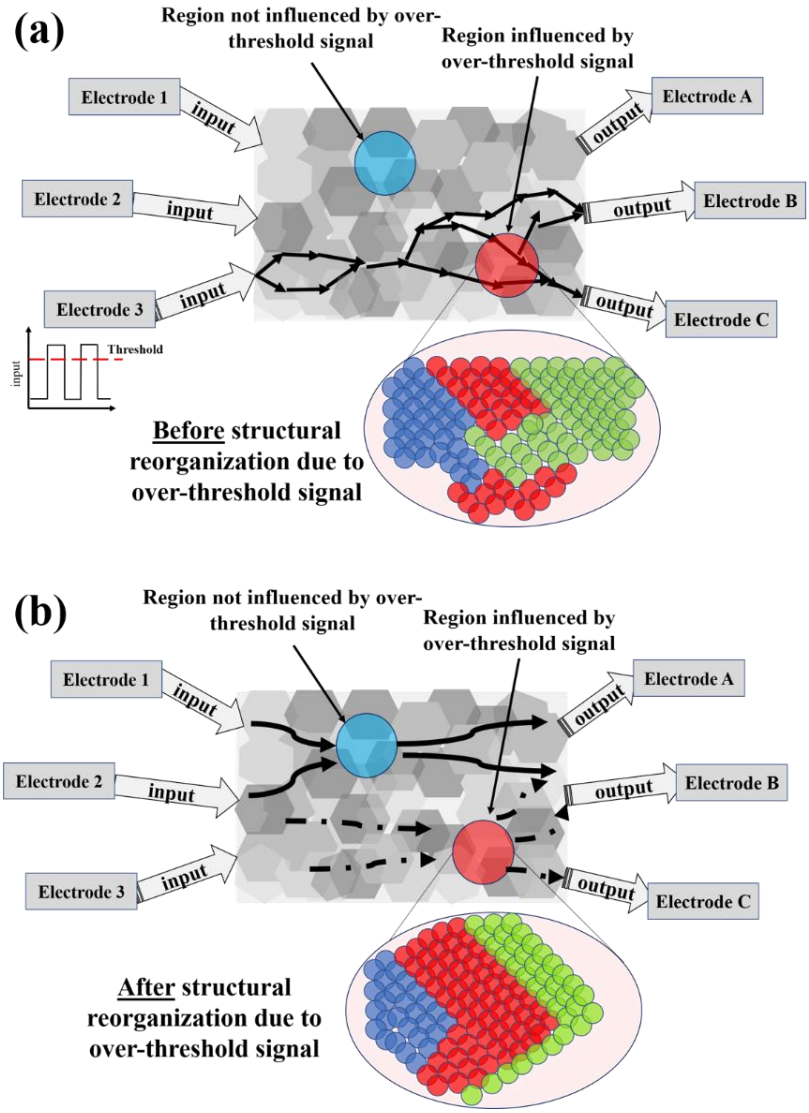

Figure 5-7 Schematic representation of the effect of over-threshold voltage application on different regions of a cluster assembled film. (a) Over-threshold voltage application between electrodes 1 – B, C. Blue shaded region is that one not affected by the over-threshold signal. Red shaded region is that one influenced by the over-threshold applied voltage. The insight shows the atomic organization at the nanoscale before the reorganization takes place. Different colors stand for the presence of grain boundaries. (b) Schematic representation of the effect of the over threshold voltage on different film regions. The solid line arrows show unaltered current paths, while dashed line arrow show current paths affected by the over threshold signals. The insight shows the atomic rearrangement that cause the alteration of the electrical resistance.

To study how the electrode spacing can influence the electrical activity of the cluster assembled films and the degree of correlation between different regions, the measurements have been performed on Conf. β devices. The protocol and the characteristics of the voltage pulse trains are as the same as for Conf. α devices.

The resistance measured for four different electrode couples of a Conf. β device after the repeated application of over-threshold signals is shown in Figure 5-8. In this case, the correlations among the activity of different electrode couples become very strong. All the measured resistance patterns show the same trend, also those relative to electrode couples that does not share electrodes with the configuration used for the over-threshold application.

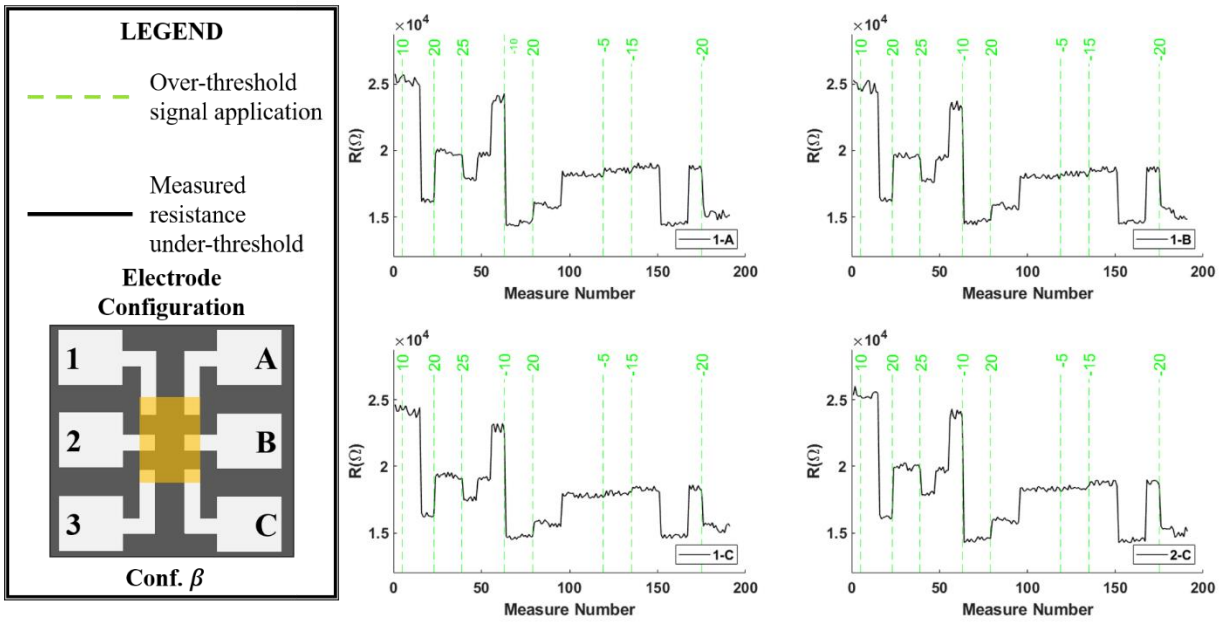

Figure 5-8: The electrical resistance evolution for a Conf. *β* device, for four different electrode couples after the application of several over-threshold signals to electrode 3-C. The dashed green lines indicate for the over-threshold voltage application, to the electrodes 3-C, whose value is indicated at the top of each line. The lines aim to aid the comparing the resistance levels explored before and after each voltage application on one electrode couple.

In the case of Conf. β devices the lower electrode spacing with respect to Conf. α devices, causes higher current densities flowing through the film for any electrode configuration. As consequence, all the electrode couples are affected by the over-threshold signal applied to any of the regions of the cluster films.

To quantify the correlations among different regions of cluster-assembled films, for both device configurations, the Pearson coefficient [217], value between -1 and 1, among the series of data obtained cumulating all the measurements for the electrode couples after the application of the over-threshold signals was computed. The correlation matrix is obtained taking the absolute value of coefficient computed for all the electrode couples. In Figure 5-9 the results are shown.

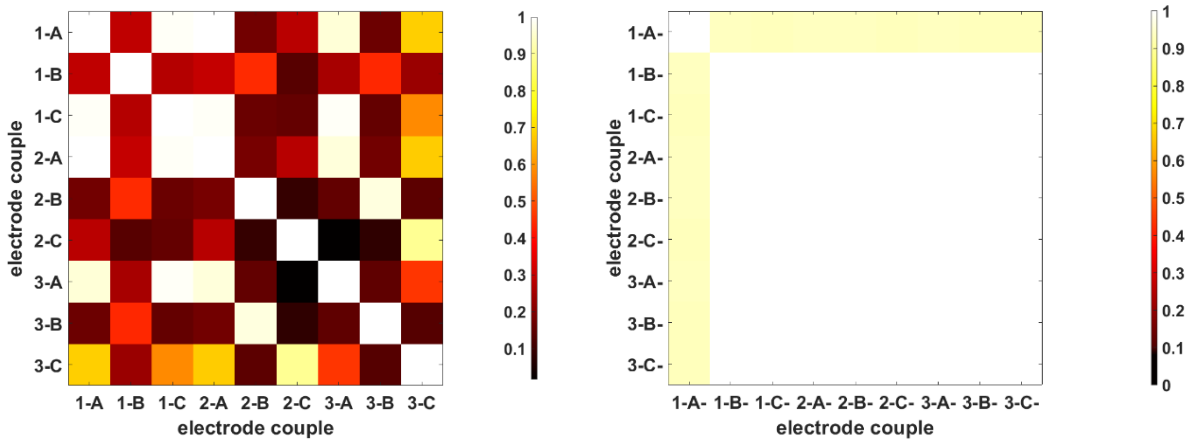

Figure 5-9 The matrix correlation among the resistance series data cumulated after each over-threshold voltage application for a Conf. α (a) and one Conf. β (b). Each element of the matrix states for the absolute value of the coefficient correlation between to different couple. The color scale states for the magnitude of the computed coefficient.

The matrices are symmetrical and the diagonal elements are equal to 1. Each coloured square displays the resulting value of the correlation coefficient among the resistance data of two couple of electrodes (see the colour map in the figure). The electrode labels are shown near each row and column of the matrix. It is possible to observe that, for Conf. α devices, there are both high and low degree of correlation among the different electrode couples. For example, Figure 5-9 shows that for electrode couples 1-C and 1-A there is a correlation different from the electrode couples 1-B and 1-A. On the contrary, the second matrix shows that the correlation coefficients are generally higher for a Conf. β device. However, some facts should be highlighted: 1) Pearson coefficient reveals only a general linear dependence among two data series 2) the data series for multi-electrode films are represented by the measurements carried out to control the resistance evolution after the application of over-threshold signals. This means that the degree of correlation is determined by the choice of electrode configuration and characteristics of the over-threshold voltage signals.

These results show a complex spatiotemporal organization of the currents following at the nanoscale afterwards the application of external electrical stimuli. As result, effects of non-locality in the over-threshold stimulus and correlations among electrical activity of different regions of the cluster-assembled film, emerge from this complex behaviour.

Some similarities can be identified between the non-local behaviour of cluster-assembled films and biological neural networ. As briefly mentioned in Chapter 2, the human brain essentially consists of a network of neurons, characterized by a high number of parallel and reciprocal connection [40,51,53]. This determine a complex spatiotemporal organization of the electrical activity of the single neurons and whole brain regions in response to an external stimulus [40,53]. This cooperating behaviour characterized by a both segregation and integration among the electrical activity of

different areas could be responsible for the efficiency in solving tasks [40,51,53]. Thanks to advent of fMRI and PET and the high resolution in collecting the spiking activity of different brain regions by microelectrode arrays [40,51], it was recently possible to analyse how different elemental units specialize and cooperate together [40,51]. Information theory represent the natural environment to study the organization in term of correlation for a system composed by a huge number of small units that behave like a realization of an experiment of random variables [51,218] and it was applied to study biological neural networks [40,51].

For all these reasons, it is in my opinion interesting to use the same theoretical tools to study and analyse the electrical activity of cluster assembled films. In the following, the theoretical background and the notation developed for neurobiology is briefly presented [51,218].

5.2. Information theory

Information theory [219,220] is a powerful tool to study the correlation of a system composed by several smaller units, each with an individual activity [219,220] and act like several realization of a Random Variable (RV). To introduce the matter, I briefly recall the definition of *entropy* and then Mutual Information and Integration are introduced.

The *entropy* can be defined, for a system at the equilibrium that can be found in several states each with probability p_i as:

$$H = \sum p_i \log (p_i) \qquad (5.1)$$

The concept of entropy is useful for the description of systems that can be found in several states there is a certain degree of uncertainty to describe it. Entropy gives a measure of disorder of the system. At the opposite, information is a measure of the order of a set of data. To clarify this, let us consider the set of 4 letters {‘g’, ’n’, ’o’, ’s’}. The set can be found in several states with different letter ordering, each with a certain probability. In general, a casual disposition means lack of order. Only few of these states carry some useful information, for example if the letters present in the form ‘s o n g’, in this case it means there is a high degree of order. For the specific example, the probability of finding the correct letter in the correct position is 1, this means minimum entropy.

The concept of entropy can be generalized to the temporal series of data for a stationary system, where the statistical properties do not change in time; in this case, different states can be assumed by the system, with the same probability distribution over time [221].

Entropy is a quantity defined on a single set of data and tells us how much disordered the set is when we want to predict in which state it is. *Mutual information (MI)* and *integration (I)* are

quantities defined on joint ensembles [51,218]. They are a measure of a statistical dependence between the elements of two ensembles [51,218]. In the following the notation to define MI and I is the same used in [51,218].

Consider an ensemble X formed by N RVs x_i, as schematically depicted in Figure 5-10; being X_j^k a subset of the ensemble X composed by k components on the total of N, Mutual information MI is defined as:

$$MI\left(X_j^k, X - X_j^k\right) = H\left(X_j^k\right) + H\left(X - X_j^k\right) - H(X) \qquad (5.2)$$

Note that $MI\left(X_j^k, X - X_j^k\right) = 0$ if X_j^k and $X - X_j^k$ are composed by RVs statistically independent, $MI\left(X_j^k, X - X_j^k\right) > 0$ otherwise. Note that there are $\frac{N!}{k!(N-k)!}$ combinations of subset X_j^k of dimension k on the total number of component N. MI is averaged on the total number of combinations.

Another quantity, Integration I can be introduced to study the degree of dependence among RVs, as suggested in [218]. Integration is defined as the different between the sum of the entropy of single components (that are RVs) in the set X_j^k and the entropy of the whole subset:

$$I\left(X_j^k\right) = \sum_i H(x_i) - H(X_j^k) \qquad (5.3)$$

Also in this case, $I(X_j^k)$ is averaged on the total number of combinations to form the subset X_j^k. $I\left(X_j^k\right)$ monotonically increases with k and it is equal to 0 if RVs are statistically independent and it is positive in the case of correlations.

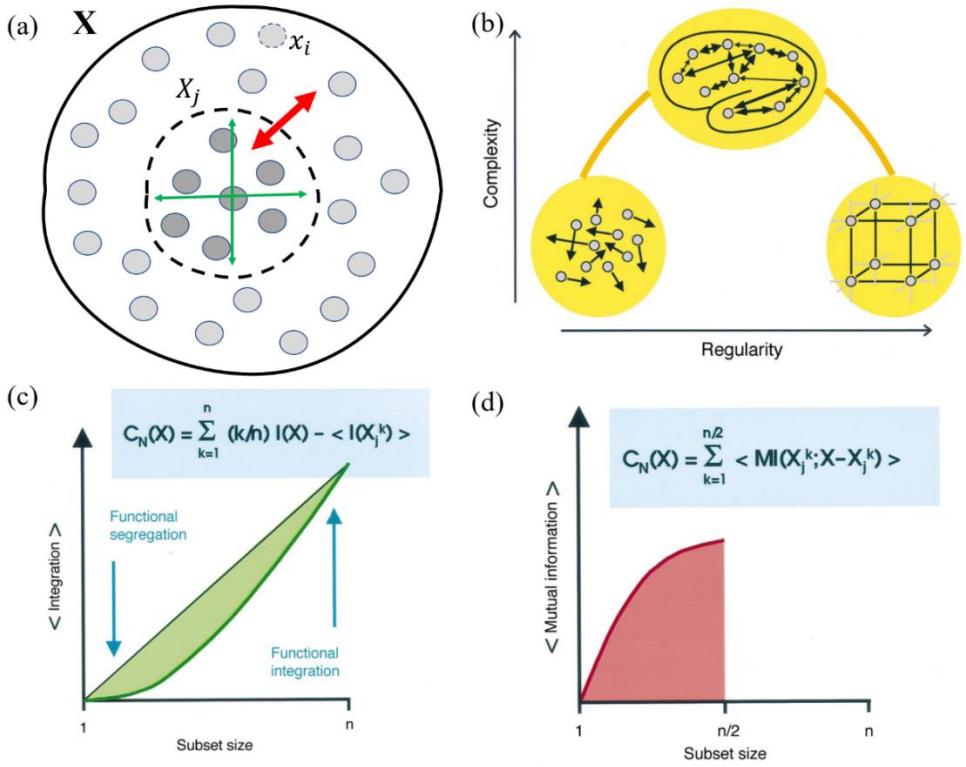

Figure 5-10 (a) Scheme of a set X composed by units x_i that represent Random Variables (RVs). The subset X_j is shown. The red arrow indicates the information exchange through X_j and the complementary set. The green arrow indicates the integration capability of the units in the subset X_j. (b) An example of different systems that present different degree of complexity as function of their regularity: gas of molecule (high disorder, low complexity), crystal bulk (low disorder, low complexity) and network with partial disorder and partial organization (high complexity). (c-d) The schematic graph of the Integration (c) and the Mutual Information (d) for a set shown in panel a. The integration has an increasing trend with the subset size of the system, and the trend deviates from the linear one for a system that has high complexity. The complexity formula derived for the integration expression (blue box), is equal to compute the shaded green area. Mutual information is shown as function of the subset size. The complexity formula derived for the Mutual Information expression (blue box), is equal to the shaded red area. Adapted from [51].

MI is a measure of the statistical dependence between the subset X_j^k and the complementary $X - X_j^k$, it gives the amount of information on the subset X_j^k, knowing the state of the rest of the system. While the correlation coefficient among two data set is measure of the amount of linear correlation in data, *MI* is a general measure of the statistical dependence, and an inference on the probability distribution of data is needed (see the entropy definition in (5.1)). *I* is, on the other hand, proposed to give a measure of the segregation (independence) and integration (dependence) among the elementary constituents of the ensemble [51,218]. Figure 5-10 shows schematic graphs for integration and mutual information as function of the subset sizes.

These quantities are useful to give a definition of complexity that takes into account the amount of information integrated by a system composed by several elemental units. High degree of information means statistical independence [218–220]. As an example, let us consider two subsets of letters taken from the alphabet: if we can choose independently the letters from the two subsets, we

can build a higher number of words). On the other hand, integration means statistical dependence. A system that presents a high degree of complexity, should show specialization (low integration) when the single constituents are considered alone, while it should integrate the elaborated information when considered as a whole (high integration). As a result, the trend of the Integration as a function of the subset dimensions deviates from the linear one. It is possible to define the complexity as a measure of the amount of integrated information within the system [51,218,222]. In the blue box in Figure 5-10 (c) a mathematical expression is shown. It corresponds to the shaded area in the figure. An equivalent definition of complexity can be given through the mutual information, as shown in Figure 5-10 (d).

The definition of complexity given above is a statistical measure of the regularities that rise from the fundamental units that compose a system, based on their statistical independence. It distinguishes the high information content patterns from noise [219] and quantifies the ability of the system to process information [51,83,218,219]. It captures the idea that a complex system is neither random neither completely ordered. A disordered sequence of letters does not bring much more information than a periodically disposition of some letters. On the other hand, the sequence of letters employed to write a book brings a high level of information. Similarly, the capacity of processing information for a physical system can be considered. It should not be expected computational abilities neither from completely disordered arranged molecules (a gas) nor a completely ordered one (the bulk matter). The brain, that presents a complex organization of the neuron networks (see scheme in Figure 5-10) demonstrates a high capability of manipulating information and so a high degree of complexity [51].

5.3. Multi-electrode configuration and the information processing

The emerging correlations among the electrical behaviour of different regions in nanostructured gold films are analysed to highlight the degree of complexity of the device through Information Theory. The aim is to clarify the statistical properties of the measured resistance patterns after the application of the over-threshold data.

A single electrode couple is considered as the fundamental unit of our system. This is the smallest part from which an electrical signal can be applied/extracted, although a complex percolating structure at the nanoscale connects the different electrodes. I assume that the statistical properties of the electrical activity do not change, and that the systems reached stationarity. This is reasonable since the statistical properties of the switching activity observed in two terminal devices do not change over time [109].

$$X_1^2 = \{R_{el1A}, R_{el1B}\}$$

$$X - X_1^2 = \{R_{el1C}, R_{el2A}, R_{el2B}, R_{el2C}, R_{el3A}, R_{el3C}, R_{el3C}\}$$

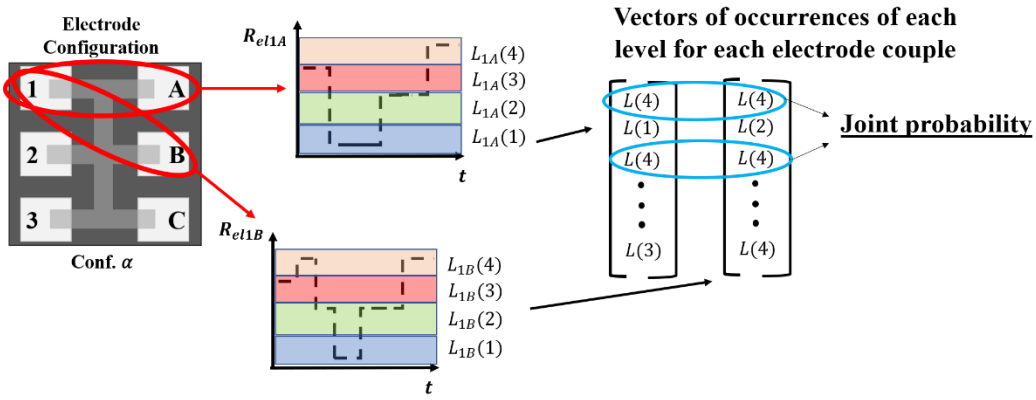

Figure 5-11: Scheme of the computing process of the joint probability for a two-element subset system. The whole system is the cluster-assembled film shown on he left. The units composing the system are the electrode couples to which resistance series data are associated. Each resistance pattern explores different levels (xy graphs for couples 1-A and 1-B in the figure) with a certain probability. A subset of the system composed by two electrode couples (1-A and 1-B) is selected, each resistance series is divided in 4 fundamental levels (colored bars in the graphs). To compute MI and I, a subset of the system is selected (the ensemble X_1^2 composed by the two resistance-series of data for electrodes 1-A and 1-B). The levels for each unit are stored in two vectors and the joint probability is computed normalizing the counts of the occurrences of the levels in time (in the figure the counts relative to the joint probability $p(L(4), L(4))$ are shown, highlighting with blue ellipses the occurrence of the levels).

The resistance series data are measured for each couple under the sub-threshold voltage after the application of the over-threshold signal. All the sub-threshold measurements are cumulated to compute the entropy of the couples under examination. The entropy for a resistance data series is computed fixing the number of levels to 4 and computing the joint probability on a fixed number of electrode couples (see Figure 5-11 for an example on a system composed by two electrode couples). The number of levels is fixed to 4, evaluating the more recurring pattern of experimentally measured resistance for each electrode couple (see Figure 5-5 and Figure 5-8). Note that in this way, only the information about the occurrence of the switching is considered, the information carried out by amplitude of the switch is washed away. The mutual information and the averaged integration for each electrode couple subset is computed following the definition (5.2) and (5.3).

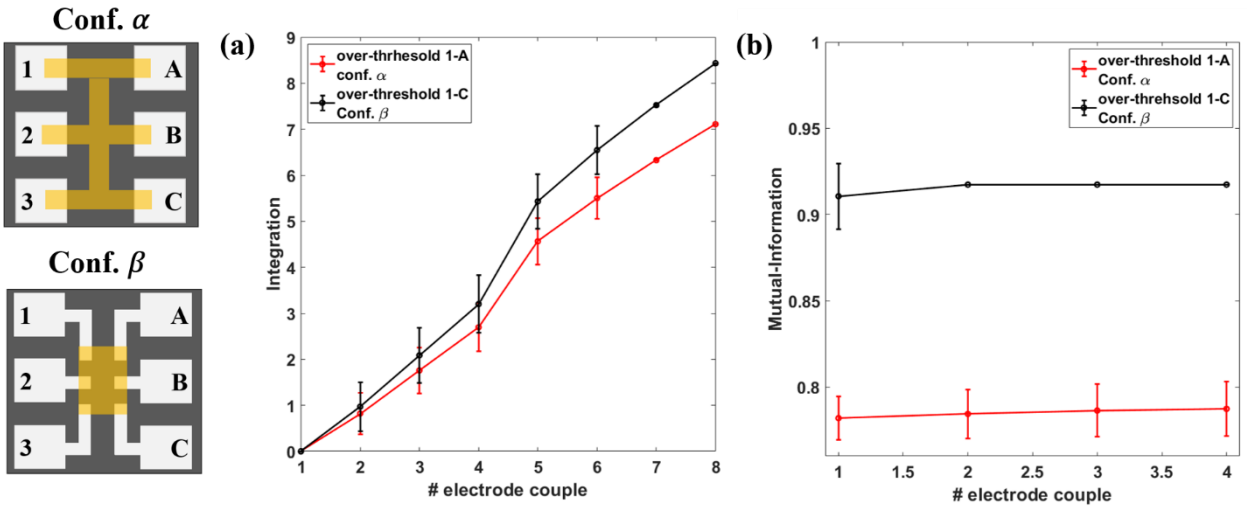

Figure 5-12: Left the scheme of the electrode configurations for Conf. α and Conf. β devices. Right, the Integration and the Mutual Information graphs. (a) The integration as function of the number of electrode couples for one Conf. α (red line) and one Conf. β (black line) device. (b) The mutual information as function of the number of electrode couples for one Conf. α (red line) and one Conf. β (black line) device.

In Figure 5-12 the integration (a) and the mutual information (b) for two devices (Conf. α and Conf. β) are shown. The two configuration classes show the same trend, and they share some features. The trend of Integration I as function of the number of electrodes is increasing with a slightly deviation from the purely linear one. This should be due to the correlations that became evident when the resistance data of multiple electrode couples are considered. The averaging process realized in collecting the current flowing from large area of the film, compared with the characteristic length of the structural properties at the nanoscale, result in a strong integration process. Mutual information shows the same trend for the two samples, but different values are assumed. Conf. β sample shows a higher mutual information, since this class has the higher linear correlation coefficients (as reported in Figure 5-9). The high density of electrodes on the surface of deposited cluster-assembled films determines a high correlation in the activity of electrode couple under the flowing of a current.

Although the Conf. α sample is less correlated (as previously shown in the Figure 5-9), it explores a higher number of resistance levels and the behaviour of the resistive switching activity for each electrode couple can be strongly influenced by the combinations of electrodes chosen during the over-threshold signal application. In Figure 5-13 Integration and Mutual Information obtained after the application of repeated (about 10 times) over-threshold voltage pulse train (voltage between 5 V and 35 V, number of pulses in the range 10-40) on two different electrode combinations are reported.

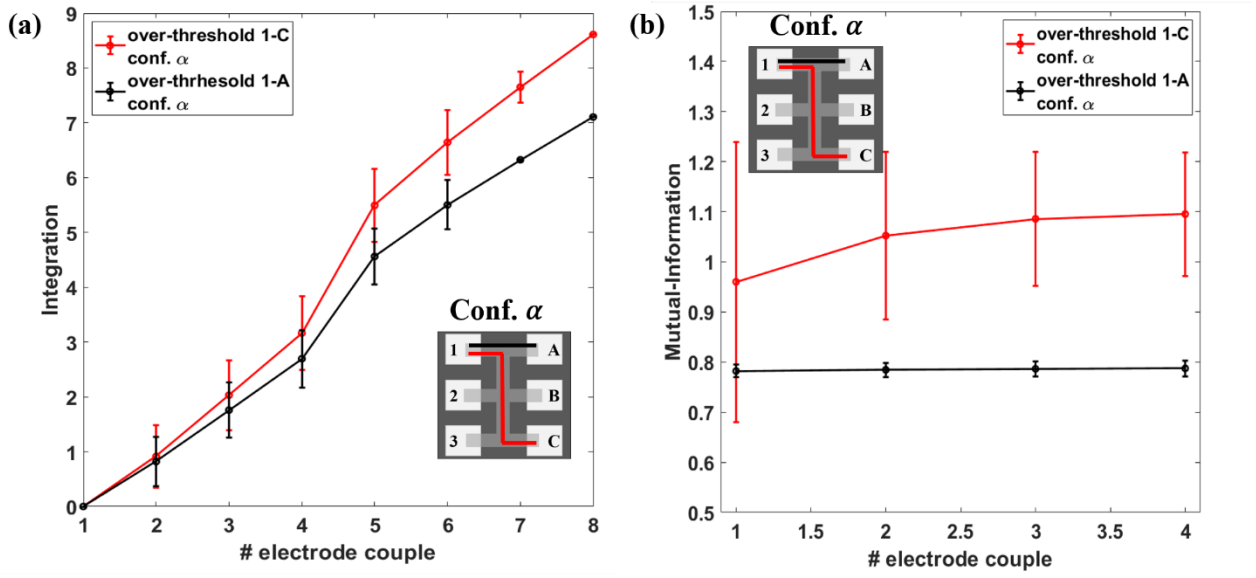

Figure 5-13 (a) Integration as a function of the number of electrode couples for a Conf. α device for two different over threshold inputs, one at electrode couple 1-A (red line) and one at 1-C (black line). The inset shows the electrode scheme. (b) The mutual information as function of the number of electrode couples for a Conf. α device for two different over-threshold inputs, one at electrode couple 1-A (red line) and one at 1-C (black line). The inset shows the electrode scheme.

The system shows an increasing trend in the Integration graph (panel (a)). In the case of over-threshold signal on a large region of the films, the electrical activity of each electrode couple results in a more integrated behaviour. At the same way, Mutual Information, shown in panel (b), has an increasing trend, faster for the application of the over-threshold on a larger region of the cluster assembled film, showing a more correlated behaviour among the electrical activity of each electrode couples. The results should be attributed to the longer path followed by the current during the application of the external stimulus. A higher area of the film is involved in the processes and the resistance between a higher number of electrode couples is modified.

These data show that the spatial organization of the electrodes used to inject and extract electrical current in the nanostructured gold film, influences the overall electrical behaviour: the resistive switching activity depends both on the applied signal and on the electrode configurations. Correlations naturally emerge among the electrical behaviour of different regions in the cluster-assembled films. The restive switching activity can be viewed as resulting from the collective structural and transport properties of the nanostructured film.

Two classes of sample were analysed, with different geometry; results suggest that the geometric parameters chosen during the fabrication stage influence the overall resistive switching properties. In addition, it is inferred that different input/output electrode configurations can be selected to control

the degree of correlations between different regions of the nanostructured film, in response to an external stimulus.

This opens new and interesting perspectives for the use of multi-electrode cluster assembled film in information elaboration processes. In the last part of the chapter, the multi-electrode cluster-assembled film is considered as a device with a global resistive switching activity determined by the electrical behaviour of smaller parts: the single electrode couples. This allowed to study the correlations arising in the electrical activity of different film region after the application of external stimuli as the same manner of biological neural network. Results suggest that electrical activity emerging form the organization of currents flowing through the different couple of electrodes connected to the film, results in complex organization with non-local and correlation properties.

Cluster-assembled gold films are a system with non-linear conduction properties, capable of generating a large amount of resistance levels with high rate in time and harnessing the spatial organization. These features have been used, as described in the next chapter, to fabricate a device capable to efficiently perform classification.

6. The receptron

As discussed in the Introduction, the emulation of brain-like data processing can be based on the use and integration of artificial components able to reproduce the working features of neurons, neuron networks, and synapses [4,36,43]. Different models have been proposed to replicate the neuron behaviour [7,27,30,32], among them, one of the most explored is the perceptron [61,62]. A single layer perceptron can be used only for the classification of linearly separable patterns and this limits significantly the range of its use. A neural network composed by two or more layers (multilayer perceptron) can process non linearly separable Boolean functions and thus perform very complex computations [67,68]. This approach is however based on digital computation and on schemes typical of Turing machines. From this point of view it cannot be considered as "neuromorphic" [4].

In this chapter I will introduce a new paradigm and describe the fabrication and characterization of a device, called "receptron", made of a generic pattern of electrodes interconnected by cluster-assembled Au film with a thickness above the electrical percolation threshold. **The receptron is a classification tool that can receive inputs from different electrodes and generate a complete set of Boolean functions of n variables.**

6.1. The perceptron as a classification tool

In biological systems, a neuron fires only if the total weight of the synapses that receive pulses in a short period (period of latent summation) exceeds a threshold [36]. The perceptron produces a binary output by thresholding the weighted sum of the inputs. The output is obtained by summing the weighted inputs as $\sum = w_1 x_1 + \cdots + w_N x_N$ and by mapping Σ to the output value $F(\Sigma)$, where F is the perceptron output function. At any input $x_1, \ldots, x_N$, the corresponding weight $w_1, \ldots, w_N$ is associated through training algorithms to update the weights until they produce the targeting output values [2,72]. In this configuration, a well-defined association between the weights and the corresponding inputs exists due to the discreteness of the elements determining the weights. The use of a system based on perceptrons to perform input classification and as Boolean function generator is limited by the following drawbacks:

1) the necessity to add more layers, and a higher number of inputs, to approximate a larger spectrum of functions (see the XOR problem for the single layer perceptron in [61,68])

2) need of time-consuming training algorithms,

3) the identification of a suitable physical implementation that can be energy efficient and offer simple integration process and high precision.

Point 2 and 3 are strongly correlated since the training process and the weight updating represent the main source of energy and time consumption, also determining the computing speed and errors in the recognition of inputs [2,82].

Major efforts have been concentrated on the development of suitable hardware to emulate synapses, which are the most numerous processing elements in ANNs. Recently memristors have been proposed for the physical realization of the perceptron as synaptic weights in order to implement a limited number of Boolean functions [63,223,224]. An approach based on the Stochastic Gradient Descent algorithm to efficiently reconfigure synaptic weights offered the possibility of implement linearly separable operations with more than two inputs [68]. In general the use of memristors introduced interesting possibilities for the fabrication of analogue systems able to encode synaptic weights directly in their conductance and thus achieve substantial speedup and power reduction compared to standard digital hardware [63,225]. Complex ANN based on perceptrons organized in crossbar array configurations [226] or with a single-memristor-layer input using back-propagation algorithms to optimize the weights on a training dataset and to perform classification and prediction on previously unseen set of data, have been demonstrated [63,225].

In the last year, to obtain systems characterized by the capability of high amount of information processing and high scalability, materials composed by a large number of non-linear junctions at the nanoscale were considered [17–19,104,111,114]. These systems, obtained by the self-assembling of nano-objects like nanoparticles and nanowires [19,104], present non-linear conduction properties characterized by spatiotemporal correlation in the electrical activity [18,111,114]. This behaviour emerges from the presence of high density of non-linear and recurrent junctions formed at the nano-scale during the fabrication process [19,111,114].

As shown in the previous chapters, cluster-assembled gold films present a multi-state resistive switching under the application of external voltage bias, and spatiotemporal correlations in the electrical activity in response to external over-threshold stimuli. The high number of non-linear junctions determine a multi-level conductivity behaviour under the application of a voltage bias, that allow high amount of information process. The switching behaviour is automatically triggered by the current flowing through the cluster-assembled film, following the paths of lowest resistances and triggering several parallel switching events that singularly dissipate a low amount of power. This process is intrinsically efficient, since does not require the control of the switching activity of each junction. As shown in Chapter 5, non-local and correlated electrical behaviour emerge naturally form the application of over-threshold signals to one region of a multi-electrode cluster-assembled film.

In the following I present and discuss a general approach to the weight optimization problem that does not need a precise knowledge of the conductivity evolution of a physical substrate and can

operate in an intrinsically stochastic environment. The use of nanostructured materials to implement new computing devices will be taken under examination in an experimental study and discussed.

6.2. The singular theorem

A notation to formally describe the perceptron is given in the following. The capability of a perceptron with N inputs of generating a limited subset of the N-bit Boolean functions, the singular one, is discussed.

Let $f: B^N \rightarrow B = \{0,1\}$ be Boolean functions of a N-dimensional input system and $\vec{x}$ the N dimensional vector of the binary inputs. A Boolean function $f(\vec{x})$ for a N-dimensional input system is completely describe by the truth table, that gives the binary output value associated to each of the 2^N input vectors $\vec{x}$. The example given in Table 6.1 is the function $f(x_1, x_2)$ that implements the XOR for 2-dimensional input system.

x_1	x_2	$f(x_1, x_2)$
0	0	0
0	1	1
1	0	1
1	1	0

Table 6.1

The *multiplicity m* of Boolean function *f* is defined here as the number of '1' values assumed by the function in the truth table; for example, the function in Table 6.1 has multiplicity $m = 2$. I is thus possible to classify the functions implemented by a perceptron by their multiplicity, and we concentrate on a particular class, the singular functions. A singular function f^s is defined formally as:

$$f^s = \begin{cases} 1 & \vec{x} = \vec{x}_0 \\ 0 & \vec{x} \neq \vec{x}_0 \end{cases},$$

where $\vec{x}_0$ is one particular combination of the 2^N possible N-dimensional binary inputs $\vec{x} = (x_1, \dots, x_N)$. The singular functions have multiplicity $m = 1$. Since the number of combinations of a N-inputs system is 2^N the maximum number of distinct singular functions will also be 2^N.

Singular functions are a limited subset of the whole Boolean functions set and they have interesting properties. They represent the minimum set of functions necessary to produce any Boolean function through simple binary linear combinations (OR operations):

$$f = \sum_{i}^{2^N} k_i \, f_i^s \qquad (6.1)$$

where k_i are binary coefficients and f_i^s are distinct singular functions. Note that the multiplicity *m* of the function *f* corresponds to the number of the coefficients $k_i = 1$ of the linear combination in Eq. 1. In addition, singular functions are useful in tasks like pattern recognition since they activate the perceptron only for a particular combination of the binary inputs [64].

In the next section a formal demonstration for the existence of a set of weights that implement the singular functions in a perceptron will be given.

6.2.1. The Singular theorem

Let *P* be a perceptron with *N* binary inputs $(x_1, \dots, x_N)$, *s* the threshold value of the output function and $(w_1, \dots, w_N)$ the synaptic weights, the perceptron activation

$$\sum_{i}^{N} w_i x_i \geq s \qquad (6.2)$$

occurs and it is singular (the multiplicity of the implemented function is equal to 1) when the following statements hold:

i) $\sum_i^N w_i x_i = s$ (6.3)

ii) $w_i > 0 \; \forall \, i : \; x_i = 1$ (6.4)

iii) $w_i < 0 \; \forall \, i : \; x_i = 0$ (6.5)

Proof:

Let $(a_1, \dots, a_N)$ be inputs satisfying the conditions of Equations 6.3-6.5 and $(x_1, \dots, x_N)$ arbitrary inputs. The input indexes $\{1, \dots, N\}$ can be separated as

$$i \in I_0 \text{ if and only if } a_i = 0 \qquad (6.6)$$

$$i \in I_1 \text{ if and only if } a_i = 1 \qquad (6.7)$$

where I_0 and I_1 are index sets so that $I_0 \cap I_1 = \emptyset$ and $I_0 \cup I_1 = \{1, \dots, N\}$, thus one can write

$$\sum_{i}^{N} w_i x_i = \sum_{I_0} w_i x_i + \sum_{I_1} w_i x_i \tag{6.8}$$

From Eq. 6.5 one can write:

$$\sum_{i}^{N} w_i x_i = \sum_{I_0} w_i x_i + \sum_{I_1} w_i x_i \leq \sum_{I_1} w_i x_i \tag{6.9}$$

that becomes from Eq. 6.3 as

$$\begin{aligned} \sum_{i}^{N} w_i x_i = \sum_{I_0} w_i x_i + \sum_{I_1} w_i x_i \\ \leq \sum_{I_1} w_i x_i \leq \sum_{I_1} w_i a_i \end{aligned} \tag{6.10}$$

From Eq. 6.2 and since $\sum_{I_1} w_i a_i = \sum_{i=1}^{N} w_i \, a_i$, we obtain

$$\begin{aligned} \textstyle\sum_{i}^{N} w_i x_i = \sum_{I_0} w_i x_i + \sum_{I_1} w_i x_i \leq \sum_{I_1} w_i x_i \leq \\ \textstyle\sum_{I_1} w_i a_i = \sum_{i=1}^{N} w_i a_i = s \end{aligned} \tag{6.11}$$

and hence

$$\sum_{i}^{N} w_i x_i \leq s \tag{6.12}$$

Equation 6.12 shows that the sum of any weighted inputs is less or equal to the threshold obtained with the sum of the weighted inputs $(a_1, \dots, a_N)$ that follow the hypothesis. This means that inputs different from $(a_1, \dots, a_N)$ will not active the perceptron. Furthermore, as

$$\sum_{I_1} w_i x_i \leq \sum_{I_1} w_i a_i = s \tag{6.13}$$

one finds from Eq. 6.3

$$\sum_{I_1} w_i x_i = \sum_{I_1} w_i a_i = s \tag{6.14}$$

if and only if $x_i = a_i = 1 \; \forall \; i \in I_1$. By substituting Eq. 6.14 in Eq. 6.8 one obtains:

$$\sum_{i}^{N} w_i x_i = \sum_{I_0} w_i x_i + s \tag{6.15}$$

from Eq. 6.3 one finds

$$\sum_{i}^{N} w_i x_i = s \tag{6.16}$$

if and only if $x_i = a_i = 0 \; \forall \; i \in I_0$.

Equations 6.14 and 6.16 show that the equality in Eq. 6.12 occurs for $(x_1, \dots, x_N) = (a_1, \dots, a_N)$. The inputs $(x_1, \dots, x_N)$ will active the perceptron when $(x_1, \dots, x_N) = (a_1, \dots, a_N)$. The activation is unique and occurs only for a particular combination $(a_1, \dots, a_N)$ of the inputs.

As an example, I apply the singular theorem to a 3-bit input system. The singular function is solved by setting the perceptron weights in a deterministic way without the needs of iterative algorithms. One can assume that the perceptron weights should be determined to solve the singular function shown in Table 1.

Inputs	**Output**
(0,0,0)	0
(0,0,1)	0
(0,1,0)	0
(0,1,1)	1
(1,0,0)	0
(1,0,1)	0
(1,1,0)	0
(1,1,1)	0

Table 6.2.

Note that the function in Table 6.2 is singular since the activation occurs only for the particular combination $(x_1, x_{2,} x_3) = (0,1,1)$. Following the hypothesis of the theorem in Eq.s 6.3, 6.4, 6.5, we immediately write

$$(w_1, w_2, w_3) = (-\varepsilon, \tfrac{s}{2}, \tfrac{s}{2})$$

where $\varepsilon > 0$ and $s > 0$ is the perceptron threshold. Note that the singular theorem offers the possibility to know the correct weights deterministically, without the use of iterative algorithms.

6.3. Weighting process

The polymorphic behaviour of cluster-assembled films is both functional and physical since the film resistance is dependent from the past history and from the topology of the electrical pathways resulting from the organization of nanojunctions constituting the film. As shown in the previous chapters, conduction properties of the nanostructured films are characterized by non-linear relation between current and voltage, and resistive switching activity triggered by the application of voltage pulses higher than a certain threshold. In addition, as shown in Chapter 5, the multi-electrode films show a correlated activity for different electrode couples that can be controlled selecting different current paths to alter the resistance of different film regions. Contrarily to the perceptron model, it is not possible to provide a direct geometric and uniform association between the conduction of each film region and the input at the corresponding couple of electrodes.

To exploit the properties shown by nonstructured films, a generalization of the perceptron is here proposed.

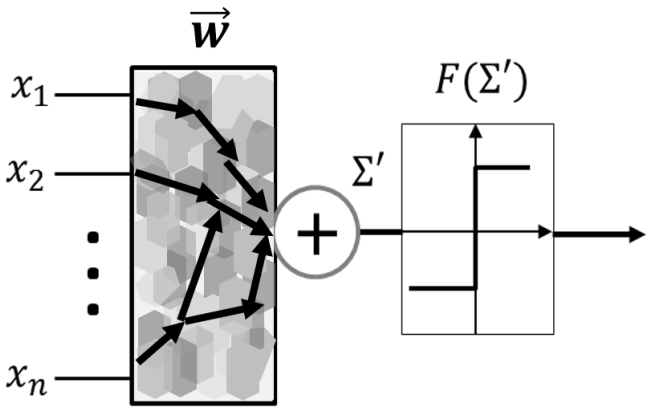

Figure 6-1 Schematic model of a input-dependent and distributed weight device. The distributed weights $\vec{w} = (w_1, \dots, w_N)$ are represented with the rectangular region connected to the adder Σ'. The function F implements the thresholding process to obtain a binary output.

A scheme is shown in Figure 6-1: in a device based on cluster-assembled films, weights are input dependent and they are determined by a network of non-linear junctions that rearrange under the action of an applied voltage thus obtaining different conducting pathways. The non-local evolution of connectivity due to the application of external stimuli (over-threshold applied voltage) leads to the formation of conducting pathways characterized by a complex topology and network connectivity. The topological organization of the conducting pathways determines the weights of the inputs. In this configuration, the weight between any given pair of "neuron terminals" is regulated by the global response of the network to external stimuli, as disclaimed in Chapter 5. In other words the

weights are functions of a convolution of the spatial location of the input electrodes (input topology) with the conducting path topology of the network, so that the device maps the weighted inputs $\Sigma' = x_1 w_1(x_1, \dots, x_n) + \cdots + x_n w_n(x_1, \dots, x_n)$ to the output value $F(\Sigma')$. The perceptron is hence a particular case of this new model, since the perceptron weights are independent constants $w_1(x_1, \dots, x_n) = w_1, \dots, w_n(x_1, \dots, x_n) = w_n$.

The distributed weights make the system input dependent. This means that the weights $\vec{w}_{ST} = (w_1, \dots, w_N)$, whose existence is proved by the singular theorem, for a given singular function are not constants by changing the inputs as instead happens for a perceptron. In this condition the singular functions are again solved when the variation of the weights occurs in a particular region around $\vec{w}_{ST}$. Let us consider for example a 2-bit inputs system as reported in Table 6.3.

Inputs	Output
(0,0)	0
(0,1)	1
(1,0)	0
(1,1)	0

Table 6.3

The singular theorem applied to the input $(0,1)$ provides the weights $(w_1, w_2) = (-\varepsilon, s)$. These weights can be represented as a point in the weight-space as shown in Figure 6-2. Despite the weights varying by changing the inputs, the singular function remains solved if the weights are in the dashed space regions $D(0,0)$, $D(1,0)$, $D(1,1)$ shown in Figure 6-2 and corresponding to the inputs $(0,0)$, $(1,0)$, $(1,1)$, respectively.

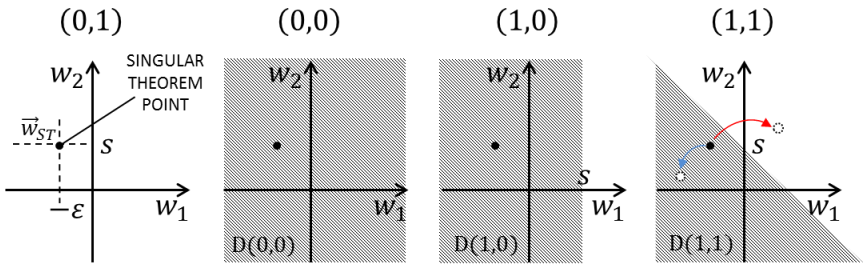

Figure 6-2: Representation of the weight-space regions to obtain the singular function reported in the table 2 for the inputs (0,0), (1,0) and (1,1). The blue and red arrows show two possibilities for changing the $\vec{w}_{ST}$ point according to the input (1,1). In particular, the blue arrow shows a change inside the region D(1,1) necessary to solve the singular function again. On the contrary the variation of the weights shown by the red arrow does not allow the solution of the singular function.

More generally one can write that the singular function is solved in an input-dependent system when

$$\vec{w}(\vec{x}) \in D(\vec{x}) \; \forall \; \vec{x} \neq \vec{x}_0 \tag{6.17}$$

$$\vec{w}(\vec{x}_0) \notin D(\vec{x}_0) \tag{6.18}$$

where $\vec{x}_0$ are the activation inputs and $D(\vec{x})$ are the regions of the weight-space such that

$$\left\{\vec{x} : \sum_i^N w_i x_i < s\right\} \tag{6.19}$$

Thus, the singular theorem gives:

$$\vec{w}_{ST} \in D(\vec{x}) \forall \; \vec{x} \neq \vec{x}_0 \tag{6.20}$$

$$\vec{w}_{ST} \notin D(\vec{x}_0) \tag{6.21}$$

To summarize one can say that in a perceptron the weights are input-independent and the singular functions are obtained if Eqs. 6.20, 6.21 are obeyed. In the model proposed here, the weights are distributed in an extended region, input-dependent, and the singular functions are obtained if the Eqs. 6.17, 6.18 hold. Notice that Eqs. 6.17, 6.18 are a generalization of Eqs. 6.20, 6.21.

I name a device based on a complex network of nanojunctions that fulfils the outlined properties **"receptron"**. Since in a receptron the weights are not spatially localized and input dependent, a training method that does not need the precise knowledge of the weight evolution is proposed and discussed. As we will see more in detail, the variability of the receptron to implement functions exceeds the case of a single perceptron since it can also implement non-linearly separable functions.

6.4. Receptron hardware

6.4.1. Hardware description

As shown in Chapter 5, cluster-assembled films present correlated regions with different resistance values and with non-linear conduction properties. In addition, the conduction properties of different regions can be controlled by the application of over-threshold signals applied to one

electrode-configuration exerting non-local and correlated effects on the evolution of the electrode couple resistances.

To exploit the outlined properties, in this section a physical implementation of the receptron model is proposed. In Figure 6-3 the scheme of a 3-bit receptron is shown. A multi-electrode cluster-assembled film is used to implement the weighting of the input currents that flow through the nanostructured film following the paths of minimum resistance. The inset in the figure shows the non-linear trend of the current as function of the applied voltage and the occurrence of resistive switching events that change the slope of the curve. For these reasons, the resistance of the electrode couples depends on both the applied voltage and the over-threshold pulses applied in the past history of the device.

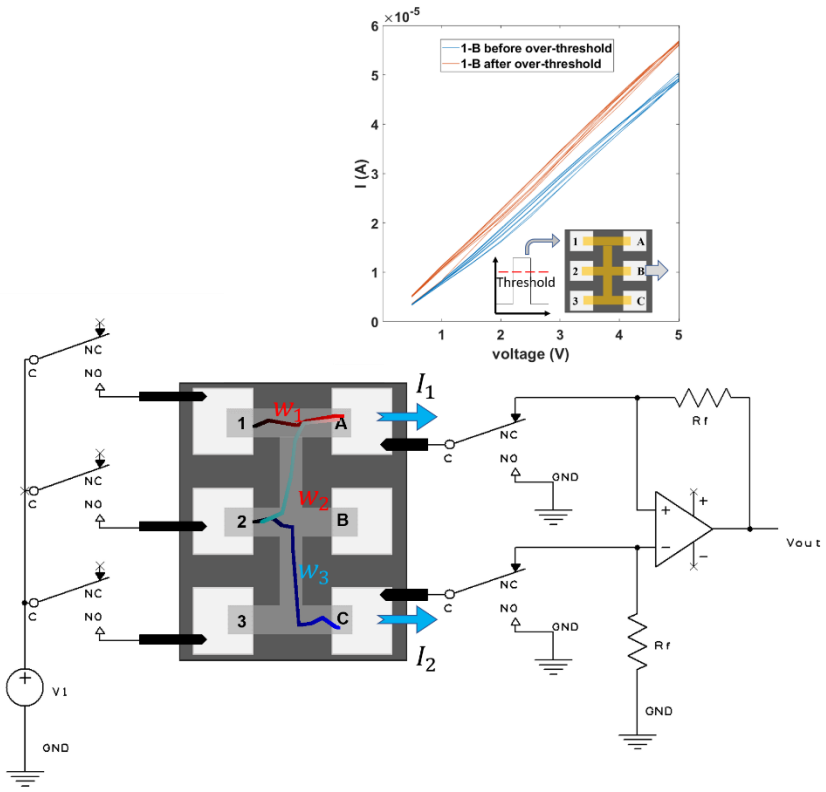

Figure 6-3: Circuital scheme of the receptron. The multi-electrode cluster assembled film is connected to the voltage power supply on the left, through one relay for each electrode. On the right, two electrodes are connected to the relay that can switch between an op-amp, in difference amplifier configuration, and ground. The op-amp stage implements the adder. I_1 and I_2 are the output current flowing though electrodes A and C of cluster-assembled film. Electrode B is unused. The currents I_1 and I_2 results form the sum of the local currents flowing through the cluster-assembled film (colored lines in the figure) that follow the paths of minimum resistance (the gradient color ramp in figure states for the voltage gradient through the films). At each local current is ideally associated a weight determined by the resistance in the different regions of the cluster assembled film. The inset shows the trend of the voltage-current curve measured at the couple 1-C in the arrange 1 to 5 V and the effect of the application of an over-threshold signal. The curves non-linear and the and different slopes because of the occurrence of switching activity.

To exploit the non-linear conduction properties and the non-local resistive switching activity of the multi electrode cluster-assembled films, a circuit was designed as shown in the scheme of Figure 6-3. The multi-electrode cluster-assembled film is connected on one side to the voltage power supply line through relays and electrode 1, 2 and 3 are used as inputs. Two output electrodes, A and C, are used to collect the current flowing though film when it is injected form the input electrodes and they are connected to two relays that can switch between the ground and an op-amp that is employed in difference amplifier configuration [22]. When the relays connect the cluster-assembled film to the amplifier, the voltage output $V_{out}$of the device is related to the difference of the input currents I_1 and I_2 following the relation:

$$V_{out} = R_f(I_2 - I_1) \quad (6.22)$$

R_f is the feedback resistance as shown in Figure 6-3. Since the cluster-assembled film is characterized by non-linear conduction properties and its resistance can be changed upon the application of over-threshold voltage signals to the input electrodes. The currents I_1 and I_2 depend by the inputs and the number of applied over-threshold signals:

$$I_1 = I_1(V_1, V_2, V_3, n) \quad (6.23)$$
$$I_2 = I_2(V_1, V_2, V_3, n) \quad (6.24)$$

In 6.23 and 6.24 the current dependencies are made explicit. V_j is the voltage values applied to j-th input, and *n* states for the n-th over-threshold signal that triggered the non-local resistive switching activity and the currents reorganization in the different film regions.

As a consequence, the output currents I_1 and I_2 are dependent by both the applied voltage at the input electrodes (both the magnitude of the voltage and the electrode-configuration at which the voltage is applied) and by the number of over-thresholding signals applied to the cluster assembled gold film.

To exploit the device shown in Figure 6-3 acting as a Boolean function generator, a protocol, consisting of two main steps, is defined: the *writing* and the *reading* step. During the *reading step*, the device is used to implement a Boolean function. The electrode 1, 2 and 3 are the input electrodes (Figure 6-3), the electrode A and C are connected to the op-amp and the voltage source is maintained to 1 V. The input logic 0 is high impedance state (open relay in Figure 6-3), while the input logic 1 is low impedance state (closed relay in Figure 6-3). They are obtained through the relays connected to input electrodes (see Figure 6-3). The device output is the voltage output V_{out} of the op-amp. To

obtain a logical value, a threshold has to be imposed to the voltage value. For the receptron, a band threshold logic is employed: two voltage thresholds are chosen, the voltage outputs falling inside the band are considered 1 state, otherwise the output values assume the 0 state. V_{out} can be read for each input configuration, hence the Boolean function is completely defined associating a binary value to each input configuration (for example 0-0-0, 1-0-0, …) after the thresholding process. There is no need to store the voltage output of the device, the Boolean function can be read several times until the device will not be reconfigured.

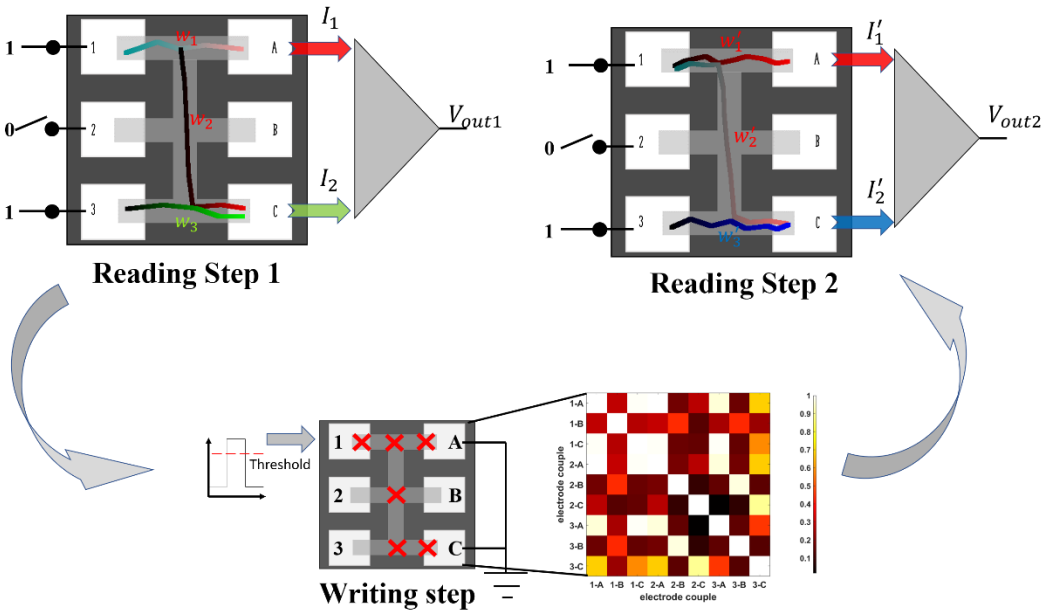

Figure 6-4 Example of one writing step, showing the effect on two reading steps, one before and one after a writing step. Reading Step1, output currents at the electrodes A and B of the cluster-assembled film are the result of the local resistance of each film region that act like a weighting process on the current distribution flowing though the film (colored lines). The different colors states for different implemented weights, while the gradient states for different current intensities. The device in the reading step for input configuration 1-0-1 gives as output the voltage V_{out1}. Writing step, a pulse train, the over-threshold signal, is applied to electrode labelled by 1, A and C are the grounded electrodes. The red crosses indicate the region that can alter their local resistance and cause the current redistribution in the cluster-assembled film. The insight shows the correlation matrix that describe the correlations arising after an over-threshold signal application in the resistive switching activity of different electrode couples. Reading Step 2, the cluster-assembled film implements a new set of distributed weights and the flowing currents reorganize in new paths and intensities. The output currents at the electrodes A and B are different from reading step 1 and this gives a different device output V_{out2}.

The *writing step* is used to reconfigure the device and obtain new Boolean functions. The electrode 1, 2 and 3 are used as input electrodes (see Figure 6-3) and the voltage source is used to apply over-threshold voltage pulse trains. The electrode A and C (Figure 6-3) are connected to ground.

To make clear the process, in Figure 6-4 an example of two reading steps separated by a writing step is shown. The cluster-assembled film implements an initial set of weights, and this

determine the output current I_1 and I_2. During the reading step for the input configuration 1-0-1 a voltage output V_{out1} is measured. The application of an over-threshold voltage pulse train triggers the occurrence of switching events and the local resistance of the film is altered in different regions (writing step). The cluster assembled film implements a new set of weights (reading step 2), currents flowing thought the film redistribute and the voltage output V_{out2} for the configuration 1-0-1 is different form step 2. The writing step implements a new set of weights updating the resistance of different film regions thanks to non-localities and correlations in the effect of the over-threshold signals for the electrical activity of the multi-electrode cluster-assembled film (see inset in Figure 6-4).

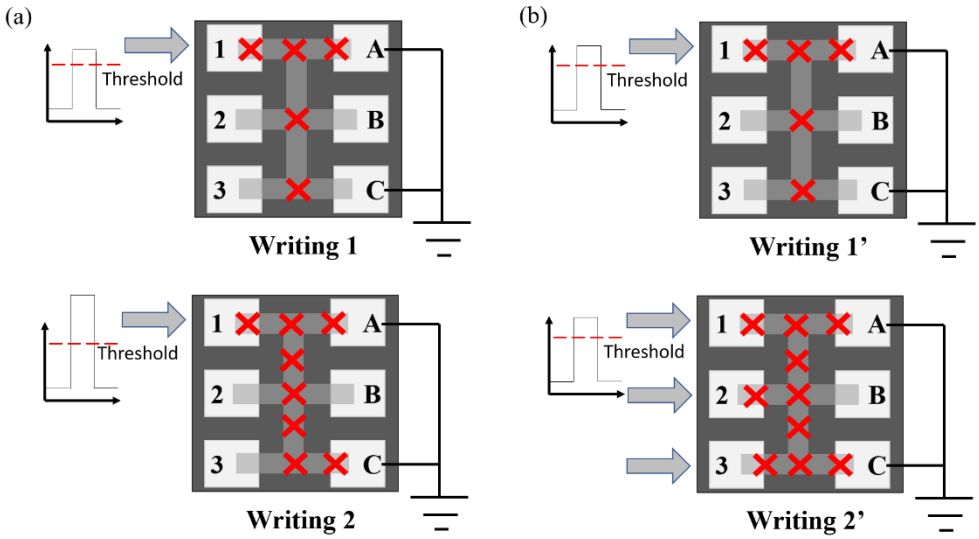

Figure 6-5 Different writing steps that can determine different switching events in the regions of the cluster-assembled gold film (red labels). (a) Two different writing steps are implemented choosing different input voltage pulses. (b) Two different writing steps are implemented choosing different input electrodes.

In order to implement different sets of weights, and different Boolean functions, the writing steps can be iteratively applied to modify the weighting process realized by the cluster-assembled film and produce the desired output in the processing steps.

There are two main ways to carry out the writing steps: choosing different voltage pulse train or choosing different combinations of input electrodes (Figure 6-5). From the results presented in chapter 5, it is possible to infer how changing the electrode configuration used for the writing steps, influences the electrical activity of each region of the film and allows to implement different weighting processes. After each writing step, a reading step can be carried out for each input configuration to check the voltage output obtained after the spatial re-organization of the currents flowing in the film and to evaluate the Boolean function implemented by the device.

6.4.2. Experimental results

We tested the device with over-threshold pulses with height between -35 V and 35 V and width between 0.1 and 0.5 s. The number of pulses for one single train was varied between 20 to 100. During the pulse application, the relay on electrodes A and B are connected to ground (see Figure 6-3) and the selected input electrodes are connected pulse generator. Different combinations of the input electrodes were tested during the writing step to evaluate the possible ways of implementing the sets of weights: the pulses were applied to all the combinations of electrode input (1, 2, 3, 1-2, 2-3, 1-3, 1-2-3, refer to Figure 6-3) with electrode A and C connected to ground.

Figure 6-6 shows the outputs of the device before and after one writing step applied to electrodes '1-2-3' using a train of 10 V pulses (0.5 s width): the differences in the output voltages for the different inputs are clearly visible. Each output is obtained from three consecutive reading measurements, to check the stability of the voltage outputs.

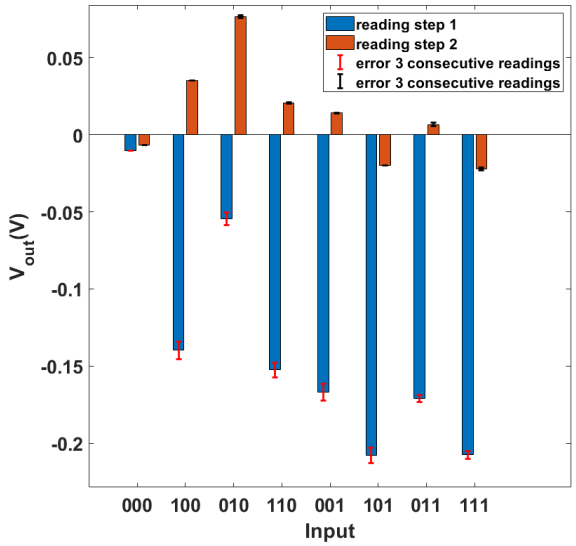

Figure 6-6 Results of two reading steps, one before (blue bars) and one after (orange bars) a writing step showing the voltage outputs measured for each input configuration. The error bars for each output are the standard deviation on three consecutive reading processes for each input configuration. The error is small compared to the differences among the measured voltage outputs before and after the pulse train application. The over-threshold pulses features are: 0.5 s width, height 10 V, they were applied to electrodes 1, 2 and 3. At the top of the histogram bars, the standard deviation of the three measurements for each input is shown.

To evaluate the Boolean functions associated to the voltage output of the device, I stored the measured values on a local computer to analyse the obtained data. I imposed a thresholding protocol to discriminate the voltage values in '0' and '1' logic values, in particular I used a double threshold band: voltage outputs falling between the two thresholds give logic value 1, otherwise 0 value is recorded.

Figure 6-7 shows an example of one reading step with the chosen threshold superimposed to the output indicated by the histogram bars (dashed line). The obtained function is the XOR for a two-input device (input electrodes '1' and '3') (see inset Figure 6-7). Note that the chosen threshold values are noise tolerant since they are well far from the error bars. The example of a two -input function is reported because the XOR function cover an important role. It is thus demonstrated that a single receptron is able to generate a non-linear separable function.

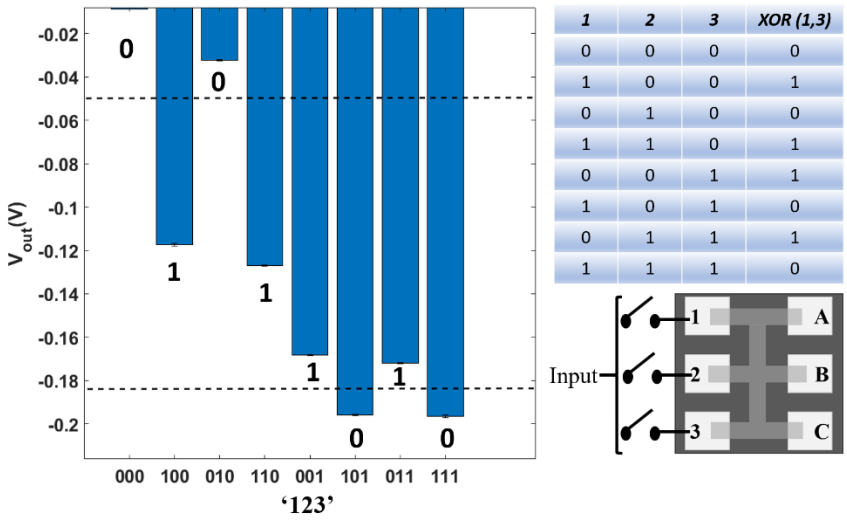

Figure 6-7 Example of two-threshold band imposed to one output. The discontinue lines represent the two threshold values; the voltage values between the threshold acquire the logic value 1, while the voltage values outside the thresholds, are the logic values 0. The result, shown in the truth table on the right, is the XOR function for gate 1 and 3. The inset shows the electrode scheme.

These results suggest that the device can be simply reconfigured to obtain new Boolean functions and no precise knowledge about the implemented weights is needed. The protocol proposed to a practical use of the device is a random search protocol, consisting in the repetitive application of writing processes, with different input electrode combination and different voltage pulse train, until the desired function is implemented.

It was experimentally observed for 3 different devices (built with 3 different multi-electrode cluster-assembled films) that, after the application of 30-40 writing steps, the recorded voltage output can be used to generate up to 10 different 3-input Boolean functions (threshold manually selected in the phase of data analysis and fixed for all the output voltage). Among the generated functions, the singular functions are usually a number of 5-7 on the total of 8.

Non-localities and spatial correlations typical of the re-organization of the nanojunctions of the cluster-assembled film, allow to implement different weight sets distributed on the cluster-assembled film in single writing process. This means that, through few writing steps, in principle, an

extremely large number of weights configurations can be explored to obtain a sub-set of all the Boolean function of a N-bit device.

6.5. Receptron performances

In order to test the receptron performances and the efficiency of the random writing protocol both experimental measures and simulations were carried out. The approach consists in testing the amount of time needed to find a minimum set of different read functions to fulfil the completeness property, or rather the property to obtain all the functions of a N-bit device through a linear combination of the functions contained in the set (OR, AND and XOR operations). The set of the N-input singular functions is a complete set, since a general function can be obtained through OR combinations. The completeness property guarantees a simple hardware implementation of a device able to generate all the N-input Boolean functions. This can be obtained by combining several receptrons through simple Boolean operations (Figure 6-8).

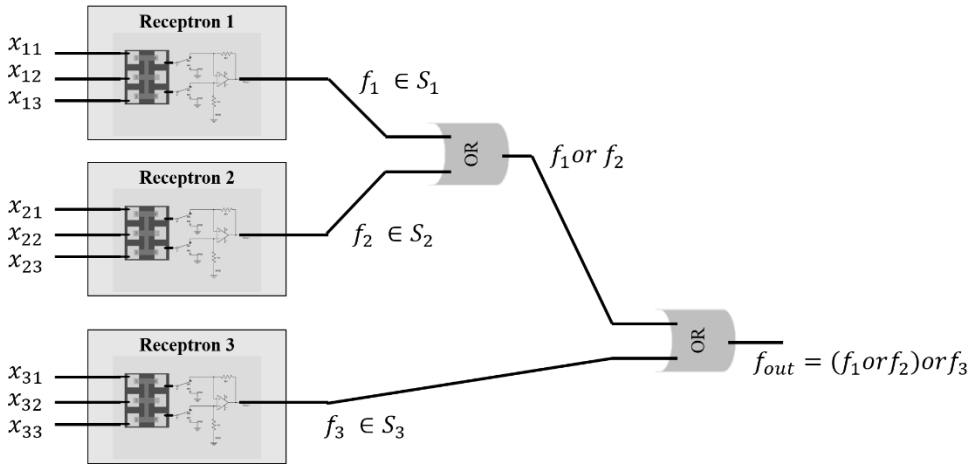

Figure 6-8 Example of a receptron network. Each receptron can generate a complete set of functions. Combining the functions implemented by each receptron through *or* operations, the output function is obtained.

To know the minimum number of receptrons to implement the device with the highest computational power, I define the efficiency as the ratio between the total number of functions and the total number of receptrons needed to generate all the N-input functions:

$$\varepsilon = \frac{2^{(2^N)}}{\sum_{i=1}^{2^{(2^N)}} C(i)} \qquad (6.25)$$

where $C(i)$ is the number of incomplete devices to obtain the i-th function through simple Boolean operations, and the numerator stands for the number of functions for a N-input device. The efficiency

is positive and it can be less than or equal to 1. In the case where a single receptron can generate all the functions, the expression in (6.25) gives maximum efficiency, assuming the value 1: $C(i) = 1 \; \forall \; i$, one single receptron for each N-input Boolean function. If a single receptron generates a partial subset of the total number of N-input Boolean functions, $C(i) \geq 1$ and the efficiency approaches 0 for less efficient devices. Efficiency provides a very interesting information about the completeness of a system since it corresponds to the average number of incomplete devices necessary to realize a complete single-output Boolean-system.

As an example, let us consider a receptron that can solve a complete set of singular functions. From Eq. 6.25 the efficiency is given by

$$\varepsilon = \frac{1}{2^{N-1}} \qquad (6.26)$$

The result expressed in (6.26) can be obtained considering that the number of singular functions needed to obtain a N-input Boolean target function is equal to the multiplicity of the target function. In the case of 3-bit device, N=3, the efficiency is equal to 0.25. With 4 receptrons, it is possible to obtain a device that generates all the 256 3-bit functions.

Since the weights implemented during the writing process are input dependent, to obtain a complete set of singular functions the receptron should satisfy Eq.s 6.17 and 6.18 for each combination of the inputs. The input-dependent behaviour of the receptron and the random nature of the writing process, can generate conditions where some singular functions cannot be realized for a limited variability of the distributed weights obtained during writing process. The missing singular functions can be obtained from others auxiliary functions (not singular) through logic operations. This method allows the realization of a complete device, despite the efficiency will be necessarily reduced as shown in Figure 6-9 (Left and Middle panels).

In addition, the high degree of freedom offered by the polymorphic behaviour of a receptron generally introduce functions that add to the singular ones. It is obvious that by adding different functions solved by the receptron, the overall efficiency increases. This means that a high variability obtained in the writing processes, due to non-locality effects of the over-threshold applied signals, gives a fundamental gain of the overall efficiency (see Figure 6-9 (Right)). Before to show the experimental results, a simulation is carried out to evaluate the efficiency of the outlined approach to implement a Boolean function generator.

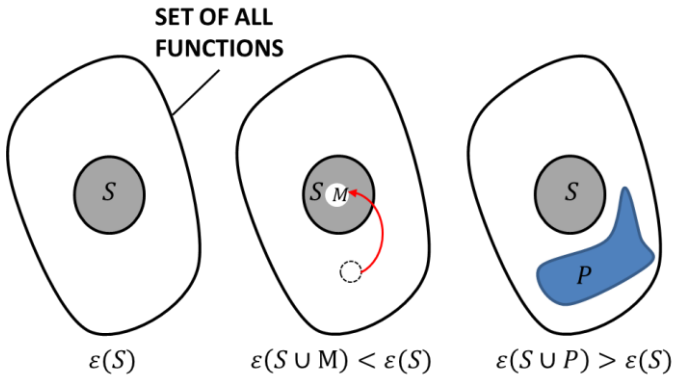

Figure 6-9: Efficiency of complete devices shown with Eulero-Venn diagrams. (Left) Representation of the singular functions set S as fundamental sub-set for the completeness of a device that exploits linear combinations through OR operations. $\varepsilon(S) = 1/2^{n-1}$ is the efficiency of the set S. (Middle) A set of singular functions $S = S' \cup M$ generated through auxiliary functions (not singulars) reduces the device efficiency making the device complete. Here S' is the incomplete set of singular functions and M is the set of missing singular functions obtained using logic operations of non-singular functions. (Right) The complete set S is always necessary for the completeness of the device, additional functions (set P) increases the overall efficiency.

Since the receptron, through the writing processes, generate a set of Boolean functions random sampled from the set of all the possible N-input functions, the properties of the obtained functions and of the Boolean operations used to implement the combinations of different devices, are now considered. The simulation is realized as explained in the following: 1) the set of 3-input singular functions is generated; 2) at each step of computation, a certain number of singular functions are substituted with a 3-bit function with multiplicity m > 1; the new functions are randomly generated fixing the number of '1' values in the function output and randomly disposing the '1' in the 8-dimensinal vector. 3) The number of substituted singular functions is increased after each step of computation.

To evaluate the effects in substituting the singular functions, the efficiency is computed at each step with the combinations of functions in the resulting set though OR and XOR operations. I report in Figure 6-10 (a) the results obtained by simulating the generation of a set of Boolean function through functions with multiplicity m = 4. The figure shows efficiency dependency on the number of singular functions in the set for three different Boolean operations is reported. At each missing singular function, a multiplicity 4 function, with four '1' output values uniformly distributed in the output vector, was inserted. The OR operation requires all the singular functions to converge (blue curve), while the XOR improve the efficiency (black curve). Another method to increase the efficiency and reach the completeness is to employ multiple Boolean combination like XOR and OR (red curve).

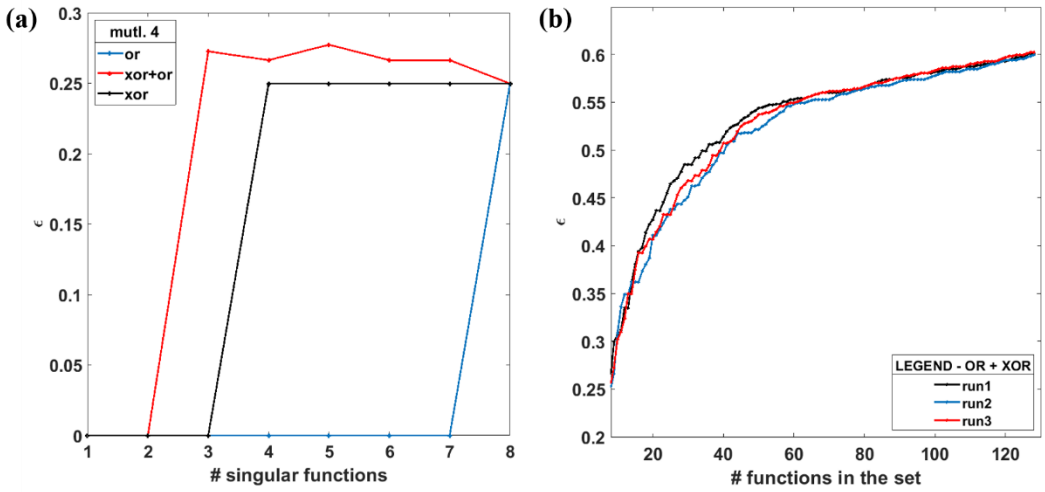

Figure 6-10 (a) The simulated efficiency as function of the number of singular functions in set 3-input functions. The missing singular functions are substituted with multiplicity-4 functions. (b) The efficiency as function of the number of randomly generated function for a 3-input system. The figure reports three different simulation results.

The reported simulated results are general, and the main features are maintained under the random variation of the functions in the set.

To check how the efficiency scales with the number of generated functions, I report in Figure 6-10 (b) the efficiency trend as function of the number of functions randomly generated. The efficiency is computed starting from a set of 8 functions, 4 singular and 4 others randomly added ones. Each new function is randomly generated among the 256 possible 3-input functions, choosing the number of '1' values in the output and then adding these in random position. The aim is to simulate the random generation of functions from a single receptron. In the figure, three different simulation runs are reported: it is possible to observe that, for a relatively low number of randomly generated functions, the efficiency value rapidly increases up to 0.5. This means that with two receptrons devices it is possible to generate all the 3-bit functions within a very low number of random writing processes. All the three simulations report similar results, stating that the approach does not need the generation of a particular class of functions.

In conclusion, the simulations give some useful information: 1) the random training protocol can reach high efficiency both in time performances (few writing steps to reach an efficiency equal to 0.5) and the device integration (simple logic combination of receptrons to obtain a complete device using simple logic operations, OR and XOR). 2) the receptron architecture can efficiently exploit the random element present in the writing process and it does not need a precise knowledge of the generated functions during the writing protocol. This means that variations in different devices to imperfections in the fabrication processes and little variations during the writing process, for example due to noise, do not affect the performances of the designed architecture.

In order to demonstrate the performances of the receptron, also experimental measures are carried out. I used a random writing protocol applying voltage pulses with a time width in the range of 0.1 to 0.5 s, voltages from -35 V up to 35 V at different combinations of electrode couples, for roughly 100 different writing processes, with the pulse train features described above, on several electrode couples. The duration of a single writing step is determined by the time period of the voltage pulses (max. 1 s) and the number of applied pulses (max 40). The maximum time needed for a single writing step is about 40 s. After the application of the writing processes, the outputs are recorded and stored on a computer for the analysis. Conf. α and Conf. β devices were tested.

A routine developed in Matlab is used to select several threshold values and each couple of thresholds is applied to the recorded voltage outputs to obtain a set of Boolean functions. The thresholds are computed selecting one voltage value v inside the interval of the measured minimum and the maximum and, from this, two thresholds are obtained summing and subtracting a constant c. The value of c is varied inside the same interval, to obtain band with different amplitudes. Thanks to this approach it is possible to: 1) evaluate the best threshold value for the device, performing a classification of the obtained Boolean functions (see below); 2) explore the properties of the different set of functions obtained directly form experimental results, without the need to perform optimization procedures.

The set of obtained Boolean functions can have different properties, since a random searching protocol is applied. In order to explore which of these properties naturally emerge, I checked for the existence of a threshold band that can recover the highest set of singular functions. In Figure 6-11 (a), the number of functions with a given multiplicity for the experimental data obtained with a Conf. α device is shown (similar results are valid also for Conf. β). The threshold imposed to obtain the set shown in the histogram generates five singular functions (on the total of 8); the other functions guarantee the completeness property of the set. In the best case, for the same number of writing processes, seven singular functions are obtained.

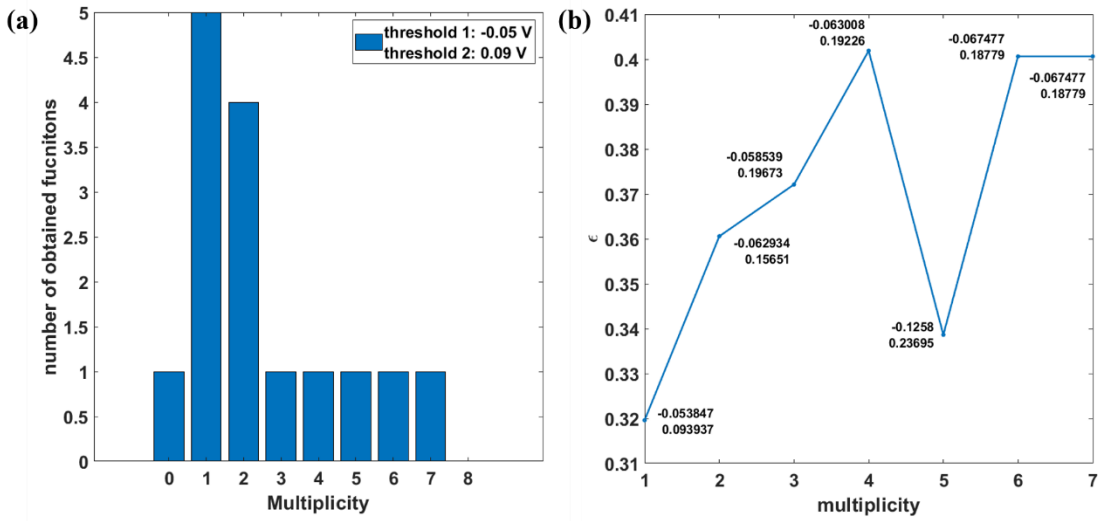

Figure 6-11 (a) Histogram representing the number of obtained functions after 100 writing processes, for a choice of the threshold (shown in the legend). The obtained set is complete. (b) Computed efficiency for several obtained set of functions with different thresholds. Each threshold-band (labels in the figure) maximize the number of functions with the multiplicity expressed on the x-axis.

From the sets of Boolean function obtained through the thresholding process, one can chose the complete sets to compute the efficiency of the device. Since the efficiency is dependent on the number of functions that appear in the set and on their multiplicity, I compute the efficiency on different sets obtained for different thresholds maximizing the number of functions with a given multiplicity. Figure 6-11 (b) shows that the efficiency varies in the range between 0.32 and 0.4. This gives us two important information: firstly, the efficiency of the device is robust against the choice of a particular threshold and a particular set; secondly, it depends upon the features of the complete set on which the computation is carried out. To summarize: a receptron produces a complete set of functions in a limited number of writings and, when these set does not cover the whole number of singular functions, the missing ones can be simply retrieved through a combination of the obtained functions.

Figure 6-12 shows how the efficiency evolves as function of the number of writing steps for Conf. α and Conf. β devices. The first eight writing steps give an efficiency equals to zero because a complete set is not generated. The efficiency has a value different form 0 when the explored outputs result in a complete function set. After each writing process, the same function can be generated several times: the process of writing is redundant. On one hand, this causes a higher number of writing steps to generate o complete set of functions, on the other one, the process is reliable and fault tolerant to variations of the environment.

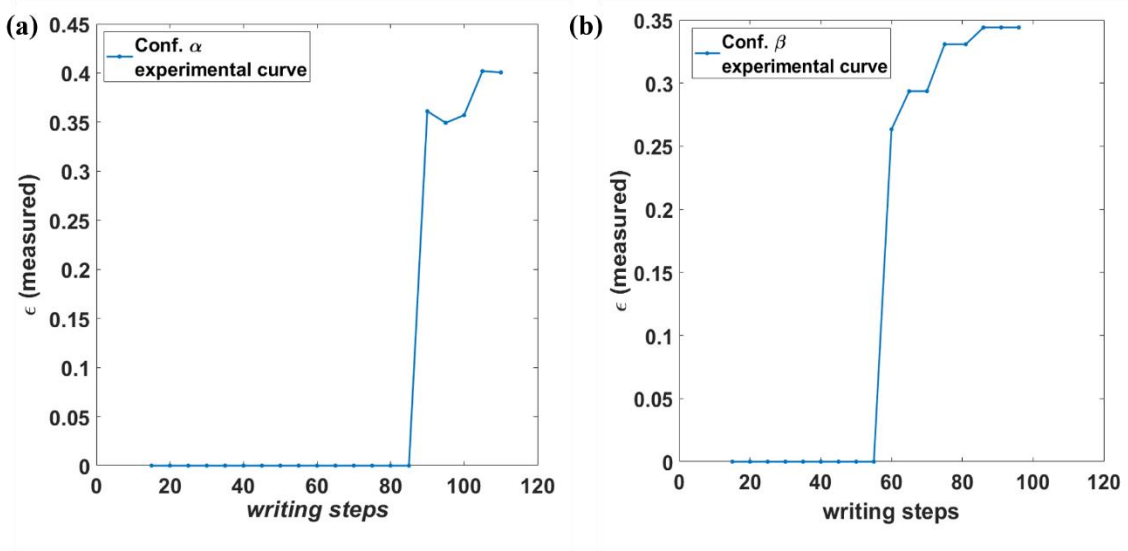

Figure 6-12 (a) Efficiency of the device as function of the number of writing process, for a Conf. α device. (b) Efficiency for a Conf. β sample.

The number of writings to reach a complete set of functions is different for the two configurations of the device. The lower degree of correlations in the Conf. α devices, require a higher number of writing processes with different input electrode configurations, to sample new functions. This lowers the rate of generation of new functions but allows to implement a broader set of weights. As result, a higher number of functions are sampled during the writing process and the maximum efficiency values are usually higher on this class of samples (Figure 6-12 (a)).

The maximum efficiency value is reached at a lower number of writings for the Conf. β device (Figure 6-12 (b)), where correlations among different couples of electrodes are higher. In this case, the spatial correlations ensure the implementation of a new set of weights after the writing process on several electrode configurations. Therefore, after each writing step the probability to sample a new function is high, increasing the rate of function generation.

6.6. Summary

In this chapter the model of the receptron, presented as a generalization of the perceptron, is proposed. The differences with the perceptron were outlined: the presence of input dependent weights and the consequences on the generation of a particular class of linear separable functions, the singular one. The results obtained by an experimental implementation of the receptron, exploiting the resistive switching properties of a multi-electrode cluster assembled gold film, are shown. The possibility to use the receptron as reconfigurable Boolean function generator is proposed and the possibility to implement also non-linear separable functions though a single device is experimentally proved.

In the last part of the chapter, a method to use receptron through a random training protocol is proposed and studied, both from simulation and experimental works. The approach guarantees the

possibility to obtain a complete device, build form a network of receptrons, that can implement all the Boolean functions with a fixed number of inputs. It was studied the reliability of the method and the fault tolerance against possible fabrication imperfections. In addition, the proposed method does not require a precise control of the evolution of the material employed to implement the weighting process and no supervision is needed. This opens new perspectives on the use of cluster-assembled films for reconfigurable devices and on the use of methods to exploit the response of materials to external stimuli to implement information processing systems.

7. Conclusions

In my thesis work I have fabricated and characterized cluster-assembled nanostructured gold films showing a non-ohmic electrical behaviour and complex and reproducible resistive switching. Nanostructured Au films have been fabricated by assembling bare gold clusters produced in the gas phase by supersonic cluster beam deposition.

The results of my work show that metallic nanogranular materials have functional properties radically different from their bulk counterparts. The electric conduction properties of cluster-assembled gold, with thickness beyond the percolation threshold, are deeply affected by their nanocrystalline complex structure, characterized by both very high density of grain boundaries and crystalline orientation mismatch. The circulation of electric current, under the application of an external electrical field, causes inter-cluster and intra-cluster rearrangements with the consequent dynamical creation and destruction of pathways, resulting in resistive switching. The electrical behaviour is characterized by the recurrent exploration of several resistance states.

The nanogranular structure of the Au films does not evolve with their thickness: this introduces a huge number of defects and junctions affecting the electrical transport for a wide range of thickness values beyond the percolation threshold.

The quantitatively characterization of the resistive switching and the electrical spiking activity shows that the electrical behaviour is influenced by the initial resistance of the cluster assembled films and that stable and reproducible features in terms of potentiation and reversible transition from low resistance to high resistance states are present. The electrical activity and the irregular bunches of spikes caused by resistive switching events show power law trend and $\frac{1}{f}$ scaling behaviour in the range of analysed frequencies. This corresponds to the emergence of temporal correlations in resistance switching activity over time, similar to those studied in the spiking activity of biological neural network.

I have also shown the possibility of fabricating a device made of a generic pattern of electrodes interconnected by a cluster-assembled Au film. Correlations emerge among the electrical activity of different regions of the film under the application of an external electrical stimulus higher than a certain threshold. The degree of correlation can be varied controlling the film geometry and the electrode configuration used to inject a current.

The fabrication of a Boolean function generator based on this multielectrode device was shown by exploiting the resistive switching activity of nanostructured gold film to implement an autonomous weight process of the input signals, triggered by external electrical pulses. This allows to reconfigure the system to recognize the input pattern of interest and generate a complete set of Boolean function.

The resistive switching properties and the device architecture results in an efficient reconfiguration processes and the generation of a broad set of function that can be used to obtain the classification of the received input signals, avoiding time consuming training processes, like backpropagation.

The spontaneous emerging of resistive switching activity in self-assembled systems avoids the complicate integration of a high number of single electronic components typical of CMOS technology. The simplicity of fabrication process enables the design of low-cost and scalable devices.

The approach developed in the work for the fabrication of a Boolean function generator for classification tasks opens interesting perspectives on the use of materials with intrinsic computational properties for the development of an artificial intelligence no longer based on the Turing paradigm.

Appendix A. Anomalous Electrical Conduction and Negative Temperature Coefficient of Resistance in Nanostructured Gold Resistive Switching Films

Introduction

Granular metallic films (GMFs) consist of random networks of metal clusters or nanoparticles, with different size and structure, separated by a dielectric matrix (either vacuum or a non-conducting material) [178,188,227]. The electrical properties of GMFs are strongly dependent on the coupling between adjacent metallic units and the transition from non-metallic transport to metallic conduction has been actively studied by varying their density from very diluted (weak-coupling regime) to particle structural percolation (strong-coupling regime) [172,186–188,208,228,229]. Systems in weak-coupling regime have received particular attention in order to understand the role of defects and discontinuities in determining the non-metallic behavior, whereas systems in strong-coupling regime are reported to be ohmic with conventional transport mechanisms typical of polycrystalline metallic films [179,183,185,230].

Random networks of metallic nanowires/nanoparticles in a polymeric matrix or passivated by shell of ligands or oxide layers have gained a renewed interest for the fabrication of non-linear circuital elements such as memristors and resistive switching devices for analog computing and neuromorphic data processing [34,104,114,157,231]. These systems are in the weak-coupling regime and their electrical behavior is determined by the formation/destruction of conducting junctions between isolated nanoparticles conferring neuromorphic properties to the networks [18,104,105,114,116,157,231].

Recently we showed that granular systems in strong-coupling regime consisting of continuous cluster-assembled gold films produced by the assembling of unprotected clusters, also show resistive switching[109,110]. Their structure is characterized by the random stacking of differently shaped crystalline clusters directly connected by junctions of different cross sections with an extremely high number of defects and grain boundaries [109,110].

Here we report that continuous cluster-assembled gold films, although in strong-coupling regime, show non-metallic electrical conduction and negative Temperature Coefficient of Resistance (TCR) within 24-300 K temperature range. The observed behavior indicates that conduction mechanisms typical of insulators or highly disordered semiconductors are occurring. Remarkably, the resistive switching activity of these systems is maintained down to cryogenic temperatures.

Experimental methods and characterization

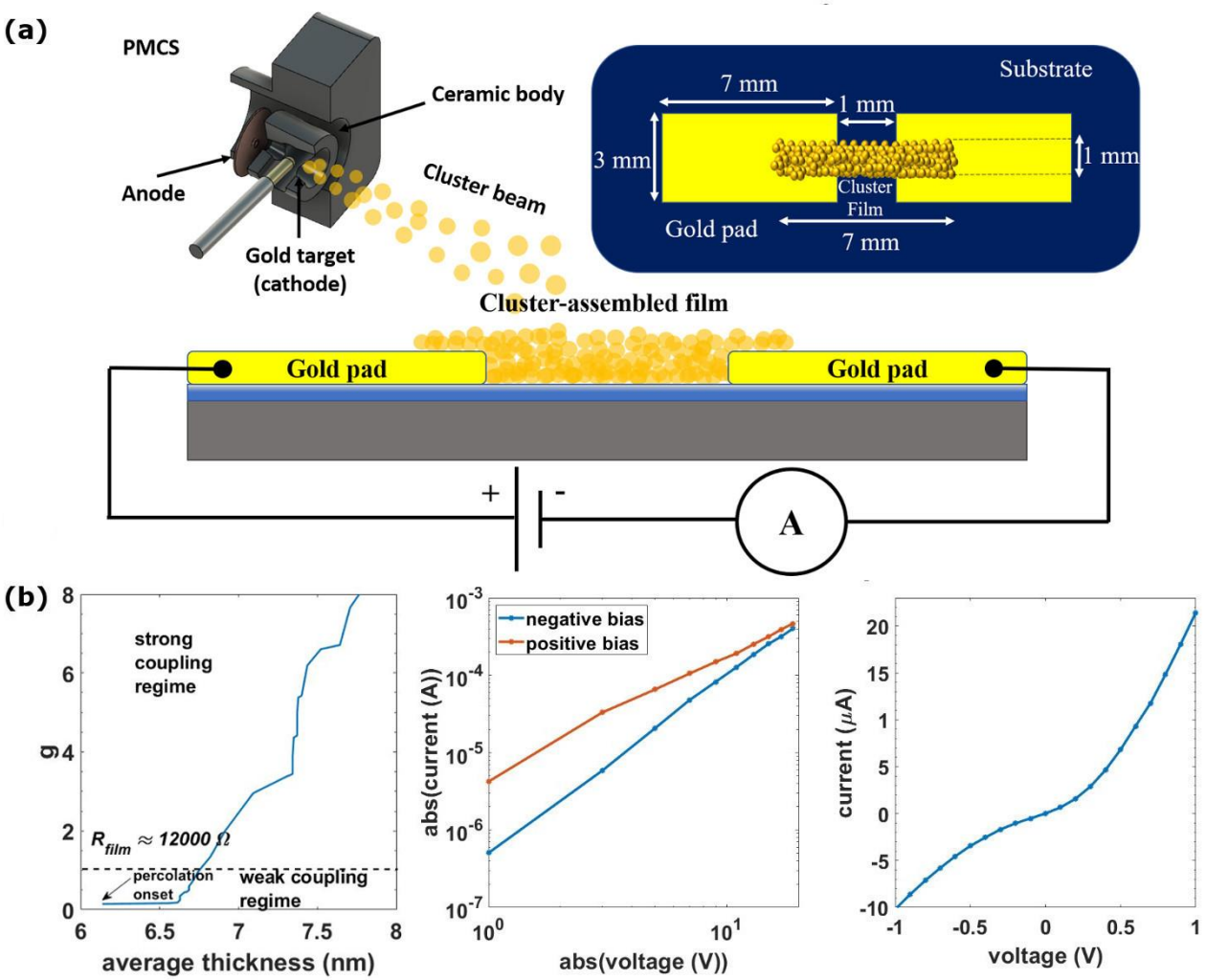

Figure 0-1 (a) Schematic view (not to scale) of a two-terminal device constituted by thermally deposited gold electrodes bridged by a cluster-assembled gold film. The blue region beneath the gold films is a silicon oxide layer. Electrical characterization is performed with an ammeter connected in series to a voltage source at room temperature. On the top left, a scheme (not to scale) of the cluster source (PMCS) used to generate the supersonic cluster beams. On the top right, a scheme with the device dimensions. The gold pads have a rectangular shape 7 mm x 3 mm, spaced by 1 mm and bridged by a 1 mm x 7 mm cluster film. The gold pads are 100 nm thick. (b) Left panel: evolution of the dimensionless tunnel conductance g after the percolation threshold, as function of the thickness of the film. Central panel: I-V curves in double logarithmic scale measured at RT. Red curve under positive bias, the blue one under negative bias. Right panel: I-V curve for voltage in the range -1 V to 1 V.

Nanostructured Au films were produced by a supersonic cluster beam deposition apparatus equipped with a Pulsed Microplasma Cluster Source (PMCS) [126], as described in detail in reference [110]. Figure 0-1a shows a schematic view of the Au cluster formation and deposition process. Au clusters with a bimodal log-normal mass distribution peaked around 5 nm are formed in an Argon

atmosphere after the plasma ablation of a gold target [110,232]; the cluster-Argon mixture is then expanded into the vacuum to form a supersonic beam directed on a silicon substrate with a thermally grown oxide layer [109,110]. Clusters are deposited between two gold electrodes previously fabricated by thermal evaporation (Figure 0-1a). Supersonic cluster beams are characterized by high collimation: this guarantees the patterning of films with a high lateral resolution by using stencil masks, as described in [110,195]. The amount of deposited material is measured by a pre-calibrated quartz microbalance, the evolution of the electrical resistance of the films is monitored *in situ* and *ex situ* in a two-probe configuration.

In situ electrical characterization in a range from room temperature (RT, 300 K) down to 24 K has been performed in vacuum (10^{-5} mbar) on films mounted on a copper cold finger of a helium mechanical cryocooler. The film overall features have been investigated by high resolution TEM (HRTEM), using a spherical aberration-corrected microscope with an ultimate point resolution of 0.07 nm [233].

We characterized continuous films with an average thickness ranging from 15 nm to 30 nm, and resistance, before switching activation [105,109,110], varying from 80 Ω to 1000 Ω. This range belongs to strong-coupling regime where ohmic behavior and positive TCR are usually observed in granular films [185,188,197]. The value of the dimensionless tunnel conductance $g = h/2e^2R_t(T \to \infty)$, where $R_t(T \to \infty)$ is the average tunnel resistance of the granular system at high temperature, discriminates the weak-coupling regime ($g < 1$) from the strong-coupling one ($g > 1$) [187,188]. In Figure 0-1-b (left panel) we show the evolution of g, obtained by approximating R_t to the resistance at room temperature, after the onset of percolation threshold, as function of the cluster-assembled film thickness [110]. The fast increase of g is due to the high rate of deposition and the formation of connections among the clusters that open new conductive paths. Figure 1b shows the transition to the strong-coupling regime at a thickness value of roughly 7 nm.

Figure 0-1b (central panel) shows the room temperature I-V characteristics of the cluster-assembled film under positive and negative bias voltage in double logarithmic scale. A clear departure from an ohmic behavior is evident, with an asymmetry under positive and negative bias (red and blue curve respectively). The slope change observed in the curves is caused by the presence of switching events during the application of the voltage ramp [109,110]. The coexistence of non-ohmic behavior with switching events in Au cluster assembled-films has been reported and discussed in [109]. Figure 0-1b (right panel) shows the room temperature I-V curve in linear scale for small applied voltages (values in the range -1 V to 1 V). Also in this case, the trend deviates form that expected for an ohmic conduction.

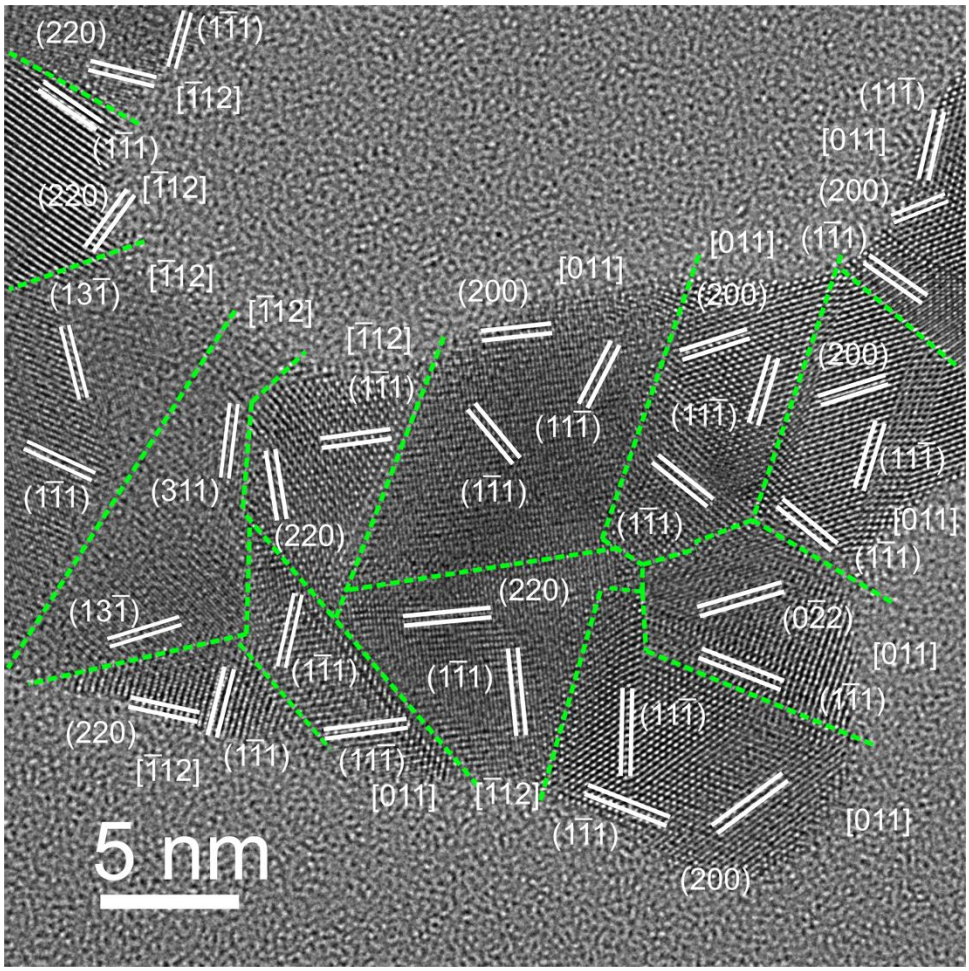

Figure 0-2 HRTEM image of a typical region of the film, in sub-monolayer regime. Different crystal domains constituting the film are separated by grain boundaries. For each single crystal domain, characteristic interplanar distances (hkl) and the corresponding zone axis [hkl] are displayed, after determination by local 2D-Fourier analysis of the relevant region of interest in the HRTEM image. The films clearly show an overall structure constituted by gold crystal domains, concomitantly allowing to rule out the presence of ordered phases other than metallic gold.

HRTEM analysis highlights the typical features at of the film from a structural point of view (Figure 2), namely its nanocrystalline, disordered nature. We characterized a film closed to percolation threshold, structural analysis performed by 2-Dimensional Fast Fourier Transform (2D-FFT) indicates that multiple, distinct crystal domains are formed, and their boundaries within the film are outlined by dashed lines. The size and shape of the domains are highly irregular and characterized by the presence of defects and with the smaller domains being less than 5 nm wide.

Results and Discussion

It is usually assumed that the electrical conduction properties of granular films in the strong-coupling regime are analogous to those of polycrystalline metallic films [187,234]. The observed

departure from an ohmic behavior at room temperature in continuous films resulting from the stacking of naked highly defective gold nanocrystals is unexpected. Our data suggest that different conduction mechanisms are taking place, dictated by the extremely high density of randomly oriented crystalline nanodomains and grain boundaries of the films (Figure 0-2).

In the case of two-terminal devices based on semiconductor or insulating layers, information on the microscopic mechanisms determining the current-voltage characteristics can be extracted by considering the parameter $\gamma = \frac{d\ln(I)}{d\ln(V)}$, where $\ln(I)$ and $\ln(V)$ are the logarithms of the current and of the applied voltage, respectively [235,236]. The analysis is carried out by plotting γ against $V^{\frac{1}{2}}$, since this curve has a well-defined trend for different mechanisms such as ohmic, space charge limited conduction (SCLC), Schottky, Poole-Frenkel, tunnelling, etc. [188,235].

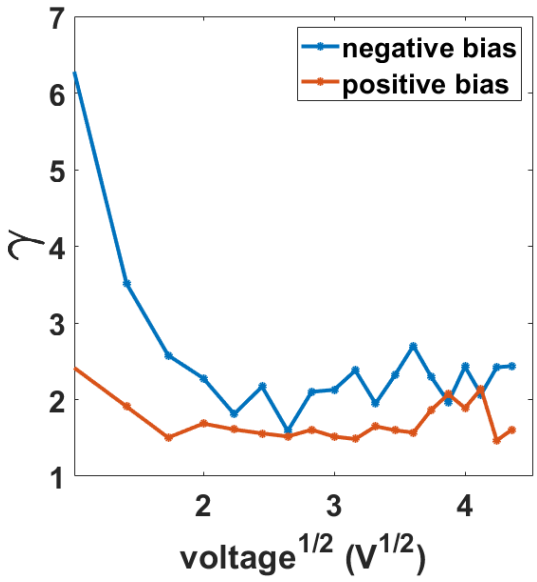

Figure 0-3: γ vs. the voltage square root for the increasing and the decreasing voltage branches of the I-V curve of a 15 nm thick cluster-assembled film.

The trend of the gamma parameter for our films is reported in Figure 0-3 showing a transient (blue curve) before stabilizing around roughly 2, which is typical of SCLC [235,237,238]. In this regime, the free carrier density is low and the electrical conduction is usually determined by the charges injected from ohmic electrodes [235].

In order to exclude the contribution of contact resistance, we tested atom-assembled thin films with similar thickness and geometry at RT. We found the standard ohmic behavior [110]. We can also exclude a contribution of the contact resistance at low temperatures since we did not observe a Schottky conduction contribution in the gamma curves, as one expects from contact resistance [239].

In systems characterized by SCLC, ohmic conduction is usually observed at low bias voltages, due to the presence of a small fraction of thermally generated carriers [237]. Cluster-assembled gold films show a non-linear I-V curve even at very low voltages (Fig 1b left panel) suggesting that different concurrent mechanisms contribute to determine a SCLC regime and to lower the free electron density. Coulomb blockade [186,240] and defect localization effects [183,188,241] could be possible causes for the low concentration of free carriers in our systems, due to their overall disordered crystal structure [], which manifests as a very high density of grain boundaries as observed by HRTEM (Figure 0-2).

To gain a deeper insight about the phenomena involved in the conduction process of cluster-assembled Au films and to discern among different mechanisms, we investigated the evolution of electrical conduction with temperature [171,186,242].

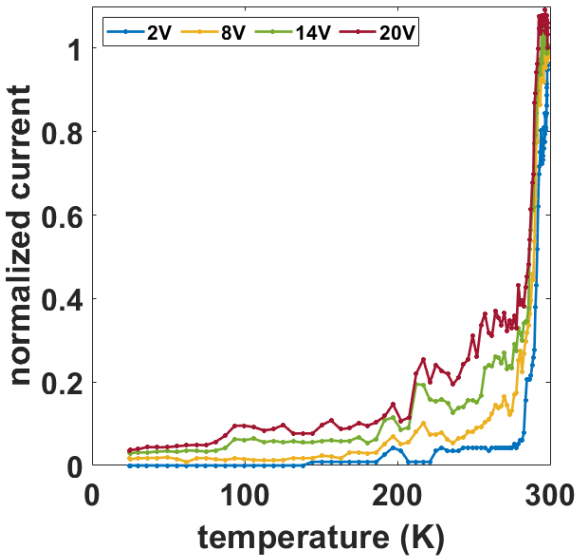

Figure 0-4 Current normalized to the value measured at RT as function of temperature for different applied voltages of a 25 nm thick sample. The sawtooth-like shape of curves at high voltages is due to switching events.

Figure 0-4 shows the temperature dependence of the current at different applied voltages normalized to the value measured at RT. We observe a steep decrease of the current in the range between RT and 250 K; from 250 K to 24 K the decrease continues with a lower slope. The trend of the current for different applied voltages is qualitatively similar.

In metallic systems, finite electrical resistivity arises due to scattering processes from impurities or various thermal excitations [134,136,178,243]. The scattering events can be considered

as statistically independent and thus additive, leading to the Matthiessen's rule, where any thermally induced scattering simply increases the resistivity ρ(T) [181,244]. This corresponds to a positive Temperature Coefficient of Resistivity (TCR), i.e. dρ/dT > 0. Figure 4 clearly show that cluster-assembled gold films are characterized by a trend of resistance with temperature typical of non-metallic systems.

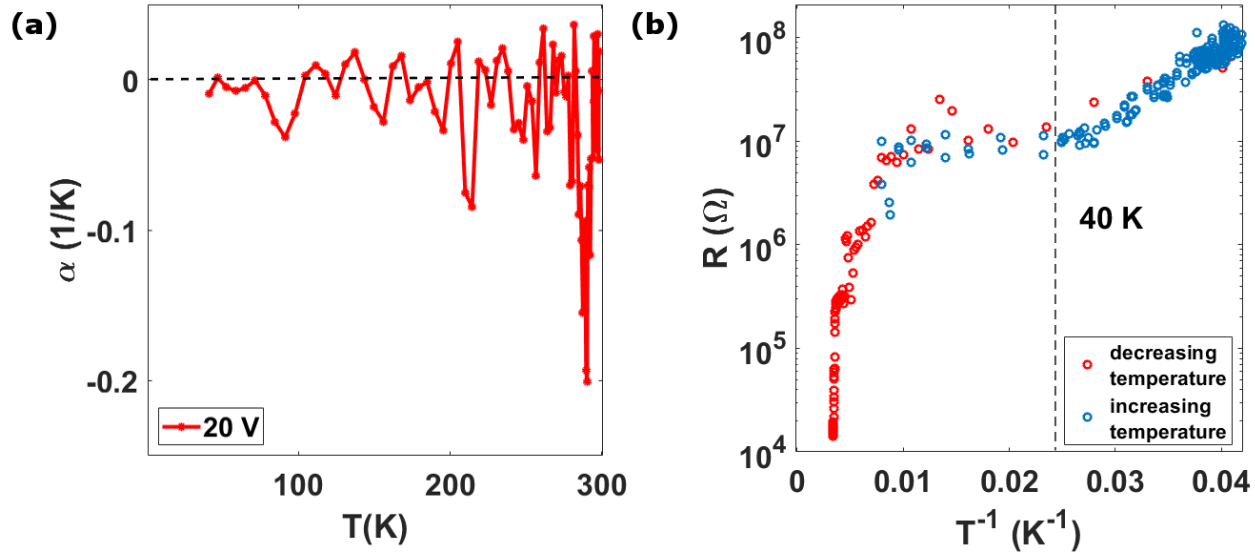

Figure 0-5: Data of a 25 nm thick cluster-assembled film. (a) the temperature coefficient of resistivity (TCR) for the curve measured upon the application of 20 V. (b) Resistance as a function of the inverse of the temperature, both for cooling (square point) and heating (cross) cycles, in logarithmic scale. An Arrhenius-like trend is recognizable only for temperatures below 40 K.

Figure 0-5a shows that cluster-assembled gold films have a negative TCR, in particular near RT, the oscillation around zero at lower temperatures can be ascribed to the presence of switching events of amplitude smaller than the resistance temperature variations [109,110].

These results are unexpected for a nanostructured metallic film in the strong-coupling regime: to the best of our knowledge only discontinuous gold ultrathin films and layers of molecularly linked gold nanoparticles have been reported to show non-metallic electrical conduction with temperature [172,179,187,197], although not in such a large temperature range. Self-assembled films of CnS2-linked Au nanoparticles have electrical properties ranging from insulating to metallic-like depending on the separation of the Au building blocks [230]. In the insulating regime, electric transport occurs through cooperative electron tunneling (co-tunneling) at low temperatures, variable-range hopping (VRH) at intermediate temperatures, and Arrhenius-type behavior at high temperatures [241]. The weight of each of these contributions depends on both the interparticle separation and the spatial organization.

Similarly, discontinuous films composed by irregularly shaped gold islands, assembled by atom deposition, with density close to the percolation threshold [185,187] show non-metallic transport strongly influenced by local disorder causing variations in the tunnel junction gaps and in the Coulomb blockade energies, due to island size fluctuations and offset charges [245]. A conduction percolation (co-percolation) model is applied to determine the total electrical current through the film as a function of both temperature and bias voltage [186]. The flowing of current is described as a percolation process through the ramified metallic islands. Unlike the case of hopping regime, in this case the high degree of disorder is related to the wide distribution, without mutual correlation, of the island electrostatic charging energy and of the parameters that characterize different tunnel junctions [186,187]. Increasing the island density till the reaching of strong-coupling regime, an ohmic electric transport is observed [186,187,197].

Various types of disorder are considered at the origin of a negative TCR in ultrathin discontinuous films: I) variations in the tunnel gaps between adjacent islands; II) variations in the size and shape of the islands; III) random offset induced by trapped impurity charges in the substrate [181,186]. In our case, cluster-assembled films are continuous and in the strong-coupling regime, however they do not show the electrical behavior typical of continuous metallic films. We suggest that this is due the extremely high concentration of defects and grain boundaries slicing the crystal domains that constitute the films: upon deposition on the substrates, gold clusters formed in the gas phase do not lose their individuality and give rise to the multidomain structure, as confirmed by HRTEM analysis [109] (see Figure 0-2). This kind of spatially extended disorder is substantially different from what observed in polycrystalline metallic films grown by atom deposition, where the density of grain boundaries is much lower compared to that we find in our systems [141].

Figure 0-5b displays the resistance vs the inverse of the temperature in logarithmic scale, showing that an Arrhenius-like behavior, characterized by a relation $R(T) \propto \exp\left(\frac{T_0}{T}\right)$, is not detected except for temperatures below 40 K. The observed behavior deviates from a pure hopping conduction like that in the Efros-Shklovskii model [186,188,246] for discontinuous films. On the other hand, the co-percolation model successfully describes the non-Arrhenius behavior of the electrical resistance at low bias voltage [186,187], even if different mechanisms, such as Anderson localization, could contribute to the overall electrical behavior observed [182,241]. We also note that the trend is reversible, i.e. the resistance curve obtained during the cooling coincides well with that obtained during the heating, strongly suggesting that the observed behavior is not related to a phase transition but only to electronic properties.

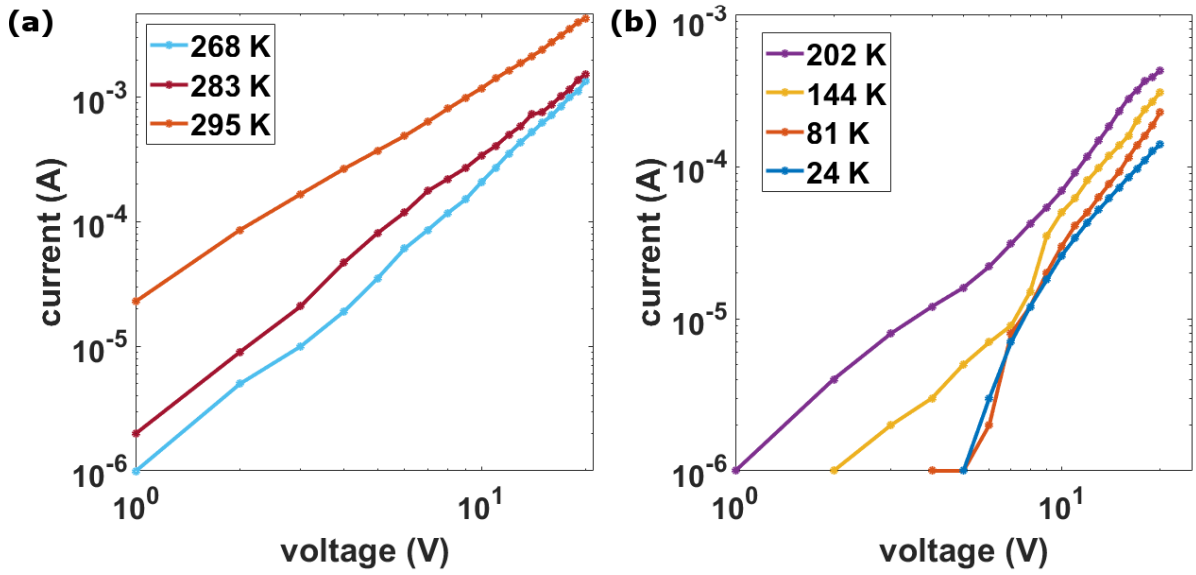

Figure 0-6: Data of a 25 nm thick cluster-assembled film. (a) I-V curves for different temperatures in the range 295 K to 268 K. (b) I-V curves in the range 202 K to 24 K.

The co-percolation model predicts not only the non-Arrhenius behavior but also a power law I-V characteristic (see Figure 0-1b). Figure 0-6a shows the I-V characteristics in the temperature range 295 K to 268 K. The trend is constantly linear in double logarithmic scale and unaffected by temperature change except for a higher resistance measured at lower temperatures. On the other hand, in Figure 0-6b the curves show steep slope variation for temperatures lower than 144 K. Although the trend slightly deviates from a pure power law, this agrees with the co-percolation model considering the occurrence of Coulomb blockade at cryogenic temperatures [186,240].

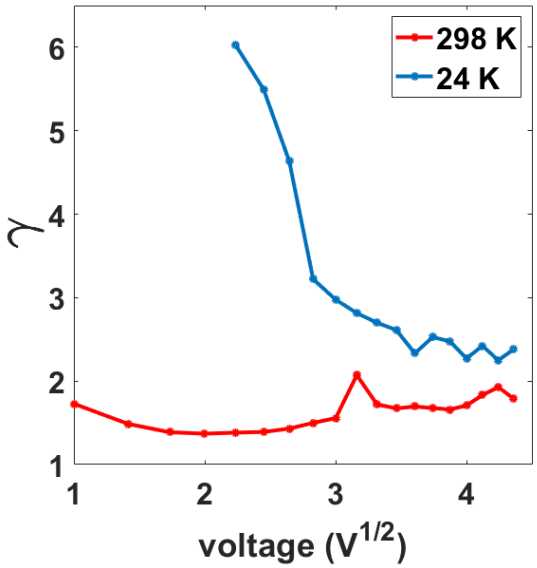

Figure 0-7: γ parameter as a function of the square root of the voltage of a 15 nm thick sample. The graph shows the evolution of γ for the positive branch in the I-V curve from 295 K to 24 K. At low voltages

(lower than 2 V) the current is suppressed; the curve shows the parameter values for voltage values greater than 2 V.

At low temperatures we also notice that the γ parameter explores values slightly larger than 2. Figure 0-7 shows the evolution of the γ parameter form 298 K to 24 K. This agrees with the observation of higher resistance states at low temperatures and indicates that the variation of thermally generated carriers is at the origin of the effects observed at low voltages. In addition, we underline that the resulting parameter γ is not compatible with a pure SCLC, but it reflects the dependence of the current by an external voltage in a medium with low density of free carriers and electrostatic phenomena hampering charge motion[186]. This further indicates the high density of defects and the disordered configuration can alter the electronic properties in the metallic film, reducing the mobility for the conduction electrons. The presence of grain boundaries and defects modify the electronic band structure of a metal[247] and its electrical conduction properties[181]. In our case the defect and grain boundaries densities are extremely high, compared to what observed in polycrystalline films[247] thus causing substantial electronic localization, the formation of space charge and hence the SCLC trend.

In order to provide further elements to highlight the role of the high density of grain boundaries and defect in determining the conduction regime, we have characterized the behavior of films under constant bias in the time. Since cluster-assembled gold films exhibit resistive switching (RS) phenomena[105,109,110], the evolution of the RS activity with temperature can provide useful elements.

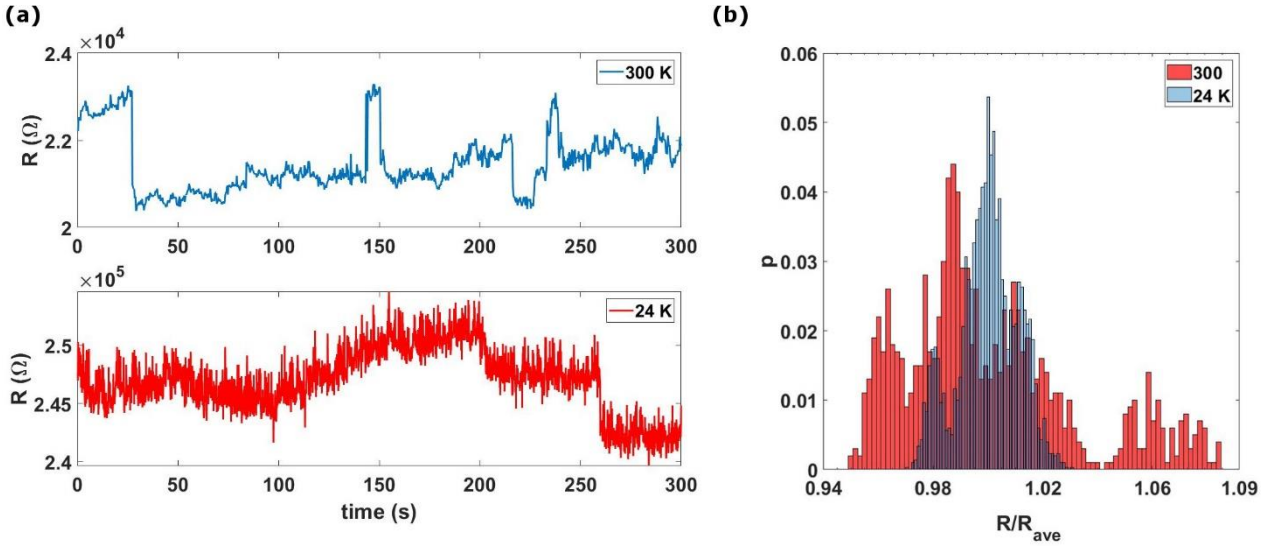

Figure 0-8: (a) The resistance-time graph, of a 15 nm thick sample, a300 K (blue curve) and at 24 k (red one). (b) Distribution of the resistance values normalized by their average for the measurements carried out at constant voltage (5 V) at RT (red data) and at 24 K (blue data).

In Figure 0-8-a we show a typical resistance-time graph of the evolution of the resistance under 5 V bias. We add the histogram (Figure 8-b) of the resistance, measured at both RT and 24 K upon the application of a constant voltage, for a duration of 300 s. The different peaks in the histogram are due to the different resistance levels explored during the resistive switching phenomena. Remarkably we observe a substantial RS activity at 24K spanning a lower number of levels compared to that at RT. We can interpret these results by considering that the flow of electric current causes the rearrangement of domains grown randomly with their related lattice defectivity and grain boundaries. As a consequence, concomitant dynamical creation and destruction of pathways with variable resistance occur through the rearrangement of defects [116,157]. This process is favored at RT by the high mobility of atoms and atomic planes [103], while the latter is reduced at cryogenic temperatures.

The persistence of RS events at cryogenic temperatures is unexpected and it could be related to the structure of cluster-assembled films characterized by a landscape crowded of defects and interconnects between grains resulting in an assembly of interacting nanojunctions [177,245,247]. Multiple conductance states are observed in single metallic nanojunctions at cryogenic temperatures [119,248] with electrical conductions characterized by discrete steps of conductance involving Coulomb blockade phenomena both in increasing and decreasing resistance [119,249]. Cluster-assembled gold films can be then considered as an assembly of nanojunctions connected in series and in parallel, thus displaying a collective electrical behavior resulting in resistive switching phenomena [109,116,142]. This confirms the facts that high densities of grain boundaries and nanojunctions can significantly alter the electronic properties, favoring the onset of non-ohmic conduction mechanisms. Atomic rearrangement present under the application of high voltage bias contributes to the rearrangement of grain boundaries responsible for the switching events. The observed mechanism is substantially different from what observed in random networks of nanowires where ionic transport is involved [34,104,114,231,250]. In our case the highly correlated re-arrangement of grain boundaries changes the local conductivity as observed in single metallic nanowires [173].

Conclusions

In summary, cluster-assembled continuous Au films in strong-coupling regime exhibit a non-metallic electrical conduction and a negative TCR over a range from RT to cryogenic temperatures. Our data can be explained by considering the coexistence SCLC and Coulomb blockade phenomena, similarly to what observed in highly disordered semiconductor or insulator films. Of primary importance for the understanding of the microscopic mechanisms responsible for these puzzling

electrical properties is the influence of an extremely high density of grain boundaries and lattice defectivity on conduction electron localization.

Our results highlight that cluster-assembled gold films are a challenging platform for exploring the fundamental role of extended nanoscale defects on electron localization and transport mechanisms, and for the fabrication of resistive switching devices that can operate over a wide temperature range with interesting non-linear electrical properties which could be exploited for neuromorphic data processing [88,109,251]

Bibliography

[1] J. Von Neumann and M. D. Godfrey, “First Draft of a Report on the EDVAC” *IEEE Ann. Hist. Comput.*, **15**, 27 (1993)

[2] S. Ambrogio *et al.*, “Equivalent-accuracy accelerated neural-network training using analogue memory” *Nature*, **558**, 60 (2018)

[3] J. P. Crutchfield, W. L. Ditto, and S. Sinha, “Introduction to focus issue: Intrinsic and designed computation: Information processing in dynamical systems-beyond the digital hegemony” *Chaos*, **20**, 037101 (2010)

[4] H. Jaeger, “Exploring the landscapes of ‘computing’: digital, neuromorphic, unconventional -- and beyond” 1 (2020)[Online]. Available: http://arxiv.org/abs/2011.12013

[5] F. Hadaeghi, X. He, and H. Jaeger, “Unconventional Information Processing Systems, Novel Hardware: A Tour d’Horizon” , (2017). [Online]. Available: https://opus.jacobs-university.de/frontdoor/index/index/docId/749

[6] G. W. Burr *et al.*, “Neuromorphic computing using non-volatile memory” *Adv. Phys. X*, **2**, 89 (2017)

[7] D. Seok Jeong, I. Kim, M. Ziegler, and H. Kohlstedt, “Towards artificial neurons and synapses: A materials point of view” *RSC Adv.*, **3**, 3169 (2013)

[8] A. I. Berg *et al.*, “Synaptic and neuromorphic functions: General discussion” *Faraday Discuss.*, **213**, 553 (2019)

[9] E. O. Neftci, “Data and Power Efficient Intelligence with Neuromorphic Learning Machines” *iScience*, **5**, 52 (2018)

[10] R. A. Nawrocki, R. M. Voyles, and S. E. Shaheen, “A Mini Review of Neuromorphic Architectures and Implementations” *IEEE Trans. Electron Devices*, **63**, 3819 (2016)

[11] A. Z. Stieg, A. V. Avizienis, H. O. Sillin, C. Martin-Olmos, M. Aono, and J. K. Gimzewski, “Emergent criticality in complex turing B-type atomic switch networks” *Adv. Mater.*, **24**, 286 (2012)

[12] A. Turing, “COMPUTING MACHINERY AND INTELLIGENCE” *Mind*, **49**, 433 (1950)

[13] K. P. Zauner, “From prescriptive programming of solid-state devices to orchestrated self-

organisation of informed matter" *Lect. Notes Comput. Sci.*, **3566**, 47 (2005)

[14] M. Mohid, J. F. Miller, S. L. Harding, G. Tufte, M. K. Massey, and M. C. Petty, "Evolution-in-materio: solving computational problems using carbon nanotube–polymer composites" *Soft Comput.*, **20**, 3007 (2016)

[15] M. Dale, S. Stepney, J. F. Miller, and M. Trefzer, "Reservoir computing in materio: An evaluation of configuration through evolution" *2016 IEEE Symp. Ser. Comput. Intell. SSCI 2016*, (2017)

[16] M. Di Ventra and F. L. Traversa, "Memcomputing: Leveraging memory and physics to compute efficiently" *J. Appl. Phys.*, **123**, 180901 (2018)

[17] H. O. Sillin *et al.*, "A theoretical and experimental study of neuromorphic atomic switch networks for reservoir computing" *Nanotechnology*, **24**, 384004 (2013)

[18] A. Diaz-Alvarez *et al.*, "Emergent dynamics of neuromorphic nanowire networks" *Sci. Rep.*, **9**, 1 (2019)

[19] E. J. Sandouk *et al.*, "Multistate resistive switching in silver nanoparticle films Multistate resistive switching in silver nanoparticle fi lms" *Sci. Technol. Adv. Mater.*, **16**, 45004 (2015)

[20] J. E. Savage, *Models of Computations*. Addison-Wesley, 1998

[21] A. S. Tanenbaum and T. Austin, *Structured Computer Organization*, Sixth Ed. PEARSON, 2013

[22] P. Horowitz and W. Hill, *The art of electronics*, Third Ed. CAMBRIDGE University Press, 2015

[23] S. Borkar, "Electronics beyond nano-scale CMOS" , in *Proceedings of the 43rd annual Design Automation Conference*, 2006, 807

[24] B. Nikolić, "Simpler, more efficient design" , in *European Solid-State Circuits Conference*, 2015, 20

[25] M. M. Waldrop, "More than moore" *Nature*, **530**, 145 (2016)

[26] J. Backus, "Can Programming Be Liberated from the von Neumann Style? A Functional Style and Its Algebra of Programs" *Commun. ACM*, **21**, 613 (1978)

[27] Z. Wang, S. Ambrogio, S. Balatti, and D. Ielmini, "A 2-transistor/1-resistor artificial synapse capable of communication and stochastic learning in neuromorphic systems" *Front.*

Neurosci., **9**, 1 (2015)

[28] D. Ielmini and H. S. P. Wong, "In-memory computing with resistive switching devices" *Nat. Electron.*, **1**, 333 (2018)

[29] G. Indiveri *et al.*, "Neuromorphic silicon neuron circuits" *Front. Neurosci.*, **5**, 1 (2011)

[30] E. Chicca, F. Stefanini, C. Bartolozzi, and G. Indiveri, "Neuromorphic electronic circuits for building autonomous cognitive systems" *Proc. IEEE*, **102**, 1367 (2014)

[31] C. Mead, "Neuromorphic Electronic Systems" *Proc. IEEE*, **78**, 1629 (1990)

[32] D. Kuzum, S. Yu, and H. S. Philip Wong, "Synaptic electronics: Materials, devices and applications" *Nanotechnology*, **24**, 382001 (2013)

[33] M. Ziegler, C. Wenger, E. Chicca, and H. Kohlstedt, "Tutorial: Concepts for closely mimicking biological learning with memristive devices: Principles to emulate cellular forms of learning" *J. Appl. Phys.*, **124**, 152003 (2018)

[34] G. Milano *et al.*, "Brain-Inspired Structural Plasticity through Reweighting and Rewiring in Multi-Terminal Self-Organizing Memristive Nanowire Networks" *Adv. Intell. Syst.*, **2**, 2000096 (2020)

[35] G. Indiveri and S. C. Liu, "Memory and Information Processing in Neuromorphic Systems" *Proc. IEEE*, **103**, 1379 (2015)

[36] E. R. Kandel, J. H. Schwartz, and T. M. Jessell, *Principles of Neural Science*, 4th ed. McGraw-Hill, 2000

[37] A. Mazzoni, F. D. Broccard, E. Garcia-Perez, P. Bonifazi, M. E. Ruaro, and V. Torre, "On the dynamics of the spontaneous activity in neuronal networks" *PLoS One*, **2**, e439 (2007)

[38] D. O. Hebb, *Organization of Behavior*. Psychology Press Edition, 1949

[39] E. M. Izhikevich, "Simple model of spiking neurons" *IEEE Trans. Neural Networks*, **14**, 1569 (2003)

[40] R. Quian Quiroga and S. Panzeri, "Extracting information from neuronal populations: Information theory and decoding approaches" *Nat. Rev. Neurosci.*, **10**, 173 (2009)

[41] D. Lonardoni, H. Amin, S. Di Marco, A. Maccione, L. Berdondini, and T. Nieus, "Recurrently connected and localized neuronal communities initiate coordinated spontaneous activity in neuronal networks" *PLoS Comput. Biol.*, **13**, 1 (2017)

[42] J. M. Beggs and D. Plenz, “Neuronal Avalanches in Neocortical Circuits” *J. Neurosci.*, **23**, 11167 (2003)

[43] L. De Arcangelis and H. J. Herrmann, “Learning as a phenomenon occurring in a critical state” *Proc. Natl. Acad. Sci. U. S. A.*, **107**, 3977 (2010)

[44] T. E. Harris, “The theory of branching processes” , New York, Dover, (1989)

[45] V. Frette, K. Christensen, A. Malthe-Sorensen, J. Feder, T. Jossang, and P. Meakin, “Avalanche dynamics in a pile of rice” *Nature*, **379**, 49 (1996)

[46] M. Karsai, K. Kaski, A. L. Barabási, and J. Kertész, “Universal features of correlated bursty behaviour” *Sci. Rep.*, **2**, 1 (2012)

[47] P. Bak and M. Paczuski, “Complexity, contingency, and criticality” *Proc. Natl. Acad. Sci. U. S. A.*, **92**, 6689 (1995)

[48] A. Levina, J. M. Herrmann, and T. Geisel, “Dynamical synapses causing self-organized criticality in neural networks” *Nat. Phys.*, **3**, 857 (2007)

[49] C. Bédard, H. Kröger, and A. Destexhe, “Does the 1/f frequency scaling of brain signals reflect self-organized critical states?” *Phys. Rev. Lett.*, **97**, 1 (2006)

[50] K. Klemm, S. Bornholdt, and H. G. Schuster, “Beyond hebb: Exclusive-OR and biological learning” *Phys. Rev. Lett.*, **84**, 3013 (2000)

[51] G. Tononi, G. M. Edelman, and O. Sporns, “Complexity and coherency: Integrating information in the brain” *Trends Cogn. Sci.*, **2**, 474 (1998)

[52] E. Bullmore and O. Sporns, “Complex brain networks: Graph theoretical analysis of structural and functional systems” *Nat. Rev. Neurosci.*, **10**, 186 (2009)

[53] J. M. Shine and R. A. Poldrack, “Principles of dynamic network reconfiguration across diverse brain states” *Neuroimage*, **180**, 396 (2018)

[54] J. Von Neumann, “Probabilistic Logics and the Synthesis of Reliable Organisms Form Unreliable Components” *Autom. Stud.*, **34**, 43 (1956)

[55] A. M. Turing, “Solvable and Unsolvable Problems” *Sci. News*, **34**, 3 (1954)

[56] G. N. Reeke and G. M. Edelman, “Real Brains and Artificial Intelligence” *Dedalus*, **117**, 143 (1988)[Online]. Available: https://www.jstor.org/stable/20025142

[57] C. Teuscher, “Unconventional Computing Catechism” *Front. Robot. AI,* **1**, 1 (2014)

[58] M. E. Csete and J. C. Doyle, “Reverse engineering of biological complexity” *Science (80-.).*, **295**, 1664 (2002)

[59] D. J. C. MacKay, *Information Theory, Inference and Learning Algorithms*. CAMBRIDGE University Press, 2005

[60] F. Rosenblatt, “The perceptron: A probabilistic model for information storage and organization in the brain” *Psychol. Rev.*, **65**, 386 (1958)

[61] M. Minsky and S. Papert, *Perceptrons, An Introduction to Computational Geometry*. 1969

[62] W. Pitts and W. S. McCulloch, “How we know universals the perception of auditory and visual forms” *Bull. Math. Biophys.*, **9**, 127 (1947)

[63] F. Alibart, E. Zamanidoost, and D. B. Strukov, “Pattern classification by memristive crossbar circuits using ex situ and in situ training” *Nat. Commun.*, **4**, 1 (2013)

[64] T. Chen *et al.*, “Classification with a disordered dopant- atom network in silicon” *Nature*, **577**, 341 (2020)

[65] H. Jaeger, “Tutorial on training recurrent neural networks, covering BPPT, RTRL, EKF and the ‘echo state network’ approach.” *GMD Rep.*, **159**, 1 (2002)

[66] J. J. Hopfield, “Neural networks and physical systems with emergent collective computational abilities Biophysics : Hopfield I T ., V .” *Proc Natl Acad Sci USA*, **79**, 2554 (1982)

[67] G. E. Hinton and R. R. Salakhutdinov, “Reducing the Dimensionality of Data with Neural Networks” *Science (80-.).*, **313**, 504 (2006)

[68] Y. Lecun, Y. Bengio, and G. Hinton, “Deep learning” *Nature*, **521**, 436 (2015)

[69] H. Y. Xiong *et al.*, “The human splicing code reveals new insights into the genetic determinants of disease” *Science (80-.).*, **347**, (2015)

[70] G. Cybenko, “Approximation by Superpositions of a sigmoidal function” *Math. Control. SIgnals, Syst.*, **2**, 303 (1989)

[71] K. Hornik, “Approximation Capabilities of Multilayer Neural Network” *Neural Networks*, **4**, 251 (1991)

[72] D. E. Rumelhart, G. E. Hinton, and R. J. Williams, “Learning representations by back-propagating errors” *Nature*, **323**, 533 (1986)

[73] L. Chua, “Memristor-The Missing Circuit Element” *IEEE Trans. Circuits Theory*, **CT-18**, 507 (1971)

[74] L. O. Chua and S. M. Kang, “Memristive Devices and Systems” *Proc. IEEE*, **64**, 209 (1976)

[75] L. Chua, “Everything you wish to know about memristors but are afraid to ask” *Radioengineering*, **24**, 319 (2015)

[76] D. B. Strukov, G. S. Snider, D. R. Stewart, and R. S. Williams, “The missing memristor found” *Nat. Lett.*, **453**, 80 (2008)

[77] D. B. Strukov and H. Kohlstedt, “Resistive switching phenomena in thin films: Materials, devices, and applications” *MRS Bull.*, **37**, 108 (2012)

[78] T. Hasegawa *et al.*, “Learning abilities achieved by a single solid-state atomic switch” *Adv. Mater.*, **22**, 1831 (2010)

[79] T. H. Kim *et al.*, “Nanoparticle assemblies as memristors” *Nano Lett.*, **9**, 2229 (2009)

[80] N. DIederich, T. Bartsch, H. Kohlstedt, and M. Ziegler, “A memristive plasticity model of voltage-based STDP suitable for recurrent bidirectional neural networks in the hippocampus” *Sci. Rep.*, **8**, 1 (2018)

[81] E. Limpert, W. A. Stahel, and M. Abbt, “Log-normal Distributions across the Sciences: Keys and Clues” *Bioscience*, **51**, 341 (2001)

[82] M. Ernoult, J. Grollier, and D. Querlioz, “Using Memristors for Robust Local Learning of Hardware Restricted Boltzmann Machines” *Sci. Rep.*, **9**, 1 (2019)

[83] J. P. Crutchfield and K. Young, “Computation at the Onset of Chaos” , in *Complexity, Entropy, and Physics of Information*, 1989

[84] M. Dale, J. F. Miller, S. Stepney, and M. A. Trefzer, “A substrate-independent framework to characterise reservoir computers” *arXivProceedings Royl Soc. A*, **475**, 1 (2018)

[85] F. L. Traversa and M. Di Ventra, “Universal Memcomputing Machines” *IEEE Trans. Neural Networks Learn. Syst.*, **26**, 2702 (2015)

[86] D. Stauffer, “Scaling Theory of Percolation Clusters” *Phys. Rep.*, **54**, 1 (1979)

[87] S. Kirkpatrick, “Percolation and Conduction” *Rev. Mod. Phys.*, **54**, 574 (1973)

[88] G. Tanaka *et al.*, “Recent advances in physical reservoir computing: A review” *Neural Networks*, **115**, 100 (2019)

[89] W. Maass, “Noise as a resource for computation and learning in networks of spiking neurons” *Proc. IEEE*, **102**, 860 (2014)

[90] L. Buesing, J. Bill, B. Nessler, and W. Maass, “Neural dynamics as sampling: A model for stochastic computation in recurrent networks of spiking neurons” *PLoS Comput. Biol.*, **7**, (2011)

[91] H. Jaeger and H. Haas, “Harnessing Nonlinearity: Predicting Chaotic Systems and Saving Energy in Wireless Communication” *Science (80-.).*, **304**, 78 (2004)

[92] D. Sherrington and S. Kirkpatrick, “Solvable model of a spin-glass” *Phys. Rev. Lett.*, **35**, 1792 (1975)

[93] M. Al-Shedivat, R. Naous, G. Cauwenberghs, and K. N. Salama, “Memristors empower spiking neurons with stochasticity” *IEEE J. Emerg. Sel. Top. Circuits Syst.*, **5**, 242 (2015)

[94] W. Maass and H. Markram, “Real-Time Computing Without Stable States: A New Framework for Neural Computation Based on Perturbations” *Neural Comput.*, **14**, 2531 (2001)

[95] M. Lukosevicoius and H. Jaeger, “Reservoir computing approaches to recurrent neural network training” *Comput. Sci. Rev.*, **3**, 127 (2009)

[96] L. Larger, A. Baylón-Fuentes, R. Martinenghi, V. S. Udaltsov, Y. K. Chembo, and M. Jacquot, “High-speed photonic reservoir computing using a time-delay-based architecture: Million words per second classification” *Phys. Rev. X*, **7**, 1 (2017)

[97] Y. Yi *et al.*, “FPGA based spike-time dependent encoder and reservoir design in neuromorphic computing processors” *Microprocess. Microsyst.*, **46**, 175 (2016)

[98] C. Du, F. Cai, M. A. Zidan, W. Ma, S. H. Lee, and W. D. Lu, “Reservoir computing using dynamic memristors for temporal information processing” *Nat. Commun.*, **8**, 1 (2017)

[99] J. F. Miller, S. L. Harding, and G. Tufte, “Evolution-in-materio: Evolving computation in materials” *Evol. Intell.*, **7**, 49 (2014)

[100] A. Thompson, “An evolved circuit, intrinsic in silicon, entwined with physics” *Lect. Notes*

Comput. Sci. (including Subser. Lect. Notes Artif. Intell. Lect. Notes Bioinformatics), **1259**, 390 (1997)

[101] J. F. Miller, "The alchemy of computation: designing with the unknown" *Nat. Comput.*, **18**, 515 (2019)

[102] A. V. Avizienis *et al.*, "Neuromorphic atomic switch networks" *PLoS One*, **7**, 1 (2012)

[103] S. K. Bose, S. Shirai, J. B. Mallinson, and S. A. Brown, "Synaptic dynamics in complex self-assembled nanoparticle networks" *Faraday Discuss.*, **213**, 471 (2019)

[104] H. G. Manning *et al.*, "Emergence of winner-takes-all connectivity paths in random nanowire networks" *Nat. Commun.*, **9**, 1 (2018)

[105] C. Minnai, M. Mirigliano, S. A. Brown, and P. Milani, "The nanocoherer: An electrically and mechanically resettable resistive switching device based on gold clusters assembled on paper" *Nano Futur.*, **2**, 1 (2018)

[106] R. W. Siegel, "Nanophase materials assembled from atom clusters" *Mater. Sci. Eng. B*, **19**, 37 (1993)

[107] H. Gleiter, "Nanostructured Materials" *Adv. Mater.*, **4**, 474 (1992)

[108] A. Perez *et al.*, "Cluster assembled materials: A novel class of nanostructured solids with original structures and properties" *J. Phys. D. Appl. Phys.*, **30**, 709 (1997)

[109] M. Mirigliano *et al.*, "Complex electrical spiking activity in resistive switching nanostructured Au two-terminal devices" *Nanotechnology*, **31**, 234001 (2020)

[110] M. Mirigliano, F. Borghi, A. Podestà, A. Antidormi, L. Colombo, and P. Milani, "Non-ohmic behavior and resistive switching of Au cluster-assembled films beyond the percolation threshold" *Nanoscale Adv.*, **1**, 3119 (2019)

[111] K. S. Scharnhorst *et al.*, "Atomic switch networks as complex adaptive systems" *Jpn. J. Appl. Phys.*, **57**, 03ED02 (2018)

[112] A. P. Alivisatos, "Semiconductor CLsters, Nanocrsytals, and Quantum Dots" , *Science*, **271**, . 933 , 1996

[113] E. Roduner, "Size matters: Why nanomaterials are different" *Chem. Soc. Rev.*, **35**, 583 (2006)

[114] J. B. Mallinson, S. Shirai, S. K. Acharya, S. K. Bose, E. Galli, and S. A. Brown, "Avalanches

and criticality in self-organized nanoscale networks" *Sci. Adv.*, **5**, 1 (2019)

[115] A. Diaz-Alvarez, R. Higuchi, Q. Li, Y. Shingaya, and T. Nakayama, "Associative routing through neuromorphic nanowire networks" *AIP Adv.*, **10**, 025134 (2020)

[116] C. Minnai, A. Bellacicca, S. A. Brown, and P. Milani, "Facile fabrication of complex networks of memristive devices" *Sci. Rep.*, **7**, 1 (2017)

[117] A. Lassesson, S. A. Brown, J. Van Lith, and M. Schulze, "Electrical characterization of gold island films: A route to control of nanoparticle deposition" *Appl. Phys. Lett.*, **93**, 2 (2008)

[118] S. K. Bose, C. P. Lawrence, Z. Liu, K. S. Makarenko, R. M. J. Van Damme, and H. J. Broersma, "Evolution of a designless nanoparticle network into recon fi gurable Boolean logic" *Nat. Nanotechnol.*, **10**, 1048 (2015)

[119] R. Hoffman-Vogel, "Electromigration and the structure of metallic nanocontacts" *Appl. Phys. Rev.*, **4**, 031302 (2017)

[120] A. Halbritter *et al.*, "Connective neck evolution and conductance steps in hot point contacts" *Phys. Rev. B - Condens. Matter Mater. Phys.*, **65**, 454131 (2002)

[121] M. Mirigliano, S. Radice, A. Falqui, A. Casu, F. Cavaliere, and P. Milani, "Anomalous electrical conduction and negative temperature coefficient of resistance in nanostructured gold resistive switching films" *Sci. Rep.*, **10**, 1 (2020)

[122] P. Milani and S. Iannotta, *Cluster Beam Synthesis of Nanostructured Materials*. Springer, 1999

[123] H. Haberland, Z. Insepov, and M. Moseler, "Molecular-dynamics simulation of thin-film growth by energetic cluster impact" *Phys. Rev. B*, **51**, 11061 (1995)

[124] Y. Huttel, *Gas-Phase Synthesis of Nanoparticles*. Wiley-VCH, 2017

[125] R. Strobel and S. E. Pratsinis, "Flame aerosol synthesis of smart nanostructured materials" *J. Mater. Chem.*, **17**, 4743 (2007)

[126] K. Wegner, P. Piseri, H. V. Tafreshi, and P. Milani, "Cluster beam deposition: A tool for nanoscale science and technology" *J. Phys. D. Appl. Phys.*, **39**, R439 (2006)

[127] P. Piseri, H. V. Tafreshi, and P. Milani, "Manipulation of nanoparticles in supersonic beams for the production of nanostructured materials" *Curr. Opin. Solid State Mater. Sci.*, **8**, 195 (2004)

[128] R. E. Palmer, R. Cai, and J. Vernieres, “Synthesis without Solvents: The Cluster (Nanoparticle) Beam Route to Catalysts and Sensors” *Acc. Chem. Res.*, **51**, 2296 (2018)

[129] H. Haberland, M. Karrais, M. Mall, and Y. Thurner, “Thin films from energetic cluster impact: A feasibility study” *J. Vac. Sci. Technol. A Vacuum, Surfaces, Film.*, **10**, 3266 (1992)

[130] J. Kousal *et al.*, “Magnetron-sputtered copper nanoparticles: lost in gas aggregation and found by in situ X-ray scattering” *Nanoscale*, **10**, 18275 (2018)

[131] O. Lupan *et al.*, “PdO/PdO2 functionalized ZnO:::Pd films for lower operating temperature H2 gas sensing” *Nanoscale*, **10**, 14107 (2018)

[132] K. Fuchs, “The Conductivity of Thin Metallic Films According To The Electron Theory of Metals” *Math. Proc. Cambridge Philos. Soc.*, **34**, 100 (1937)

[133] E. H. Sondheimer, “The mean free path of electrons in metals” *Adv. Phys.*, **1**, 1 (1952)

[134] A. F. Mayadas and M. Shatzkes, “Electrical-resistivity model for polycrystalline films: the case of arbitrary reflection at external surfaces” *Phys. Rev. B*, **1**, 1382 (1970)

[135] D. Josell, S. H. Brongersma, and Z. Tokei, “Size-dependent resistivity in nanoscale interconnects” *Annu. Rev. Mater. Res.*, **39**, 231 (2009)

[136] J. Vancea, H. Hoffmann, and K. Kastner, “Mean Free Path and Effective Density of Conduction Electrons in Polycrystalline Metal Films” *Thin Solid Films*, **121**, 201 (1984)

[137] C. Durkan, M. A. Schneider, and M. E. Welland, “Analysis of failure mechanisms in electricallystressed Au nanowires” *J. Appl. Phys.*, **86**, 1280 (1999)

[138] W. Steinhögl, G. Schindler, G. Steinlesberger, M. Traving, and M. Engelhardt, “Comprehensive study of the resistivity of copper wires with lateral dimensions of 100 nm and smaller” *J. Appl. Phys.*, **97**, 023706 (2005)

[139] D. Gall, “The search for the most conductive metal for narrow interconnect lines” *J. Appl. Physic*, **127**, 050901 (2020)

[140] I. Petrov, P. B. Barna, L. Hultman, and J. E. Greene, “Microstructural evolution during film growth” *J. Vac. Sci. Technol. A Vacuum, Surfaces, Film.*, **21**, S117 (2003)

[141] M. Cattani and M. C. Salvadori, “Contribution of the morphological grain sizes to the electrical resistivity of platinum and gold thin films” *Surf. Rev. Lett.*, **11**, 463 (2004)

[142] G. P. Zhigal’skii and B. K. Jones, *The Physical Properties of Thin Metal Films*. Taylor &

Francis, 2003

[143] G. Abadias, L. Simonot, J. J. Colin, A. Michel, S. Camelio, and D. Babonneau, “Volmer-Weber growth stages of polycrystalline metal films probed by in situ and real-time optical diagnostics” *Appl. Phys. Lett.*, **107**, 183105 (2015)

[144] R. Messier, A. P. Giri, and R. A. Roy, “Revised structure zone model for thin film physical structure” *J. Vac. Sci. Technol. A*, **2**, 500 (1984)

[145] K. Sarakinos, “A review on morphological evolution of thin metal films on weakly-interacting substrates” *Thin Solid Films*, **688**, 137312 (2019)

[146] P. B. Barna and M. Adamik, “Fundamental structure forming phenomena of polycrystalline films and the structure zone models” *Thin Solid Films*, **317**, 27 (1998)

[147] K. L. Ekinci and J. M. Valles, “Formation of polycrystalline structure in metallic films in the early stages of zone I growth” *Acta Mater.*, **46**, 4549 (1998)

[148] J. M. Camacho and A. I. Oliva, “Surface and grain boundary contributions in the electrical resistivity of metallic nanofilms” *Thin Solid Films*, **515**, 1881 (2006)

[149] P. Jensen, “Growth of nanostructures by cluster deposition: Experiments and simple models” *Rev. Mod. Phys.*, **71**, 1695 (1999)

[150] J. E. Barborini *et al.*, “The influence of nanoscale morphology on the resistivity of cluster-assembled nanostructured metallic thin films” *New J. Phys.*, **12**, 073001 (2010)

[151] S. Yamamuro, K. Sumiyama, T. Hihara, and K. Suzuki, “Geometrical and electrical percolation in nanometre-sized Co-cluster assemblies” *J. Phys. Condens. Matter*, **11**, 3247 (1999)

[152] W. Bouwen *et al.*, “Characterization of granular Ag films grown by low-energy cluster beam deposition” *Thin Solid Films*, **354**, 87 (1999)

[153] L. Bardotti, B. Prével, P. Mélinon, A. Perez, Q. Hou, and M. Hou, “Deposition of clusters on Au(111) surfaces. II. Experimental results and comparison with simulations” *Phys. Rev. B - Condens. Matter Mater. Phys.*, **62**, 2835 (2000)

[154] B. Pauwels *et al.*, “Low-energy-deposited Au clusters investigated by high-resolution electron microscopy and molecular dynamics simulations” *Phys. Rev. B - Condens. Matter Mater. Phys.*, **62**, 10383 (2000)

[155] L. Bardotti, B. Prével, M. Treilleux, P. Mélinon, and A. Perez, “Deposition of preformed gold clusters on HOPG and gold substrates: Influence of the substrate on the thin film morphology” *Appl. Surf. Sci.*, **164**, 52 (2000)

[156] G. Fuchs *et al.*, “Low-energy Bi cluster beam deposition” *J. Phys. D. Appl. Phys.*, **26**, 1114 (1993)

[157] J. Schmelzer, S. A. Brown, A. Wurl, M. Hyslop, and R. J. Blaikie, “Finite-size effects in the conductivity of cluster assembled nanostructures” *Phys. Rev. Lett.*, **88**, 226802 (2002)

[158] A. D. F. Dunbar, J. G. Partridge, M. Schulze, and S. A. Brown, “Morphological differences between Bi, Ag and Sb nano-particles and how they affect the percolation of current through nano-particle networks” *Eur. Phys. J. D*, **39**, 415 (2006)

[159] A. Sattar, S. Fostner, and S. A. Brown, “Quantized Conductance and Switching in Percolating Nanoparticle Films” *Phys. Rev. Lett.*, **111**, 136808 (2013)

[160] P. Jensen *et al.*, “Direct observation of the infinite percolation cluster in thin films: Evidence for a double percolation porcess” *Phys. Rev. B*, **47**, 5008 (1993)

[161] B. Yoon *et al.*, “Morphology control of the supported islands grown from soft-landed clusters” *Surf. Sci.*, **443**, 76 (1999)

[162] F. Borghi *et al.*, “Cluster-assembled cubic zirconia films with tunable and stable nanoscale morphology against thermal annealing” *J. Appl. Phys.*, **120**, 055302 (2016)

[163] F. Bisio *et al.*, “Optical properties of cluster-assembled nanoporous gold films” *Phys. Rev. B - Condens. Matter Mater. Phys.*, **80**, 205428 (2009)

[164] D. Stauffer and A. Aharony, *Intorduction to percolation theory*. Taylor & Francis, 2003

[165] I. Balberg, “Tunnelling and percolation in lattices and the continuum” *J. Phys. D. Appl. Phys.*, **42**, 064003 (2009)

[166] A. I. Maaroof and B. L. Evans, “Onset of electrical conduction in Pt and Ni films” *J. Appl. Phys.*, **76**, 1047 (1994)

[167] H. Wei and H. Eilers, “From silver nanoparticles to thin films: Evolution of microstructure and electrical conduction on glass substrates” *J. Phys. Chem. Solids*, **70**, 459 (2009)

[168] G. Ambrosetti, C. Grimaldi, I. Balberg, T. Maeder, A. Danani, and P. Ryser, “Solution of the tunneling-percolation problem in the nanocomposite regime” *Phys. Rev. B - Condens. Matter*

Mater. Phys., **81**, 1 (2010)

[169] M. Sahimi, *Heterogeneous Materials I: Linear Transport and Optical Properties*. 2003

[170] F. A. Burgmann *et al.*, "Electrical conductivity as a measure of the continuity of titanium and vanadium thin films" *Thin Solid Films*, **474**, 341 (2005)

[171] G. Reiss, J. Vancea, and H. Hoffmann, "Grain-Boundary Resistance in polycrystalline Metals" *Phys. Rev. Lett.*, **56**, 2100 (1986)

[172] C. A. Neugebauer and M. B. Webb, "Electrical Conduction Mechanism in Ultrathin , Evaporated Metal Films" *J. Appl. Phys.*, **33**, 74 (1962)

[173] S. L. Johnson, A. Sundararajan, D. P. Hunley, and D. R. Strachan, "Memristive switching of single-component metallic nanowires" *Nanotechnology*, **21**, 125204 (2010)

[174] A. F. Mayadas, R. Feder, and R. Rosenberg, "Resistivity and Structure of Evaporated Aluminum Films" *J. Vac. Sci. Technol.*, **6**, 690 (1969)

[175] S. B. Soffer, "Statistical model for the size effect in electrical conduction" *J. Appl. Phys.*, **38**, 1710 (1967)

[176] Y. Namba, "Resistivity and Temperature Coefficient of Thin Metal Films with Rough Surface" *Jpn. J. Appl. Phys.*, **9**, 1326 (1970)

[177] R. C. Munoz and C. Arenas, "Size effects and charge transport in metals : Quantum theory of the resistivity of nanometric metallic structures arising from electron scattering by grain boundaries and by rough surfaces" *Appl. Phys. Rev.*, **4**, 011102 (2017)

[178] J. Vancea, G. Reiss, and H. Hoffmann, "Mean-free-path concept in polycrystalline metals" *Phys. Rev. B*, **35**, 6435 (1987)

[179] X. Y. Qin, W. Zhang, L. D. Zhang, and L. D. Jiang, "Low-temperature resistance and its temperature dependence in nanostructured silver" *Phys. Rev. B*, **56**, 596 (1997)

[180] B. Lutzer, O. Bethge, C. Zimmermann, J. Smoliner, and E. Bertagnolli, "*In situ* resistance measurements during physical vapor deposition of ultrathin metal films on Si(111) at room temperature" *J. Vac. Sci. Technol. B, Nanotechnol. Microelectron. Mater. Process. Meas. Phenom.*, **35**, 051802 (2017)

[181] S. Ciuchi, D. Di Sante, V. Dobrosavljević, and S. Fratini, "The origin of Mooij correlations in disordered metals" *npj Quantum Mater.*, **3**, 1 (2018)

[182] P. W. Anderson, E. Abrahams, and T. V. Ramakrishnan, “Possible explanation of nonlinear conductivity in thin-film metal wires” *Phys. Rev. Lett.*, **43**, 718 (1979)

[183] Y. Imry, “Possible role of incipient Anderson localization” *Phys. Rev. Lett.*, **44**, 469 (1980)

[184] B. J. Last and D. J. Thouless, “Percolation theory and electrical conductivity” *Phys. Rev. Lett.*, **27**, 1719 (1971)

[185] M. M. A. Yajadda, I. Levchenko, and K. Ostrikov, “Gold nanoresistors with near-constant resistivity in the cryogenic-to-room temperature range” *J. Appl. Phys.*, **110**, 023303 (2011)

[186] K. H. Muller and M. A. Yajadda, “Electron transport in discontinuous gold films and the effect of Coulomb blockade and percolation” *J. Appl. Phys.*, **111**, 123705 (2012)

[187] M. M. A. Yajadda, K. H. Müller, and K. Ostrikov, “Effect of Coulomb blockade, gold resistance, and thermal expansion on the electrical resistance of ultrathin gold films” *Phys. Rev. B*, **84**, 235431 (2011)

[188] I. S. Beloborodov, A. V. Lopatin, V. M. Vinokur, and K. B. Efetov, “Granular electronic systems” *Rev. Mod. Phys.*, **79**, 469 (2007)

[189] A. Zanardi *et al.*, “Miniaturized FISH for screening of onco-hematological malignancies” *Biotechniques*, **49**, 497 (2010)

[190] T. Santaniello and P. Milani, “Additive nano-manufacturing of 3D printed electronics using supersonic cluster beam deposition” , in *Cluster Beam Deposition of Functional Nanomaterials and Devices*, **15**, , Elsevier, 2020, 313

[191] E. Barborini, P. Piseri, and P. Milani, “Pulsed microplasma source of high intensity supersonic carbon cluster beams” *J. Phys. D. Appl. Phys.*, **32**, L105 (1999)

[192] P. Piseri, A. Podestà, E. Barborini, and P. Milani, “Production and characterization of highly intense and collimated cluster beams by inertial focusing in supersonic expansions” *Rev. Sci. Instrum.*, **72**, 2261 (2001)

[193] H. V. Tafreshi, P. Piseri, G. Benedek, and P. Milani, “The Role of Gas Dynamics in Operation Conditions of a Pulsed Microplasma Cluster Source for Nanostructured Thin Films Deposition” *J. Nanosci. Nanotechnol.*, **6**, 1140 (2006)

[194] H. V. Tafreshi, G. Benedek, P. Piseri, S. Vinati, E. Barborini, and P. Milani, “A simple nozzle configuration for the production of low divergence supersonic cluster beam by

aerodynamic focusing" *Aerosol Sci. Technol.*, **36**, 593 (2002)

[195] E. Barborini *et al.*, "Batch fabrication of metal oxide sensors on micro-hotplates" *J. Micromechanics Microengineering*, **18**, 055015 (2008)

[196] M. Marelli *et al.*, "Flexible and biocompatible microelectrode arrays fabricated by supersonic cluster beam deposition on SU-8" *J. Micromechanics Microengineering*, **21**, 045013 (2011)

[197] A. Z. Khosousi and A.-A. Dhirani, "Charge Transport in Nanoparticle Arrangements" *Chem. Rev.*, **108**, 4072 (2008)

[198] P. Eaton and P. West, *Atomic Force Microscopy*. Pxford University Press, 2010

[199] F. Borghi, A. Podestà, C. Piazzoni, and P. Milani, "Growth Mechanism of Cluster-Assembled Surfaces: From Submonolayer to Thin-Film Regime" *Phys. Rev. Appl.*, **9**, 044016 (2018)

[200] C. G. Granqvist and R. A. Buhrman, "Statistical model for coalescence of islands in discontinuous films" *Appl. Phys. Lett.*, **27**, 693 (1975)

[201] T. Andersson, "The electrical properties of ultrathin gold films during and after their growth on glass" *J. Phys. D. Appl. Phys.*, **9**, 973 (1976)

[202] R. F. Voss, R. B. Laibowitz, and E. I. Allessandrini, "Fractal (scaling) clusters in thin gold films near the percolation threshold" *Phys. Rev. Lett.*, **49**, 1441 (1982)

[203] F. Borghi, M. Mirigliano, P. Milani, and A. Podestà, "Quantitative Analysis of Gold Nano-aggregates by Combining Electron and Probe Microscopy Techniques" , in *Toward a Science Campus in Milan*, 2018, 67

[204] A.-L. Barabási and H. E. Stanley, *Fractal Concepts in Surface Growth*. CAMBRIDGE University Press, 1995

[205] D. I. Yakubovsky, A. V. Arsenin, Y. V. Stebunov, D. Y. Fedyanin, and V. S. Volkov, "Optical constants and structural properties of thin gold films" *Opt. Express*, **25**, 25574 (2017)

[206] G. B. Smith, A. I. Maaroof, and M. B. Cortie, "Percolation in nanoporous gold and the principle of universality for two-dimensional to hyperdimensional networks" *Phys. Rev. B - Condens. Matter Mater. Phys.*, **78**, 165418 (2008)

[207] C. Durkan and M. E. Welland, "Analysis of failure mechanisms in electrically stressed gold

nanowires" *J. Appl. Physic*, **86**, 1280 (1999)

[208] S. B. Arnason, S. P. Herschfield, and A. F. Hebard, "Bad metals made with good-metal components" *Phys. Rev. Lett.*, **81**, 3936 (1998)

[209] A. F. Hebard and S. B. Arnason, "Bad-Metal Behavior : Exotic Physics or a Consequence of Microstructure ?" *J. Supercond.*, **12**, 159 (1999)

[210] J. C. Blair, C. R. Fuller, P. B. Ghate, and C. T. Haywood, "Electromigration-induced failures in, and microstructure and resistivity of, sputtered gold films" *J. Appl. Phys.*, **43**, 307 (1972)

[211] C. Durkan and M. Welland, "Size effects in the electrical resistivity of polycrystalline nanowires" *Phys. Rev. B - Condens. Matter Mater. Phys.*, **61**, 14215 (2000)

[212] M. Aguilar, A. I. Oliva, and P. Quintana, "The effect of electrical current (DC) on gold thin films" *Surf. Sci.*, **409**, 501 (1998)

[213] A. Mehonic and A. J. Kenyon, "Emulating the electrical activity of the neuron using a silicon oxide RRAM cell" *Front. Neurosci.*, **10**, 1 (2016)

[214] A. Clauset, C. R. Shalizi, and M. E. J. Newman, "Power-law distributions in empirical data" *SIAM Rev.*, **51**, 661 (2009)

[215] P. Bak, C. Tang, and K. Wiesenfeld, "Self-organized criticality: an explanation of 1/f noise" *Phys. Rev. Lett.*, **59**, 381 (1987)

[216] J. P. Sethna, K. A. Dahmen, and C. R. Myers, "Crackling noise" *Nature*, **410**, 242 (2001)

[217] G. E. P. Box, G. M. Jenkins, G. C. Reinsel, and G. M. Ljung, *Time Series Analysis Forecasting and Control*, **53**, . Wiley, 2016

[218] G. Tononi, O. Sporns, and G. M. Edelman, "A measure for brain complexity: Relating functional segregation and integration in the nervous system" *Proc. Natl. Acad. Sci. U. S. A.*, **91**, 5033 (1994)

[219] J. P. Crutchfield and K. Young, "Inferring statistical complexity" *Phys. Rev. Lett.*, **63**, 105 (1989)

[220] M. Gell-Mann and S. Lloyd, "Information measures, effective complexity, and total information" *Complexity*, **2**, 44 (1996)

[221] A. Papoulis, *Probability, Random Variables and Stochastic Processes*. New York: McGraw-Hill, 1991

[222] G. Tononi, M. Boly, M. Massimini, and C. Koch, “Integrated information theory: From consciousness to its physical substrate” *Nat. Rev. Neurosci.*, **17**, 450 (2016)

[223] I. Boybat *et al.*, “Neuromorphic computing with multi-memristive synapses” *Nat. Commun.*, **9**, 1 (2018)

[224] A. Serb, A. Khiat, and T. Prodromakis, “Seamlessly fused digital-analogue reconfigurable computing using memristors” *Nat. Commun.*, **9**, 2170 (2018)

[225] M. V Nair, L. K. Muller, and G. Indiveri, “A differential memristive synapse circuit for on-line learning in neuromorphic computing systems” *Nano Futur.*, **1**, 035003 (2017)

[226] P. S. Zarrin, F. Zahari, M. K. Mahadevaiah, E. Perez, H. Kohlstedt, and C. Wenger, “Neuromorphic on-chip recognition of saliva samples of COPD and healthy controls using memristive devices” *Sci. Rep.*, **10**, 1 (2020)

[227] P. Sheng and B. Abeles, “Voltage-induced tunneling conduction in granular metals at low temperatures” *Phys. Rev. Lett.*, **28**, 34 (1972)

[228] L. L. Kazmerski, D. M. Racine, and M. S. Ayyagari, “Temperature coefficient of resistance in ultrathin metal films” *J. Appl. Phys.*, **46**, 2658 (1975)

[229] I. S. Beloborodov, K. B. Efetov, A. V. Lopatin, and V. M. Vinokur, “Transport properties of granular metals at low temperatures” *Phys. Rev. Lett.*, **91**, 246801 (2003)

[230] A. Zabet-khosousi, P. Trudeau, Y. Suganuma, A. Dhirani, and B. Statt, “Metal to Insulator Transition in Films of Molecularly Linked Gold Nanoparticles” *Phys. Rev. Lett.*, **96**, 156403 (2006)

[231] P. N. Nirmalraj *et al.*, “Manipulating connectivity and electrical conductivity in metallic nanowire networks” *Nano Lett.*, **12**, 5966 (2012)

[232] C. Ghisleri *et al.*, “Patterning of gold-polydimethylsiloxane (Au-PDMS) nanocomposites by supersonic cluster beam implantation” *J. Phys. D. Appl. Phys.*, **47**, 015301 (2014)

[233] R. Erni, *Aberration-corrected imaging in transmission electron microscopy*, 2nd ed. London: Imperial College Press, 2015

[234] M. Hövel, B. Gompf, and M. Dressel, “Dielectric properties of ultrathin metal films around the percolation threshold” *Phys. Rev. B - Condens. Matter Mater. Phys.*, **81**, 035402 (2010)

[235] C. Acha, “Graphical analysis of current-voltage characteristics in memristive interfaces” *J.*

Appl. Phys., **121**, 134502 (2017)

[236] C. Acha, A. Schulman, M. Boudard, K. Daoudi, and T. Tsuchiya, "Transport mechanism through metal-cobaltite interfaces" *Appl. Phys. Lett.*, **109**, 011603 (2016)

[237] Y. Xia, W. He, L. Chen, X. Meng, and Z. Liu, "Field-induced resistive switching based on space-charge-limited current" *Appl. Phys. Lett.*, **90**, 022907 (2007)

[238] T. Burr, A. Seraphin, E. Werwa, and K. Kolenbrander, "Carrier transport in thin films of silicon nanoparticles" *Phys. Rev. B - Condens. Matter Mater. Phys.*, **56**, 4818 (1997)

[239] T. Tmai and K. Tsuchiya, "Contact Resistance Characteristics at Low Temperature" *IEEE Trans. COMPONENTS, HYBRIDS, Manuf. Technol.*, **CHMT-1**, 54 (1978)

[240] W. Chen, H. Ahmed, and K. Nakazoto, "Coulomb blockade at 77 K in nanoscale metallic islands in a lateral nanostructure" *Appl. Phys. Lett.*, **66**, 3383 (1995)

[241] C.-W. Jiang, I.-C. Ni, S.-D. Tzeng, and W. Kuo, "Anderson localization in strongly coupled gold-nanoparticle assemblies near the metal – insulator transition" *Appl. Phys. Lett.*, **101**, 083105 (2012)

[242] N. W. Ashcroft and D. N. Mermin, *Solid State Physics*. Cengage Learning, Inc, 1976

[243] M. Kaveh and N. Wiser, "Deviations from Matthiessen's Rule ofr the elctrical resitivity of dislocations" *J. Phys. F Met. Phys.*, **16**, 795 (1986)

[244] P. A. Lee and T. V. Ramakrishnan, "Disordered electronic systems" *Rev. Mod. Phys.*, **57**, 287 (1985)

[245] M. Bowman, A. Anaya, A. L. Korotkov, and D. Davidović, "Localization and capacitance fluctuations in disordered Au nanojunctions" *Phys. Rev. B*, **69**, 205405 (2004)

[246] A. L. Efros and B. I. Shklovskii, "Critical Behaviour of Conductivity and Dielectric Constant near the Metal-Non-Metal Transition Threshold" *Phys. Status Solidi*, **76**, 475 (1976)

[247] D. Valencia *et al.*, "Grain-Boundary Resistance in Copper Interconnects: From an Atomistic Model to a Neural Network" *Phys. Rev. Appl.*, **9**, 044005 (2018)

[248] T. Kim *et al.*, "Large Discrete Resistance Jump at Grain Boundary in Copper Nanowire" *Nano Lett.*, **10**, 3096 (2010)

[249] A. Anaya, A. L. Korotkov, M. Bowman, J. Waddell, and D. Davidovic, "Nanometer-scale metallic grains connected with atomic-scale conductors" *J. Appl. Phys.*, **93**, 3501 (2003)

[250] A. Vahl *et al.*, “Concept and modelling of memsensors as two terminal devices with enhanced capabilities in neuromorphic engineering” *Sci. Rep.*, **9**, 1 (2019)

[251] Y. Zhou and S. Ramanathan, “Mott Memory and Neuromorphic Devices” *Proc. IEEE,* **103**, 1289 (2015)

Acknowledgments

Since this research is the result of many human and professional interactions, I sincerely want to thank the amazing people that I had the opportunity to meet during the last three years because they all taught me a lot.

Firstly, I thank my tutor, Prof. Paolo Milani, for having believed in me and having shared the maximum of the enthusiasm, working hard to help solving the problems encountered along the way, keeping morale high.

Secondly, my thanks go to Prof. Cristina Lenardi for the patience to tutor me at the beginning of my PhD.

I also have to thank all the people who both helped me and contributed to the work shown in the thesis: Prof. Marco Potenza and Bruno Paroli as they made a fundamental contribution to the research shown in Chapter 6 and improved both the value of the work and my personal background as the discussions had with Bruno taught me a lot; Prof. Andrea Falqui and Alberto Casu for the availability to discussions, for me of great importance, and for the professionalism had during our collaboration; Prof. Davide Galli and Francesco Mambretti, who shared the maximum effort in the theoretical understanding of my experimental work, giving rise to interesting and fundamental discussions; Prof. Alberto Pullia, who gave me the possibility to use the facilities in the electronic laboratory; Prof. Luciano Colombo and his group that started the simulation work during my first PhD year; a special thanks to Francesco Cavaliere and to the colleagues of the mechanical Workshop (Daniele, Federico and William) at the Physics Department, for both the willingness to satisfy requests and the precision shown in the commissioned works; Prof. Petra Rudholf and her group at the University of Groening, in particular C. Sibanda, that started a collaboration to study optical and electronic properties of cluster-assembled films.

I cannot forget the CIMaINa staff. My warm thanks go to prof. Paolo Piseri, my work would not be the same without the precious discussions with him. Thanks to prof Alessandro Podestà for his advices that improved my background. I met them when I was a master's student, and they continue to teach me a lot. Thanks to Claudio Piazzoni for having helped me in dealing with the difficult life of an experimental laboratory (I stressed him lot for every technical problem). Thanks to all my colleagues, old and new, that shared the laboratory facilities with me during the last three years: they improved my work through their spontaneous discussions and their abilities in building a strong team. A special thanks to Matteo and Sara, that I met when I was student and we met again as PhD colleagues; thanks to Francesca B., the first person who collaborated with me at the beginning of the PhD, Lorenzo (to him the burden of managing the team building), Tommy, Charsten, Marcel, Marco

(our motto was and will be ‘flectar ne frangar’), Matteo G., Ewelina, Hatice (who reminded me of the importance of having lunch), Riccardo, Lorenzo G., Francesca O. and above all Anita, that helped me in the most important moment the work: the thesis submission. Thanks to Mrs. Tiziana, for the company early in the morning as soon as I get to work.

A sincere thanks to all the student that I met during my PhD work; in particular, thanks to Marta, Matteo, Davide, Stefano, Marco, Gianluca, Silvia, Federica and Francesco: through their sincere questions and their dedication to work taught me a lot and improved my work. Thanks also to Matteo Tiberi that worked with us and gave a great contribution in building the team.

Last but not least, I thank my parents that have helped me since the beginning of my studies and all the people in my family that gave me a lot of useful advices during these years. Obviously, thanks to my friends, old and new, near and far, you are so many that I cannot list you all. A special thanks to the people that spent a lot of time with me during the last years in Milano, that, following the recent provisions of our governments, I can formally define ‘congiunti’: Vincenzo, Chiara, Ilario, Martina, Giulia, Ale, Roberta, Sofia and Andrea, old friend that I met again at the PhD schools of the University of Milano.

Finally, I want to highlight that, despite the several contributions received to my work, all the errors found in the thesis must be attributed only to me.